ABSTRACT

The era of gravitational wave astronomy was ushered in by the LIGO (Laser Interferometer Gravitational-Wave Observatory) collaboration with the detection of a binary black hole collision [2]. The event that shook the foundation of space-time allowed mankind to view the cosmos in a way that had never been done previously. Since then, another remarkable event was found by the LIGO and Virgo detectors where two neutron stars collided, sending both gravitational and electromagnetic waves to earth [3]. LIGO was built with the purpose of detecting the ripples in space-time caused by astrophysical events with the hopes of understanding the complexities hidden within the cosmos. In 2011, the primary stages of Advanced LIGO were installed and commissioned to start the first observing run (O1). During the writing of this thesis, the detectors had hardware replaced in order to mitigate noise from scattered light and new optics which reduced the losses from absorption. The upgrades were in preparation for the third observing run (O3) and the work presented here is primarily focused on experimental techniques for operating at higher power and mode matching Gaussian beams in the dual-recycled Michelson interferometer for the Advanced LIGO era and beyond. The first two chapters discuss the fundamentals of gravitational waves and the LIGO detector configurations. The third chapter introduces the reader to fundamentals in mode matching Gaussian laser beams. The fourth and fifth chapter summarizes the author's work at Syracuse University. The sixth chapter deals with work at the LIGO Hanford observatory with an emphasis on mode sensing and high-power operation.

ADAPTIVE MODE MATCHING IN ADVANCED LIGO AND BEYOND

By

Thomas V. Vo

B.S. University of Washington, Seattle, WA, 2010
M.S. Syracuse University, Syracuse, NY, 2016

Dissertation
Submitted in Partial Fulfillment of the Requirements
for the degree of
Doctor of Philosophy in Physics

Syracuse University
May 2019

ACKNOWLEDGEMENTS

I would like to thank my thesis advisor Stefan Ballmer for trusting in me as a scientist, always providing indispensable advice, and allowing me to follow my interests.

To Peter Saulson: Your love of science truly inspires me to be a better scientist and teacher.

To Duncan Brown: Tough questions force us to grow and your group meetings provided a growth spurt.

To Sheila Dwyer, Jenne Driggers, and Georgia Mansell: Thank you for your patience in teaching me the gritty details about the Hanford interferometer, I will never forget the in-chamber work at HAM6 and the long commissioning hours in the control room.

To Daniel Sigg: Your dinners are the perfect fugue of flavors, conversations and friends. Thank you for letting me participate in some of the crucial interferometer commissioning tasks.

To Keita Kawabe: Thank you for the tough questions but also the encouragement to do the best science.

To Mike Landry: From operator to graduate student, thank you for your help, support and guidance.

To Rick Savage: I was honored to be a Fellow for so long, thank you for the advice about all aspects of life and the fishing trips when I needed it most.

To Aidan Brooks: Thank you for letting me work on/use TCS at Hanford, your guidance and experience is invaluable in times of confusion.

To Daniel Vander-Hyde: Thank you for being patient with me when things weren't going well but also celebrating with me when things were!

To Dan Brown: Cheers for coming across the pond to help when we needed it most and the Inbetweeners jokes on wings night.

To Corey Gray, Gunner and Gomez: The hikes brought peace to my troubled mind and patience to my restless soul.

To TJ Shaffer: Thank you for helping with steady hands or Guardian skills.

To all the operators and staff at Hanford: Jeff, Betsy, Chandra, TJ, Jim, Cheryl, Nico, Patrick, Ed, Gerardo, Evan.

To Hang Yu: Thank you for helping me understand the inner workings of the interferometer with only a few lines of math and a drawing.

To my forever teachers Melissa Brainerd, Paul Didier, Chrissy Dahms, Carolyn West, and Dan Dorsey: My work is a direct ripple from your teachings and you inspire kids like me from White Center to chase our dreams.

To my childhood friends Quang, Leah, Thang, Sienna, Khanh, Truc, Kay, Tuan, Wanda, James, Matt and Trung: You knew me when I was just dreaming of being a scientist, now we're here.

To the Bloomingdale family: Thank you for making me feel at home even in the frigid Syracuse winters.

To Jaysin Lord, Laura Nuttall, and Mat Hutchings: Thank you for the laughs and Thursday wings.

To my family Cuong, Nhi, Tony, Theresa, Brittny, Kayla, Chloe: Your support and encouragement mean everything to me.

To my parents: The difficulties of science are modest in comparison to your journey from Vietnam, this work is dedicated to you.

To my darling Tiffany: Your support provides nourishment for my soul and your love gives a guiding light through the darkest of nights.

Contents

List of Tables

List of Figures

Preface

The work presented in this thesis stems from my participation in the LIGO Scientific Collaboration (LSC).

LIGO DCC Number: P1900086

Chapter 1

Introduction

This chapter will focus primarily on the theoretical constructs of gravitational waves and underlying principles of using a Michelson interferometer to detect them. The derivations draw heavily on the work of Schutz [80] and Saulson [77].

1.1 Gravitational Waves

In 1915, Albert Einstein published his theory of general relativity [38], which contains the most complete description of gravity to date. This theory has stood the test of time and scrutiny by correctly predicting the perihelion of mercury [36], the bending of light from massive objects [35], the gravitational redshift effect [86], and the loss of energy from gravitational radiation [90]. The seminal equation in this theory, called the Einstein Field Equation is

$$G_{\mu\nu} = 8\pi T_{\mu\nu} \tag{1.1}$$

which is a set of 10 coupled second-order differential equations that are nonlinear and fully describes the interaction between space-time and mass-energy. Equation 1.1 is difficult to solve analytically except in situations where specific approximations allow a user to find exact solutions, such as spherical symmetry [21] [81]. In areas where the curvature is close to flat, the weak field approximation can be applied and the metric is described as

$$g_{\mu\nu} \cong \eta_{\mu\nu} + h_{\mu\nu} \tag{1.2}$$

where $\eta_{\mu\nu}$ is the metric of flat spacetime and $|h_{\mu\nu}| \ll 1$ is the perturbation due to a gravitational field. Considering only the vacuum solution ($T_{\mu\nu} = 0$), we obtain the wave equation from [80],

$$\Big(\nabla^2 - \frac{1}{c^2}\frac{\partial^2}{\partial t^2}\Big)\overline{h}_{\mu\nu} = 0 \tag{1.3}$$

where $\overline{h}_{\mu\nu} = h_{\mu\nu} - \frac{1}{2}\eta_{\mu\nu}h^{\alpha}_{\alpha}$ and only in the transverse-traceless gauge [80] will $\overline{h}_{\mu\nu} = h_{\mu\nu}$. For the remainder of the text, $h_{\mu\nu}$ will be referred to as the gravitational wave (GW). One could ask if a GW passes by a pair of particles initially separated by length L, what would be the change in distance between the two points? In [80], the length change δl, was shown to be

$$\delta l = \int g_{\mu\nu}dx^{\mu}dx^{\nu} = \int_0^L g_{xx}dx \approx |g_{xx}(x=0)|^{1/2} \approx [1 + \frac{1}{2}h_{xx}(x=0)]L \tag{1.4}$$

which is proportional to the gravitational wave and the initial separation between the particles. This means a detector that is large will have a better chance to measure the perturbation, which was an important point that drove the design of the Laser Interferometer Gravitational-Wave Observatory.

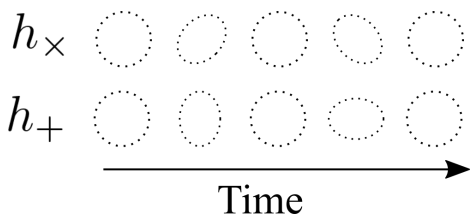

Figure 1 : **A ring of free floating particles being stretched and squeezed by a passing gravitational wave.** In this picture, the wave is traveling in the transverse direction to the rings (in/out of the page) and the two pictures represent the plus and cross polarizations.

1.2 Measuring Gravitational Waves with Light

During the Chapel Hill Conference in 1957 [8], which included some of the great minds of the era such as Wheeler, Dicke, and Feynman, the experimental search for gravitational waves began to take hold. One interesting thought experiment that was proposed by Pirani [25][74] where he considered a bead sliding on a string with friction as a gravitational wave passes. As the bead slides back and forth due to the wave described by equation 1.4, there will be some heat dissipated which means the gravitational wave must carry some energy and hence, be a physical effect. The earliest attempts at detecting gravitational waves were done by Joseph Weber [89] using large aluminum bars and piezoelectric transducers to extract the energy from gravitational waves at the resonant frequencies. However, these bars are limited by thermal noise and could only detect GWs in very narrow frequency bands.

With the development of lasers in the 1960s, which created coherent and spatially confined light that could propagate long distances, another prospect for measuring gravitational waves using interferometry was thoroughly considered by Weiss et al. [39]. As light travels in space, it picks up an important quantity called *phase* as a function of distance. Interferometers are transducers that measure small displacements by using a laser beam that is split by a partially transmitting mirror, which allows 50% of the light to get reflected and 50% to be transmitted. Each of the beams travel down the arms and reflect off of mirrors and return to the beamsplitter. Upon reaching the optic, the two beams recombine and by the principle of superposition the electromagnetic waves will add linearly at the output port (or antisymmetric port), Figure 2. The laser beams will gather phase as they propagate down each individual arm, and when recombining, the intensity of the light will be proportional to the phase differences between each beam. This will correspond to a differential length that is described by

$$l_{-} = l_x - l_y \tag{1.5}$$

As shown in equation 1.4, the effect of gravitational waves on the proper length between two free falling objects is proportional to the initial separation. It can be shown that interferometry is an ideal technique to sense signals from a gravitational wave and one can explicitly derive the detector's response to a GW from an astrophysical object.

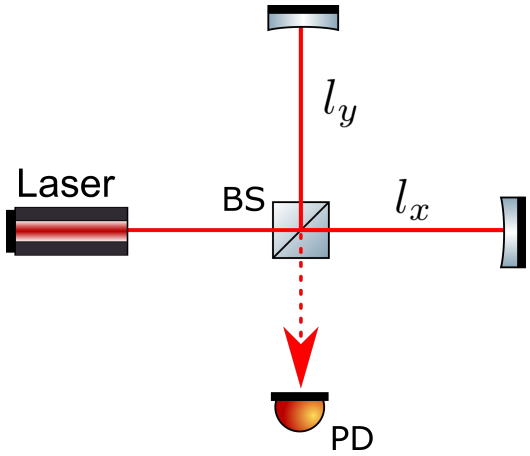

Figure 2 : **A Michelson Interferometer.** A laser is split between with a partially transmitting optic called a beamsplitter (BS), then propagate down each arm to reflect off mirrors, sometimes called test masses (TM). The beams return to the beamsplitter and recombine, photodetectors are placed at the antisymmetric port (AS).

If the gravitational wave radiation is propagating towards the interferometer from directly above, the GW is strictly a function of time and the polarization aligns with the interferometer. So, the null geodesic equation (i.e. the path of a photon) in the interferometer frame becomes [77]

$$ds^2 = -dt^2 + [1 + h(t)]dx^2 + [1 - h(t)]dy^2 + dz^2 = 0 \tag{1.6}$$

where $h(t)$ is the GW amplitude. Now, if the photon is traveling along the x-arm, this means that $dy^2 = dz^2 = 0$ and the metric equation transforms to

$$\frac{dt}{dx} = \sqrt{1 + h(t)} \approx 1 + \frac{1}{2}h(t) \tag{1.7}$$

The amount of time required for the photon to reach the x-end mirror (starting at $t = 0$) is equal to

$$t_1 = \int_0^{l_x/c} [1 + \frac{1}{2}h(t)]\mathrm{d}t \tag{1.8}$$

where l_x is the total length of the x-arm and $h(t)$ is the GW amplitude as a function of propagation distance. Upon returning to the beamsplitter, the photon's total time

of flight for the x and y arms are, respectively,

$$t_2 = 2\frac{l_x}{c} + \frac{1}{2}\int_0^{l_x/c}\Big[h(t) + h(t + l_x/c)\Big]\mathrm{d}x \tag{1.9}$$

$$t_2' = 2\frac{l_y}{c} - \frac{1}{2}\int_0^{l_y/c}\Big[h(t) + h(t + l_y/c)\Big]\mathrm{d}y \tag{1.10}$$

If the gravitational wave period is much longer than the time of flight, then $h(t)$ does not change significantly during the measurement, which means $h(t) \approx h(t + l_x/c) \approx$ *constant* (similarly for the y-direction). By subtracting the flight times of the photons for each arm and setting $l = l_x = l_y$, the difference is proportional to the gravitational wave perturbation multiplied by the sum of arm lengths,

$$\Delta t = t_2 - t_2' = \frac{2l}{c}h \tag{1.11}$$

By recasting the expression for time of flight in terms of the phase picked up laser light as it travels through space, the differential phase shift is [77]

$$\Delta\Phi = \Phi(t_2) - \Phi(t_2') = \frac{4\pi}{\lambda}\,h\,l \tag{1.12}$$

The equation above only works for gravitational wave signals that are varying slowly with respect to the round trip light propagation time and it assumes that the path length can be arbitrarily long. Both points are not strictly true [77] but we can alleviate these discrepancies by considering a gravitational wave signal of the form $h(t) = h_0\, e^{i2\pi f_{GW} t}$ and repeating the calculation between equations 1.8 and 1.12:

$$\Delta\Phi(t) = h(t)\ \tau_{RT}\ \frac{2\pi c}{\lambda}\ \mathrm{sinc}(f_{GW}\tau_{RT})e^{i\pi f_{GW}\tau_{RT}} \tag{1.13}$$

where $\tau_{RT} = 2l/c$. The response for a detector has null points from the sinc function that is dependent on the gravitational wave frequency and the round trip time constant. Figure 3 compares the response of an interferometer with 4 km arms versus 100 km and there is larger low frequency response for the longer detector but has large dips when approaching the kilohertz regime where solar mass compact binaries tend to merge. This means that the instrument is not as useful for detecting known astrophysical events [42] when the length reaches close to 100 km, however, it is very

expensive and difficult to make a terrestrial detector of this size. On the other hand, space-based detectors such as the LISA project will have to account for this effect.

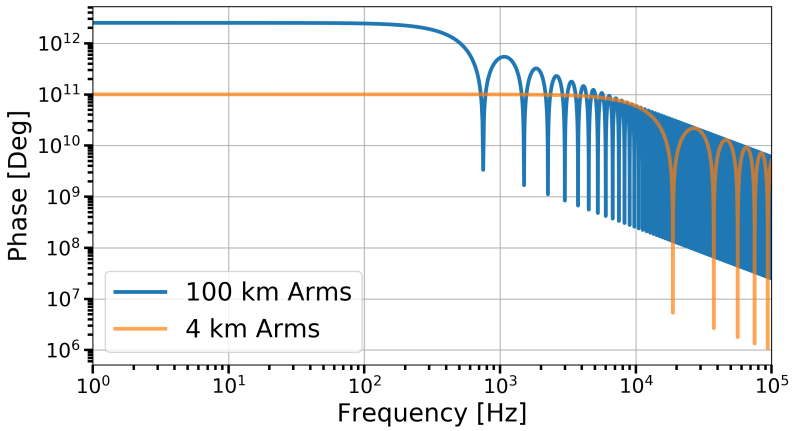

Figure 3 : **The phase response of an interferometer to a gravitational wave.** The horizontal axis is in GW frequency and the vertical axis is the accumulated phase shift.

1.3 Detection of Gravitational Waves

The purpose of LIGO is to observe gravitational waves emanating from astrophysical objects [39], so it is natural to wonder how well a single detector can probe the universe. The inspiral horizon distance is how far a single detector can detect a binary system comprised of two equal mass compact objects optimally oriented in the sky relative to the detector. Using the convention from [1], the optimal signal-to-noise ratio (SNR) can be expressed as

$$\rho = \sqrt{4 \int_{f_\mathrm{l}}^{f_\mathrm{h}} \frac{\tilde{h}(f)\tilde{h}^*(f)}{S_n(f)}} \tag{1.14}$$

where $S_n(f)$ is the one-sided average power spectral density of the detector noise and $\tilde{h}(f)$ is the Fourier transform of the detectors' response to a gravitational-wave signal. The lower limit frequency, f_l is determined by the increased detector noise at lower frequencies. For Advanced LIGO, this is typically 20 Hz. The high frequency limit, f_h, will be determined by the innermost stable circular orbit [42]. For an binary system where each object has a mass equal to $1.4\mathrm{M}_\odot$, the upper frequency cutoff is 1570 Hz.

Consider two dense objects which are approximated by point sources with equal masses (m_1 and m_2) spiraling around each other. If the binary is optimally oriented and located in the sky relative to the detector then the signal which appears at the interferometer can be described by [43]

$$\tilde{h}(f) = \frac{1}{d_H}\left(\frac{5\pi}{24c^3}\right)^{1/2}(G\mathcal{M})^{5/6}(\pi f)^{-7/6}e^{i\Psi(f;M)} \tag{1.15}$$

where

$$\mathcal{M} = \frac{(m_1 m_2)^{3/5}}{(m_1+m_2)^{1/5}} \tag{1.16a}$$

By convention, $\mathcal{M}$ is called the chirp mass, d_H is the horizon distance, and $\Psi(f;M)$ is a real function of frequency that is parameterized by the total mass. By setting the signal to noise ratio in equation 1.14 to $\rho = 8$ and using equation 1.15, the horizon distance is

$$d_H = \frac{1}{8}\left(\frac{5\pi}{24c^3}\right)^{1/2}(G\mathcal{M})^{5/6}(\pi)^{-7/6}\sqrt{4\int_{f_\mathrm{l}}^{f_\mathrm{h}}\frac{f^{-7/3}}{S_n(f)}} \tag{1.17}$$

To go from the horizon distance which is the furthest an interferometer can sense an optimally placed binary neutron star to the quantity commonly referred to as *sensemon range*, d_h is divided by a factor of 2.26 to account for averaging over all sky locations and binary orientations [43]. In the control rooms at the LIGO detectors, the sensemon range is one figure of merit for the interferometer performance.

Chapter 2

The LIGO Instrument

When gravitational waves were first detected, the first question on everybody's mind was: **"Is it real?"**.

Soon after, the question was **"How do we get more?"**.

The previous chapter dealt with gravitational waves and briefly touched on how a laser interferometer is particularly well-suited for detecting them. In its simplest form, the LIGO instrument is an incredibly large Michelson interferometer. However, to make a practical gravitational-wave observatory, the complexity had to be extended far beyond what Michelson and Morley used. The next sections will explore the various instrument configurations that improve LIGO's sensitivity and a few fundamental noise sources.

2.1 Interferometer Configurations

2.1.1 Simple Michelson

As shown in Figure 2, modern interferometers use a laser which is incident on a partially-reflecting and partially-transmitting beamsplitter that sends half of the laser light down each arm. The individual beams gather phase as they propagate down the arms and then reflect off of two end mirrors and eventually recombine at the same beamsplitter. Whether the light constructively or destructively interferes will depend on their relative accumulated phase from propagating down each arm. A photodetector is placed at the output and measures the total power which converts the total amount of light into an electronic signal. In Section 1.2, it was shown that the

differential time of flight between photons traveling down the individual arms carry gravitational wave information. The difference in flight times, Δt, can be converted into how much phase, $\Delta\phi$, is accumulated by the photons as they propagate through space.

But the question remains, how does an interferometer explicitly measure $\Delta\phi$? If the input electric field of the interferometer is E_0, the beamsplitter will transmit $iE_0/\sqrt{2}$ down the x-arm and reflect $E_0/\sqrt{2}$ towards the y-arm. By setting the beamsplitter to be the origin, the two plane waves traveling down their respective arms will have gathered a phase ϕ_i, where the individual arms are denoted by the subscripts. Then, upon reflecting off the end mirrors and returning to the beamsplitter the resultant fields are transmitted to the antisymmetric port. Each of the electric fields from the arms can be described by these equations

$$\begin{aligned} E_x &= \frac{iE_0}{2} e^{2i\phi_x} \\ E_y &= \frac{iE_0}{2} e^{2i\phi_y} \end{aligned} \tag{2.18}$$

Since the electromagnetic waves are linear, the resultant sum of waves at the antisymmetric port will be $E_{out} = E_x + E_y$. The photodiode at the output, or antisymmetric (AS), port detects the integrated power which is related to the total electric field by

$$\begin{aligned} P_{AS} &= \int_{\text{Area}} I \, \mathrm{d}A \\ &= \int_{\text{Area}} |E_x + E_y|^2 \, \mathrm{d}A \\ &= P_{in} \, \cos^2(\Delta\phi) \end{aligned} \tag{2.19}$$

where $\Delta\phi = \phi_x - \phi_y = k_x l_x - k_y l_y$ and $P_{in} = \int_{\text{Area}} |E_0|^2 \mathrm{d}A$ is the input power. By using equation 1.12 and the common (or average) arm length $l_+ = \frac{l_x + l_y}{2}$, the power due to a differential phase shift is

$$P_{AS}|_{\text{Bright}} \approx P_{in} \, (1 - 2\Delta\phi) = P_{in} \, (1 - 2k l_+ h_+) \tag{2.20}$$

There is a large DC term that is dependent on the input power and generally, it is very difficult to measure small changes in a large signal. This is configuration can be

referred to as being on a bright fringe. So the next obvious method is to shift the arm lengths such that the output port is operating on a dark fringe, normally this is called a null-point operation. However, there are difficulties associated with this method as well. Consider shifting the phase of equation 2.19 by $\pi/2$, which would result in

$$P_{AS}|_{\text{Dark}} = P_{in}\,\sin^2(\Delta\phi) \approx P_{in}\,(kl_+h_+)^2 \tag{2.21}$$

This results in a second-order dependence on a gravitational-wave signal that is already approximated to be very small. So a good solution to the issue of how to *read out* a gravitational wave signal can be remedied using radio frequency (RF) detection methods. By changing the interferometer input from a single laser to adding an electro-optical modulator (EOM) that sinusoidally modulates the laser frequency and expanding to first order using the Bessel functions,

$$\begin{aligned} E_{in} &= E_0 e^{i(wt+\beta\cos(\Omega t))} \\ &\approx E_0 e^{iwt}[J_0(\beta) + J_1(\beta)e^{i\Omega t} + J_1(\beta)e^{-i\Omega t}] \\ &= E_{C,in} + E_{SB+,in} + E_{SB-,in} \end{aligned} \tag{2.22}$$

where Ω and β are the modulation frequency and depths, respectively. The first term is commonly called the carrier field whereas the second and third terms are referred to as the (upper or lower) sidebands. Because there are multiple electric fields, it is useful to define an optical transfer function which maps the interferometer's input fields to its output,

$$E_{out} = E_C + E_{SB+} + E_{SB-} = \begin{pmatrix} t_C \\ t_{SB+} \\ t_{SB-} \end{pmatrix} \begin{pmatrix} E_{C,in} & E_{SB+,in} & E_{SB-,in} \end{pmatrix} \tag{2.23}$$

The carrier transfer function, t_C has already been calculated by equations 2.19 - 2.21 and the sideband transfer functions are not much different.

$$t_{SB\pm} = r_{x,\pm}e^{i\phi_{\pm,x}} - r_{y,\pm}e^{i\phi_{\pm,y}} \tag{2.24}$$

where $\phi_{\pm,i} = (k \pm k_\Omega)\,\ell_i = (\frac{w+\Omega}{c})\ell_i$. In the current example, the sidebands and carrier fields reflect off the mirrors identically, however, this will not be true in general when

dealing with resonators that are highly frequency dependent. Plugging equation 2.24 into 2.23, the output electric field becomes

$$E_{out} = ie^{iwt}[J_0(\beta)k\ell_+h_+ \ + \ J_1(\beta)\sin(k\Delta\ell + k_\Omega\Delta\ell)(e^{i\Omega t} + e^{-i\Omega t})] \tag{2.25}$$

where $\Delta\ell = \frac{l_x - l_y}{2}$ is the average differential arm length. The frequency offset of the sidebands allow them to accumulate phase differently than the carrier field. Thus, by choosing a static offset between the arm lengths such that the carrier signal is on a dark fringe, $k\Delta\ell = \pi/2$, but the sideband are slightly off the null point (Figure [4]) and leak into the anti-symmetric port. This technique is colloquially known as the *Schnupp Asymmetry* and the electric field reduces to

$$E_{out} = ie^{iwt}[J_0(\beta)k\ell_+h_+ \ + \ J_1(\beta)\sin(k_\Omega\Delta\ell)(e^{i\Omega t} + e^{-i\Omega t})] \tag{2.26}$$

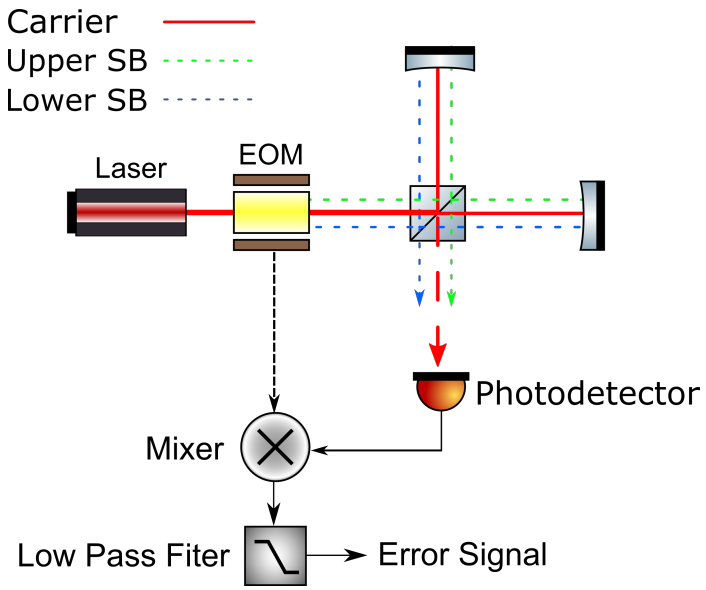

Figure 4 : **A heterodyne detection scheme for interferometers.** The laser enters an electro-optical modulator which creates three fields described by equation 2.22 and read out by a photodetector. The error signal at the output is then filtered and described by equation 2.29.

The intensity, which is equal to the electric field squared can be described by

$$\begin{aligned} I = |E_{out}|^2 =& |E_C|^2 + |E_{SB+}|^2 + |E_{SB-}|^2 \\ &+ 2\mathbf{Re}\{\ E_{SB+}E^*_{SB-}e^{2i\Omega t}\ \} \\ &+ 2\mathbf{Re}\{\ (E_C E^*_{SB-} + E_{SB+}E^*_C)e^{i\Omega t}\ \} \end{aligned} \tag{2.27}$$

The last term is referred to as the *beat note* between the carrier signal and the sidebands. To extract the term at the modulation frequency, one can use a mixer which is an analog device that outputs the product of two inputs. Usually, the same oscillator that was used to modulate the input beam can be one of the mixer inputs, $\cos(\Omega t)$, so that the demodulated signal is

$$\begin{aligned} I_{\text{Demod}} &\propto \left[4\pi J_0(\beta)J_1(\beta)\frac{\ell_+}{\lambda}\sin(k_\Omega \Delta\ell)\ h_+\right]\left[\cos(\Omega t)\sin(\Omega t + \phi_{Demod})\right] \\ &\propto \left[4\pi J_0(\beta)J_1(\beta)\frac{\ell_+}{\lambda}\sin(k_\Omega \Delta\ell)\ h_+\right]\left[\sin(\phi_{Demod}) + \sin(2\Omega t + \phi_{Demod})\right] \end{aligned} \tag{2.28}$$

where ϕ_{Demod} is the phase that can be set by the user in order to account for extra phase shifts (ie. longer cables). After the mixer, there will be signals at DC, Ω, 2Ω and so on. However, the part that is linear in the gravitational wave amplitude will be at DC so a low-pass filter will allow the final signal to dominate [9]:

$$S = 4\pi J_0(\beta)J_1(\beta)\frac{\ell_+}{\lambda}\sin(k_\Omega \Delta\ell)\sin(\phi_{Demod})\ h_+ \tag{2.29}$$

This shows that a RF detection technique will be linear in GW signal with no large DC offset. Setting the carrier on a null point means $\Delta\ell = \frac{k_\Omega}{k}\frac{\pi}{2}$ and allows the designer to optimize the Schnupp asymmetry length to get the best signal for some modulation frequency. This type of readout scheme was used in Enhanced LIGO and is called heterodyne detection, where the sideband fields are produced by an EOM and its efficacy depends on the local oscillator's stability [47]. In contrast, the Advanced LIGO scheme uses a homodyne detection [55] method called "DC-Readout". Here, the oscillator field is produced by slightly offsetting the arms away from the dark fringe and letting a small amount of carrier light through the antisymmetric port. A gravitational wave will induce sidebands on the carrier such that the beat note between the two fields will have a linear signal in gravitational wave strain. This

method benefits from naturally being co-aligned and mode matched with the signal field. All techniques follow the same logic of beating the field containing useful information with a reference field to extrapolate a linear signal but the differences come from technical noise such as laser intensity fluctuations and effective quantum noise.

2.1.2 Fabry-Perot Cavities

There are two ways to improve the LIGO detectors: one is to increase the response from gravitational waves and the other is to decrease the noise contributions. From equation 1.12, the gravitational wave signal is proportional to the optical path length that the photon travels, which means the most straightforward method of increasing the sensitivity is to make the arms as long as possible (up to the null point described by equation 1.13). There are two methods to achieve this: a Herriott delay line or a Fabry-Perot resonator, the differences between each method is shown in Figure 5. At the time of writing this thesis, all modern gravitational wave detectors use the latter method.

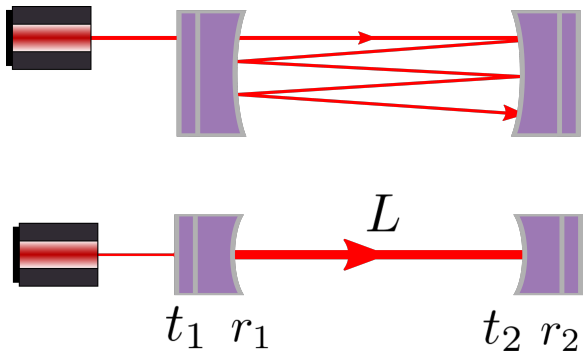

Figure 5 : Delay Line (top) vs Fabry Perot (bottom)

A Fabry-Perot cavity is an optical system comprised of two or more partially transmitting mirrors with one laser input. To create such a resonator, the user must design a system so that once the electric field has made one round trip within the optical system, the phase of the beam is the same as when it started such that it constructively interferes. This is done by changing the cavity length, which may seem simple conceptually but in practice, controlling and sensing any optical cavity comes with a few challenges.

To start understanding the longitudinal degree of freedom, consider a two mirror

system in Figure 5 which is separated by a length L with reflection and transmission coefficients: $r_1,\ t_1,\ r_2,\ t_2$. Starting with a plane wave at the input mirror with amplitude E_0, the beam will enter the cavity and propagate back between the two mirrors. The reflected, transmitted, and circulating fields [77], which are a result of the geometric series, can be described as

$$E_{\text{REFL}} = r_{FP}E_0 = \left(-r_1 + \frac{t_1^2 r_2 e^{-i2kL}}{1 - r_1 r_2 e^{-i2kL}} \right) E_0 \tag{2.30}$$

$$E_{\text{TRAN}} = t_{FP}E_0 = \left(\frac{t_1 t_2 e^{ikL}}{1 - r_1 r_2 e^{-i2kL}} \right) E_0 \tag{2.31}$$

$$E_{\text{CIRC}} = c_{FP}E_0 = \left(\frac{t_1}{1 - r_1 r_2 e^{-2ikL}} \right) E_0 \tag{2.32}$$

The above fields are all highly dependent on the round trip phase accumulated within the cavity which becomes resonant when the length is $L = n\lambda/2$. While on resonance, the circulating coefficient in the cavity is maximized such that the gain is

$$\text{Gain} = c_{FP}^2|_{\text{resonating}} = \left(\frac{t_1}{1 - r_1 r_2} \right)^2 \tag{2.33}$$

Notice that the fields are dependent on the cavity length and laser frequency, $2kL$, so one might naively determine that modulating the two parameters independently cause the same effect. However, when both are changing by large amounts, they are related by a frequency dependent transfer function [63]

$$C(\omega)\frac{\Delta\omega}{\omega} = -\frac{\Delta L}{L} \tag{2.34}$$

where $C(\omega) = \frac{1-e^{-2i\omega L/c}}{2i\omega L/c}$. It is only when the cavity is on resonance that the frequency and length variations are related by $\frac{\Delta w}{w} = -\frac{\Delta L}{L}$. Depending on the relative reflection coefficients of the input and output mirrors, the fields on resonance will be different in amplitude. For example, in the LIGO 4 km arms, the end test masses are highly reflective with a transmission of about 4 parts per million while the input test masses have a transmission of about 0.015. This means that the arm cavities are very much over-coupled and almost all of the light reflects back towards the beamsplitter. It is important to understand the Fabry-Perot response while sweeping through either the

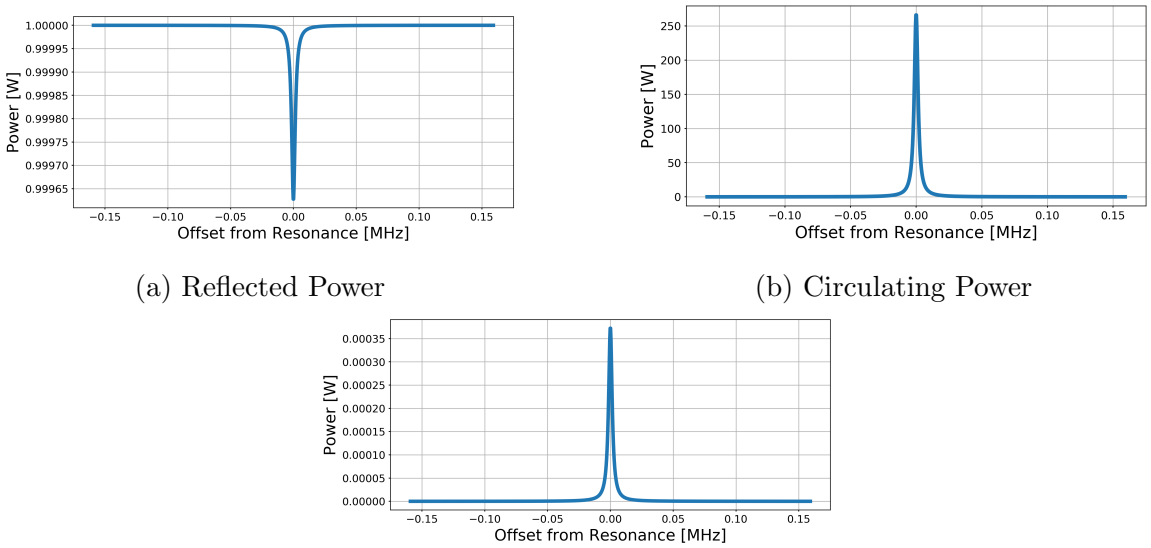

(a) Reflected Power

(b) Circulating Power

(c) Transmitted Power

Figure 6 : **The reflected, circulating, and transmitted powers for a single Fabry-Perot cavity.** The optical properties used represent the Hanford 4 kilometer x-arm [28], which is a highly over-coupled cavity [9] so almost all of the light reflects toward the beamsplitter. The input power is normalized to 1 Watt to show the relative gain of the circulating power.

laser frequency or cavity length and measuring the reflected (or transmitted) fields, there are features of the power spectrum which relate directly to the cavity's physical properties.

The finesse describes the line width of the resonant peak and is a function of r_1 and r_2. A higher finesse will mean the line width is smaller and the peak height taller compared to a lower finesse cavity:

$$\mathbb{F} = \frac{\pi\sqrt{r_1 r_2}}{1 - r_1 r_2} \tag{2.35}$$

The cavity storage time, τ_s, describes how long it takes the power circulating in the cavity to decay by a factor of $1/e$ if the laser suddenly turns off,

$$\tau_s = \frac{L}{c\pi}\,\mathbb{F} \tag{2.36}$$

The pole frequency, f_{pole}, is when the magnitude of the cavity's transfer function (see

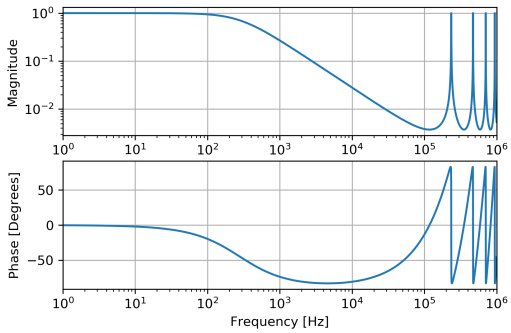

(a) Transfer function with respect to cavity length offset

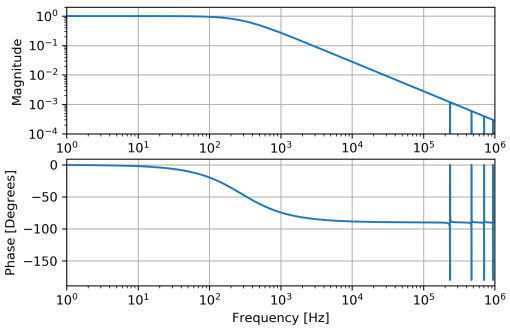

(b) Transfer function with respect to laser frequency offset.

Figure 7 : Bode plots of a linear Fabry-Perot response in reflection.

Figure 7) reaches 3dB below the DC level:

$$f_{\text{pole}} = \frac{1}{4\pi\tau_s} \tag{2.37}$$

The free spectral range,f_{FSR}, is the frequency span from one resonant peak to the next.

$$f_{\text{FSR}} = \frac{c}{2L} \tag{2.38}$$

It is useful to understand the power circulating as a function of our defined parameters slightly off resonance by a length of ΔL

$$P_{cav} = |c_{FP}|^2 = \frac{\text{Gain}}{1 + \left(\frac{2\mathbb{F}}{\pi}\right)^2 \sin^2(k\Delta L)} \tag{2.39}$$

Stable resonance requires the beam to stay spatially confined on the mirrors, meaning a resonant cavity does not have a continually growing beam size in steady-state operation. In order to prove that an optical cavity is geometrically stable, it is useful to introduce the matrices that describe a periodic optical system which is explicitly derived in Appendix A. A Fabry Perot cavity that is separated by distance L with spherical mirrors that have radii of curvature R_1 and R_2 will need to satisfy

$$0 \leq \left(1 - \frac{L}{R_1}\right)\left(1 - \frac{L}{R_2}\right) \leq 1 \tag{2.40}$$

in order to be stable.

LIGO uses optical cavities for a number of reasons: Firstly, the round trip phase of the gravitational wave is amplified by the finesse (equation 2.35) of the 4 kilometer arm cavities, therefore increasing the sensitivity. Secondly, the input and output of the interferometer's Gaussian beam mode can be refined by only allowing the fundamental mode of the laser to resonate (input and output mode cleaners). Thirdly, Advanced LIGO uses a dual-recycled Michelson interferometer which means the symmetric port has a mirror inserted to resonate the light reflected from the Fabry Perot arms (power recycling) and another mirror shapes the frequency response of the differential cavity pole at the anti-symmetric port (signal recycling).

Achieving Resonance in an Optical Cavity

Described above are the theoretical constructs for a Fabry-Perot cavity, but the question remains, how does one practically construct a resonant optical cavity? The answer comes from using a heterodyne sensing scheme similar to the one described in Section 2.1.1. Except in this case the optical system is not a Michelson interferometer but rather a two mirror cavity and can apply to a number of different geometries such as triangular or bow-tie cavities.

Starting with an input laser and EOM (electro-optical modulator) that imparts upper and lower sidebands at a modulation frequency Ω, the user injects three beams into the optical system described in Equation 2.22. When placing a photodetector on the reflection port, one should see the cavity's effect on each of the three electric fields.

$$E_{FP,out} = E_C + E_{SB+} + E_{SB-} = \begin{pmatrix} r_C \\ r_{SB+} \\ r_{SB-} \end{pmatrix} \begin{pmatrix} E_{C,in} & E_{SB+,in} & E_{SB-,in} \end{pmatrix} \tag{2.41}$$

$$r_C = -r_1 + \frac{t_1^2 r_2 e^{-i2kL}}{1 - r_1 r_2 e^{-i2kL}} \tag{2.42}$$

and

$$r_{SB\pm} = -r_1 + \frac{t_1^2 r_2 e^{-i2(k+k_\Omega)L}}{1 - r_1 r_2 e^{-i2(k+k_\Omega)L}} \tag{2.43}$$

where the reflection coefficients follow equation 2.30. Because sidebands are frequency

shifted, they will effectively *see* a different cavity than the carrier and the total phase accumulated by the two fields will be different. To make a good reference for the resonant carrier beam, the modulation frequency Ω, is chosen such that sidebands are anti-resonant, which effectively means they are rejected from entering the cavity.

The formalism to read out the error signal is shown in Equation 2.27 where a photodetector in reflection (see Figure 8) reads out the sum of fields squared and demodulates to get the error signal which will be linearly proportional to the laser frequency and cavity length [9].

$$\text{Error Signal} \propto \frac{L\mathbb{F}}{\lambda}\left[\frac{\delta w}{w} + \frac{\delta L}{L}\right] \tag{2.44}$$

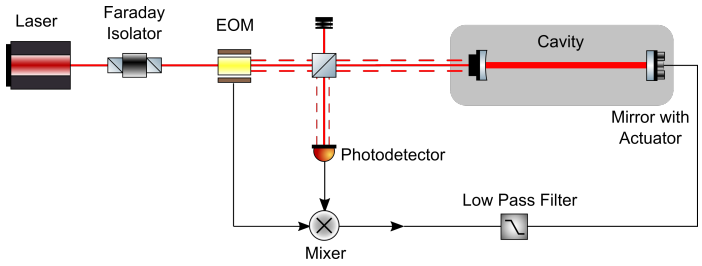

Figure 8 : **Control scheme for an optical cavity.** The electric fields in reflection provide the error signal when mixed with the local oscillator and then gets low-passed for a DC signal to drive the end mirror which will control the length of the cavity, see Figure 9.

2.1.3 Fabry-Perot Michelson

Using an optical cavity to increase the number of bounces along the 4 kilometer arms will amplify the gravitational wave signal but it will also shape the frequency dependence of the sensitivity as well. This has already been alluded to in section 1.2 where the overall increase in arm length will tune the response function of equation 1.13. The same concept applies to integrating the use of Fabry-Perot arms with a Michelson interferometer and looking at the signal at the antisymmetric port as a function of gravitational wave frequency. Previously in section 2.1.1, it was shown that the heterodyne RF detection technique required beating the sidebands with a carrier field that contains the gravitational wave information. Another method known as homodyne detection uses signal sidebands beating with a reference carrier field as a valid way of measuring the signal of interest. In fact, Advanced LIGO employs

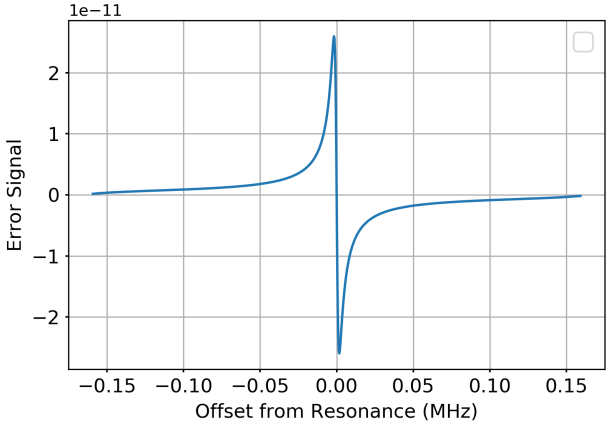

Figure 9 : **Pound-Drever-Hall (PDH) error signal in reflection of a Fabry Perot cavity.** By modulating the frequency (or length) close to the zero offset point, the error signal is linear. However, if the actuation is too far away from the lock point, the signal becomes highly non-linear. Within this regime where the error signal is not useful, the control output to an actuator must wait until the error signal comes close enough to linear before triggering on. Generally, this is done by sweeping the frequency or length offset until the cavity becomes roughly resonant and then closing the loop.

a specific type of homodyne detection called DC readout [47][31]. The idea is that the carrier field will resonant in the arms but will be slightly modulated due to a gravitational wave which will create audio frequency sidebands imparted on the field. A small offset in the arm lengths will allow some of the carrier light to leak into the antisymmetric port in order to provide the reference field.

Figure 10 shows an input electric field E_0 incident on a 50/50 beamsplitter which then enters two orthogonal arm cavities of length L_x and L_y. Notice that the distance from the beamsplitter to the input couplers for both arms is denoted by l_x and l_y, this is to allow the description of the DARM offset which is analogous to the Schnupp asymmetry described in section 2.1.1. After partially transmitting and reflecting at the beamsplitter, the fields will resonate in each of the arm cavities and obey the reflectivity relations described by equation 2.30. Upon recombining at the beamsplitter, the antisymmetric port electric field will be related to the arm fields by,

$$E_{\mathrm{AS}} = \frac{1}{\sqrt{2}}[E_x^{\mathrm{ARM}} + E_y^{\mathrm{ARM}}] \tag{2.45}$$

where $E_i^{\mathrm{ARM}} = E(\omega) \pm [E(+\omega_{\mathrm{GW}}) + E(-\omega_{\mathrm{GW}})] \sin k\delta l$ represents the reflected fields for

the x and y arms which contain the carrier(first term) and GW signal sidebands(last two terms). In this case, the gravitational wave sidebands are a single frequency for simplicity but this analysis will work for all frequencies spanning the LIGO sensitivity band. The antisymmetric port will only be sensitive to the differential motion between the arm cavities, which means the gravitational wave sidebands in the x-arm will be out of phase with the y-arm. Also it is important to note that inserting a DC microscopic length shift of a few picometers represented by $\delta l = l_x - l_y$ allows for some carrier leakage field to propagate towards the antisymmetric port which creates the static reference to form a beat note with the signal sidebands. In practice, this is achieved by introducing a static offset between the x and y arm cavity lengths, $L_x \neq L_y$, this is referred to as a differential arm (DARM) offset.

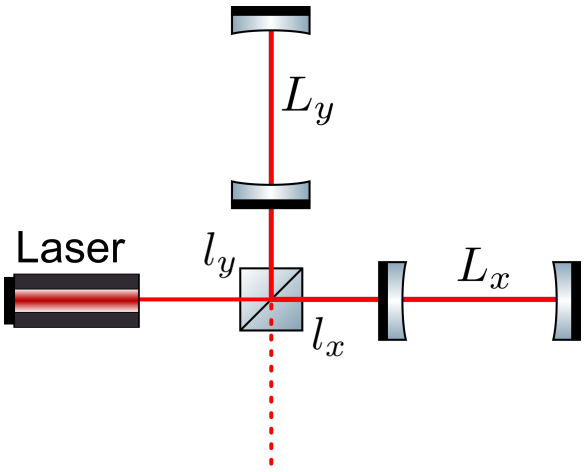

Figure 10 : Michelson with Fabry Perot arms

For the carrier field, the amplitude of reflection is simple because the LIGO arms are a strongly over-coupled cavity operating on resonance therefore

$$E(\omega) = \frac{E_0}{\sqrt{2}}\left(-r_1 + \frac{t_1^2 r_2}{1 - r_1 r_2}\right) \approx -\frac{E_0}{\sqrt{2}} \tag{2.46}$$

The sidebands are a different story because the modulation caused by the gravitational wave slightly moves the field off resonance. Imagine the carrier circulating in the arms and then suddenly, a disturbance due to a gravitational wave differentially displaces the end mirrors at a frequency ω_{GW} by an amount ΔL_-. By using the same formalism as the expansion of a modulated field in equation 2.22, the sideband fields

can be described by,

$$\begin{aligned} E(\pm\omega_{\rm GW}) &= \left[\frac{t_1}{1-r_1r_2e^{-2ikL_+}}\right]\frac{E_0}{\sqrt{2}}\left[\frac{t_1}{1-r_1r_2e^{-2i(kL_+\pm\omega_{\rm GW}\frac{L_+}{c})}}\right]ik\Delta L_- \\ &= \left[\frac{t_1^2}{1-r_1r_2}\right]\frac{E_0}{\sqrt{2}}\left[\frac{1}{1-r_1r_2e^{\pm 2i\omega_{\rm GW}\frac{L_+}{c}}}\right]ik\Delta L_- \end{aligned} \tag{2.47}$$

The first bracket is the circulating field of the carrier signal amplified by the Fabry Perot cavity and the second bracket is the circulating field slightly off resonance due to the gravitational wave frequency offset. Notice that the static arm length is denoted by $L_+ = \frac{L_x+L_y}{2}$, which refers to the common arm length for the two Fabry-Perot arms. Setting the fields to resonate already simplifies the equation but it is also reasonable to approximate the gravitational wave as a weak signal and expand the exponential $e^{-2i\omega_{\rm GW}\frac{L_+}{c}} \approx 1 - 2i\omega_{\rm GW}\frac{L_+}{c}$. This transforms the signal sideband field into a simpler form,

$$E(\pm\omega_{\rm GW}) \approx \left[\frac{t_1}{1-r_1r_2}\right]^2\frac{E_0}{\sqrt{2}}\left[\frac{1}{1\pm i\frac{\omega_{\rm GW}}{\omega_p}}\right]ik\Delta L_- \tag{2.48}$$

where $\omega_p = \frac{1-r_1r_2}{r_1r_2}\frac{c}{2L_+}$ is the differential pole frequency; notice that it matches the single arm cavity pole so a Fabry-Perot Michelson interferometer has the same frequency dependence.

The photodiode signal at the antisymmetric port is proportional to the beat note between the carrier and signal sideband in the audio frequency band with a demodulation phase ϕ_D,

$$\begin{aligned} S &\propto 2[E(\omega)E^*(+\omega_{\rm GW}) + E(-\omega_{\rm GW})E^*(\omega)]\sin(k\delta l)\sin(\phi_D) \\ &\propto 4kE_0^2\left[\frac{t_1}{1-r_1r_2}\right]^2\left[\frac{1}{1-i\frac{\omega_{\rm GW}}{\omega_p}}\right]\sin(k\delta l)\sin(\phi_D)\Delta L_- \\ &\propto E_0^2\,\frac{8\pi L_+}{\lambda}\left[\frac{t_1}{1-r_1r_2}\right]^2\left[\frac{1}{1-i\frac{\omega_{\rm GW}}{\omega_p}}\right]\sin(k\delta l)\sin(\phi_D)h_{\rm GW} \end{aligned} \tag{2.49}$$

where the length disturbance ΔL_- was transformed to originate from a gravitational wave signal $k\Delta L_- = \frac{2\pi L_+}{\lambda}h_{\rm GW}$. The response of this particular interferometer to differential arm length motion is linearly proportional to the gravitational wave amplitude as well as the input power $P_0 \propto E_0^2$, but there is also a frequency dependent component which is the same as that of a single Fabry-Perot cavity. This acts like a

low pass filter above the corner frequency colloquially called the DARM cavity pole. By adding resonators, there is also a DC amplification of the signal by a factor of $\left[\frac{t_1}{1-r_1 r_2}\right]^2$, which is the gain of a linear Fabry-Perot cavity (≈ 268 for Advanced LIGO optics [28]).

2.1.4 Power-Recycled Fabry-Perot Interferometers

If the interferometer is operating such that the intensity at the antisymmetric port is close to null, conservation of energy requires that the arm powers will reflect back towards the input laser. Fritschel et al. [48] [45] showed the effects of adding a partially reflecting mirror increases the Michelson optical gain for both the sideband and carrier fields. Section 2.1.3 showed that the Michelson interferometer with Fabry Perot arms can be represented by a single cavity response. Therefore it is useful to model a power recycled interferometer by using a coupled cavity approach where one of the mirrors is replaced with the total reflected field of the Fabry-Perot Michelson on a bright fringe. Here the reflectivity and transmissivity of the power recycling mirror (PRM) is denoted by r_p and t_p, respectively.

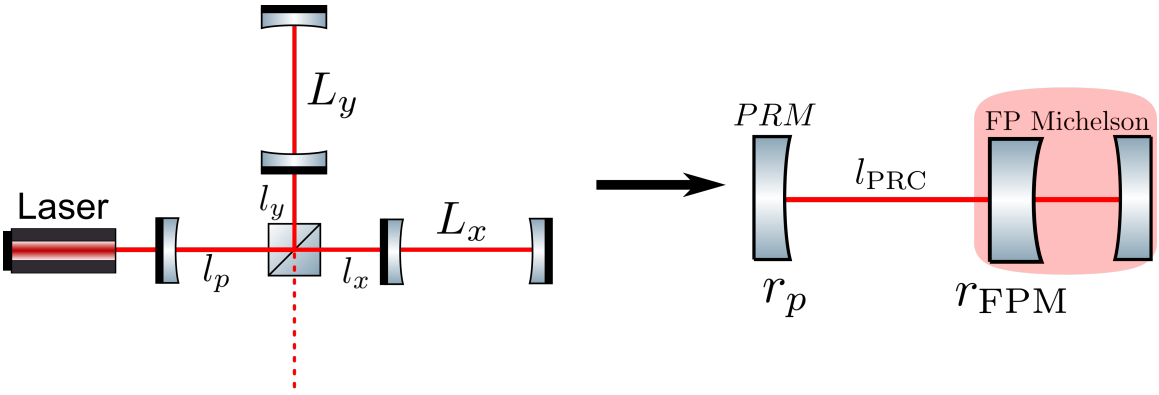

Figure 11 : **A power recycled Fabry-Perot interferometer.** Adding a mirror at the symmetric port forms another resonator called the power recycling cavity (PRC) where the distance between from the power recycling mirror (PRM) to the beamsplitter is denoted by l_p and the reflectivity is r_p. The interferometer usually operates with the symmetric port on the bright fringe and the reflection from a Fabry-Perot Michelson can be represented by a single reflectivity, r_{FPM} while the length l_{PRC} is the average distance from PRM to the ITMs. This model makes handling the mathematics of a coupled cavity much more tangible.

In this configuration, the effective length of the cavity is the average path between

the power recycling mirror and the high reflectivity surfaces of the input test masses,

$$l_{\mathrm{PRC}} = l_{\mathrm{p}} + \frac{l_x + l_y}{2} \tag{2.50}$$

The circulating power in the cavity is given by equation 2.32 but uses the reflectivity of arm cavities,

$$E_{\mathrm{PRC}} = \frac{t_p}{1 - r_p r_{\mathrm{FPM}} e^{-2ikl_{\mathrm{PRC}}}} E_{\mathrm{in}} \tag{2.51}$$

where $r_{\mathrm{FPM}} \approx 1 - \frac{\mathbb{F}}{\pi}\mathcal{L}_{\mathrm{ARM}}$ for high finesse ($\mathbb{F}$) arm cavities and the round trip arm losses are denoted by $\mathcal{L}_{\mathrm{ARM}}$ which include scattering, mode mismatch, absorption, and any other effect which is not directly reflected or transmitted from optics. This is a valid approximation for the Advanced LIGO since their values for arm finesse can be around 450 or higher depending on the losses. This means the circulating power in the recycling cavity while on resonance can be expressed by

$$P_{\mathrm{PRC}} = \frac{1 - r_p^2}{\left[1 - r_p(1 - \frac{\mathbb{F}}{\pi}\mathcal{L}_{\mathrm{ARM}})\right]^2} P_{\mathrm{in}} \tag{2.52}$$

By taking the derivative with respect to r_p and setting to zero, the optimal power recycling tuning is dependent on the round trip loss,

$$r_{\mathrm{opt}} = 1 - \frac{\mathbb{F}}{\pi}\mathcal{L}_{\mathrm{ARM}} \tag{2.53}$$

so it important to keep the arm cavity losses as low as possible and this also limits the ability to increase the finesse.

Adding a power recycling mirror will be equivalent to introducing higher power into the arm cavities but it will not shape the gravitational wave sideband frequency dependence in any other way. This can be reasoned qualitatively by imagining the signal sidebands that get created in the arm cavities and propagate to the beam splitter where they will combine, however, the stretching and squeezing from the gravitational wave pattern will make the x-arm shorter while lengthening the y-arm and vice versa. This makes the anti-symmetric port transmissive to the signal sidebands but the carrier field which mostly gets reflected to the symmetric port will see the power recycling amplification. This means the beat note between the static carrier

field and gravitational wave signal for a power recycled Fabry-Perot interferometer is

$$S_{\mathrm{PRFP}} \propto E_0^2 \, \frac{8\pi L_+}{\lambda} \sqrt{g_{\mathrm{PRC}}} \left[\frac{t_1}{1 - r_1 r_2} \right]^2 \left[\frac{1}{1 - i \frac{\omega_{\mathrm{GW}}}{\omega_p}} \right] \sin\left(k\delta l\right) \sin\left(\phi_D\right) h_{\mathrm{GW}} \tag{2.54}$$

where $g_{\mathrm{PRC}} = P_{\mathrm{PRC}}/P_{\mathrm{in}}$ is the power recycling gain.

2.1.5 Dual-Recycled Fabry-Perot Interferometers

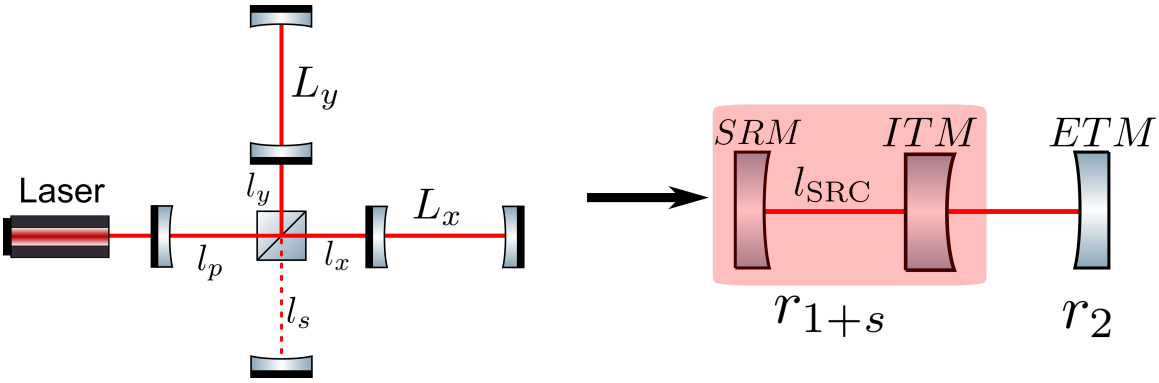

Figure 12 : **A dual recycled Fabry-Perot interferometer.** The left diagram is similar to Figure 11 but with a signal recycling mirror (SRM) placed at the anti-symmetric port a distance l_s away from the beamsplitter. Similar to the analysis done when adding power recycling, collapsing the SRM and ITM into a single mirror system that has one reflectivity, r_{1+s} and an average length $l_{\mathrm{SRC}} = \left(l_{\mathrm{s}} + \frac{l_x + l_y}{2}\right)$ will simplify the coupled cavity picture. The round trip phase of the SRC will effectively increase or decrease r_{1+s} which will shape the frequency dependence of the interferometer's optical gain for gravitational-wave sidebands.

One of the biggest changes made between initial and Advanced LIGO was the addition of a signal recycling mirror at the antisymmetric port (see Figure 12). In the previous section, it was shown that the gravitational wave sensitivity was improved by adding a power recycling cavity to increase the effective input power entering the arm cavities. Adding another partially reflecting optic called the signal recycling mirror (SRM) at the antisymmetric port to create a resonant cavity will shape the interferometer's response to gravitational waves. This allows for some flexibility in optimizing the instrument for specific sources such as binary neutron stars, but it also creates a more broadband response at higher frequencies while allowing the arm cavity finesse and/or power recycling to impart more power.

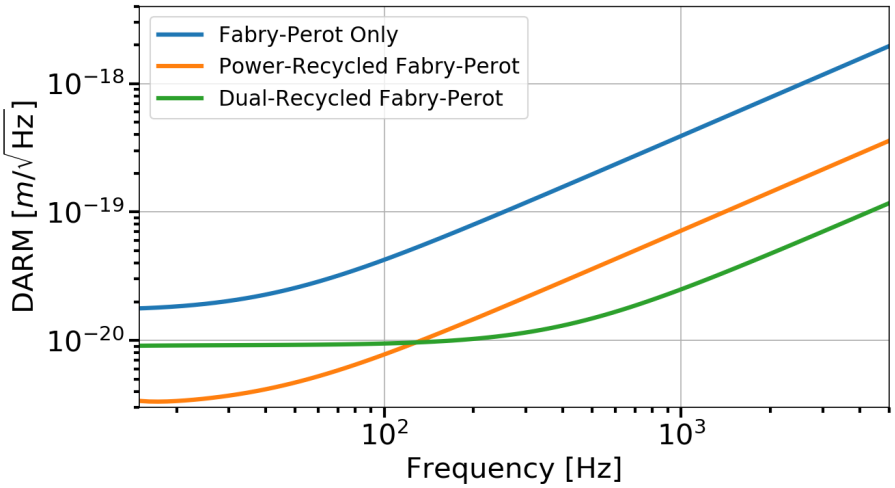

Figure 13 : **Comparing the shot noise limited differential arm spetra for different interferometer configurations.** Here, the simulation was ran with FINESSE [71] using the Advanced LIGO optical parameters [12].

A nice way to model the effect of signal recycling on the gravitational wave sidebands is to combine the SRM and arm cavity input test mass to create a combined mirror that is dependent on the round trip phase, ϕ_s of the signal recycling cavity. The SRM will have a reflectivity and transmissivity equal to r_s and t_s, respectively, so the combined mirror will have a reflectivity and transmissivity equal to

$$r_{1+s} = \frac{r_1 - r_s e^{-2i\phi_s}}{1 - r_1 r_s e^{-2i\phi_s}} \tag{2.55}$$

$$t_{1+s} = \frac{t_1 t_s e^{i\phi_s}}{1 - r_1 r_s e^{-2i\phi_s}} \tag{2.56}$$

where $\phi_s = k\left(l_s + \frac{l_x + l_y}{2}\right) = k\, l_{\text{SRC}}$ is the average signal recycling length. Plugging this into equation 2.47 in place of the input test mass reflectivity shows that the cavity pole is directly affected by the signal recycling properties, namely, the SRM reflectivity and the microscopic detuning of the length. The field propagating to the antisymmetric port is in transmission of the signal recycling cavity which is accounted

for with the last bracketed term.

$$\begin{aligned} E_{\mathrm{AS}}(\pm\omega_{\mathrm{GW}}) &= \left[\frac{t_1^2}{1-r_1 r_2}\right]\frac{E_0}{\sqrt{2}}\left[\frac{1}{1 \pm r_{1+s} r_2 e^{-2i\omega_{\mathrm{GW}}\frac{L_+}{c}}}\right]\left[\frac{t_1 t_s e^{i\phi_s}}{1-r_1 r_s e^{-2i\phi_s}}\right] ik\Delta L_- \\ &\propto \left[\frac{\text{Constant}}{1 \pm 2i\frac{r_{1+s}r_2}{1-r_{1+s}r_2}\omega_{\mathrm{GW}}\frac{L_+}{c}}\right] \\ &\propto \left[\frac{\text{Constant}}{1 \pm i\omega_{\mathrm{GW}}/\omega_{\mathrm{DR}}}\right] \end{aligned} \tag{2.57}$$

Here, the frequency dependence of the differential cavity pole with dual recycling is denoted by

$$\begin{aligned} \omega_{\mathrm{DR}} &= \frac{1-r_{1+s}r_2}{r_{1+s}r_2}\frac{c}{2L_+} \\ &= \frac{1-r_1 r_s e^{-2i\phi_s}}{(r_1 - r_s e^{-2i\phi_s})r_2} - 1 \end{aligned} \tag{2.58}$$

The carrier field will also see a gain from the signal recycling cavity equal to

$$\sqrt{g_{\mathrm{SRC}}} = \frac{t_s}{1 + r_s r_{\mathrm{FPM}} e^{-2i\phi_s}} \tag{2.59}$$

The equations above show that the gravitational wave sideband and carrier fields will see the signal recycling cavity effects differently and the responses are highly sensitive to the length detuning of ϕ_s. Putting all the pieces together to get the dual recycled Fabry-Perot interferometer response to gravitational waves,

$$S_{\mathrm{DRFP}} \propto E_0^2 \, \frac{8\pi L_+}{\lambda}\sqrt{g_{\mathrm{PRC}}}\,\sqrt{g_{\mathrm{SRC}}}\,g_{\mathrm{ARM}}\left[\frac{1}{1 - i\frac{\omega_{\mathrm{GW}}}{\omega_{\mathrm{DR}}}}\right]\sin(k\delta l)\sin(\phi_D)h_{\mathrm{GW}} \tag{2.60}$$

The previous sections only considered the effect of Fabry-Perot cavities and recycling mirrors at the antisymmetric port (AS) due to the differential length change (DARM) of the 4 kilometer arms but the Advanced LIGO interferometer has a few lengths which are actively controlled. The other degrees of freedom include the common arm length (CARM), the power recycling length (PRCL), and signal recycling length (SRCL). These signals are sensitive at ports other than AS, such as in reflection of PRM (REFL) and a pick off port in the power recycling cavity (POP). A good reference for what signals are expected at these important readout points can be found in [57] [58] [59].

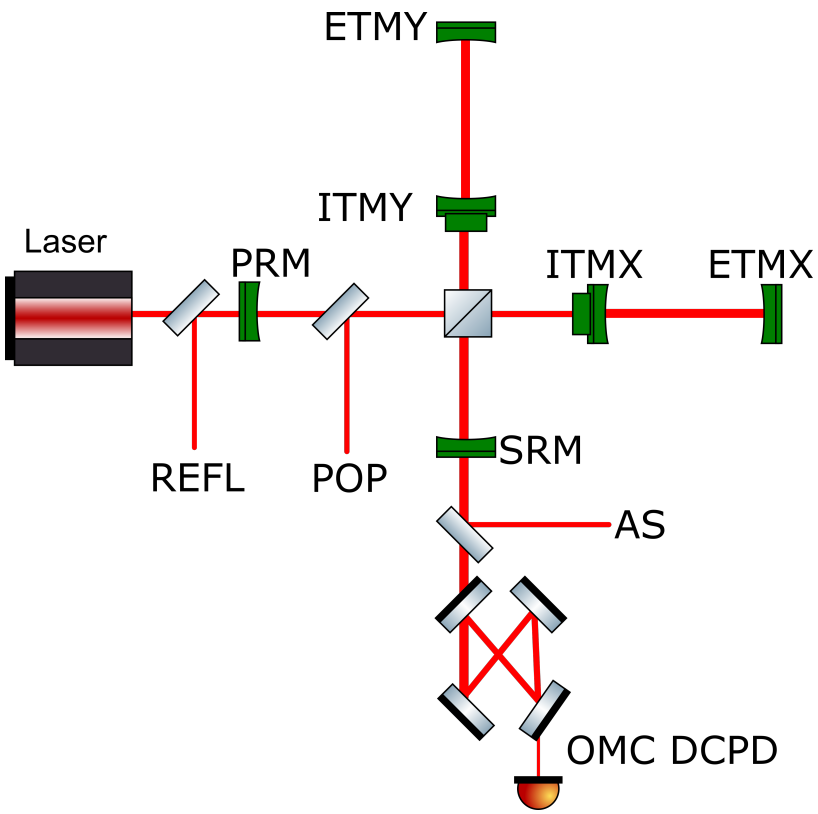

Figure 14 : **Important sensor ports for Advanced LIGO** The green optics are used to distinguish the main interferometer mirrors from pick off mirrors which sense various degrees of freedoms for sensing and controls.

2.2 Fundamental Noise Sources

The preceding sections described ways to increase the response of LIGO to gravitational waves; equally as important is the science of characterizing and reducing the noise contributions from everything that is not gravitational waves to optimize the sensitivity.

Quantum Noise

In quantum mechanics [82], solving the Schrödinger equation for the harmonic oscillator using creation ($\hat{a^\dagger}$) and annihilation ($\hat{a}$) operators leads to the existence of a non-zero energy ground state which has variances in momentum and position related by the Heisenberg uncertainty principle. When it comes to electromagnetic fields, the pair associated with the uncertainty principle is the amplitude and phase of the laser

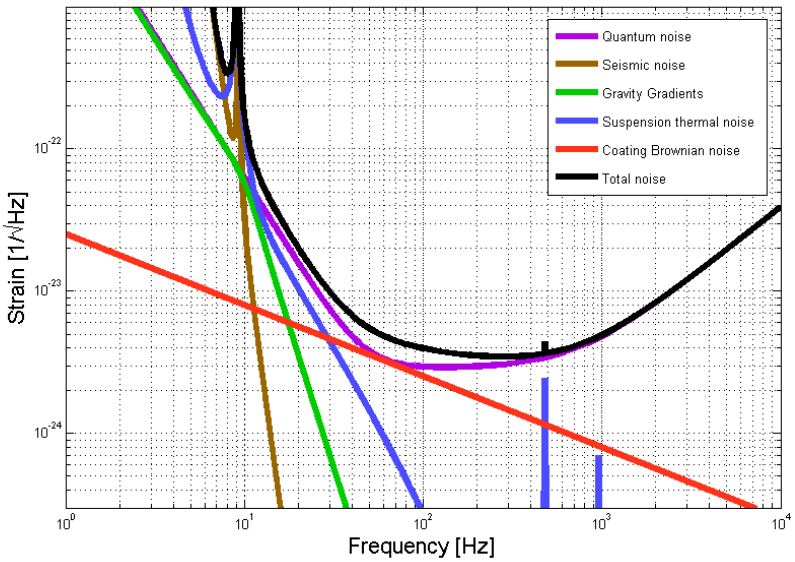

Figure 15 : **Noise budget from GWINC (Gravitational Wave Interferometer Noise Calculator)**

beam.

As a result, one of the main noise sources that is limiting LIGO's sensitivity comes from the fluctuations of quantum vacuum entering the anti-symmetric port and coupling to the input laser. A quantum mechanical description of an interferometer was constructed by Caves [22][23] [24], where he used electric field operators to show that vacuum fluctuations are the cause of radiation pressure and shot noise in a simple interferometer (no resonant cavities). The following analysis below will also be simplified in this way but is reasonably close in estimating the amount radiation pressure and shot noise. For studies that take into account more complicated interferometer configurations with resonant cavities, refer to Buonanno, Chen, and Kimble [20] [26] [60].

Quantum states: A solution to the quantum harmonic oscillator in the energy eigenbasis employs the annihilation and creation operators, $\hat{a}^\dagger$ and $\hat{a}$, to factorize the Hamiltonian [82] [51]

$$\hat{H} = \hbar w(\hat{N} + 1/2) \tag{2.61}$$

where $\hat{N} = \hat{a}^\dagger\hat{a}$ is the number operator. When using this formalism to create a coherent electromagnetic field, it is useful to define a unitary operator that displaces

the vacuum state [49]:

$$\hat{D} \equiv \hat{D}(\alpha) \equiv \exp(\alpha \hat{a}^\dagger - \alpha^* \hat{a}) = e^{-\frac{|\alpha|^2}{2}} e^{\alpha \hat{a}^\dagger} e^{\alpha^* \hat{a}} \tag{2.62}$$

and has the properties,

$$\begin{aligned} \hat{D}(\alpha) = \hat{D}^{-1}(\alpha) &= \hat{D}(-\alpha) \\ \hat{D}^\dagger \, \hat{a} \, \hat{D} &= \hat{a} + \alpha \\ \hat{D}^\dagger \, \hat{a}^\dagger \, \hat{D} &= \hat{a}^\dagger + \alpha^* \end{aligned} \tag{2.63}$$

When applying the displacement operation on the vacuum state, the resultant vector has an amplitude α and follows the same uncertainty distribution as an unperturbed vacuum vector,

$$|\alpha\rangle = \hat{D} \, |0\rangle = e^{-\frac{|\alpha|^2}{2}} e^{\alpha \hat{a}^\dagger} \, |0\rangle \tag{2.64}$$

Radiation Pressure

Power fluctuations in the main laser causes radiation pressure effects on the test masses, however, if the 50/50 beamsplitter is perfect, then the momentum transfer to each test mass will result in a common length change and will not vary the intensity at the antisymmetric port (or the symmetric port for that matter). The coupling of radiation pressure into the interferometer is shown below to come directly from vacuum fluctuations.

Consider plane wave waves entering the interferometer from both the symmetric and anti-symmetric ports. This method is similar to the input-output methods of section 2.1.1, however, the difference being that the beamsplitter will couple the electric fields from the input laser and quantum vacuum.

The electric fields combine at the beamsplitter from both ports and add linearly,

$$E_x = \frac{1}{\sqrt{2}} \left[i E_0 + E_{AS,in} \right] \tag{2.65a}$$

$$E_y = \frac{1}{\sqrt{2}} \left[E_0 + i E_{AS,in} \right] \tag{2.65b}$$

where E_0 is the input field from the laser and $E_{AS,in}$ is the field from the anti-symmetric port. The electric fields will travel down each arm and strike the mirrors

with intensities denoted by,

$$|E_x|^2 = \frac{1}{2}\Big[|E_0|^2 + |E_{AS,in}|^2 + i(E_0 E^*_{AS,in} - E^*_0 E_{AS,in})\Big] \tag{2.66a}$$

$$|E_y|^2 = \frac{1}{2}\Big[|E_0|^2 + |E_{AS,in}|^2 - i(E_0 E^*_{AS,in} - E^*_0 E_{AS,in})\Big], \tag{2.66b}$$

Therefore, differential momentum transfer between the two masses will be equal to the differences in intensities between the two arms:

$$\begin{aligned} \mathbf{P} &= \frac{2\hbar\omega}{c}\Big(|E_x|^2 - |E_y|^2\Big) \\ &= \frac{2\hbar\omega}{c}\Big(E_0 E^*_{AS,in} - E^*_0 E_{AS,in}\Big) \\ \Rightarrow \hat{\mathbf{P}} &= \frac{2\hbar\omega}{c}\Big(\hat{a}_1^\dagger \hat{a}_2 - \hat{a}_2^\dagger \hat{a}_1\Big) \end{aligned} \tag{2.67}$$

The last part of equation 2.67 replaces the classical electric fields with creation and annihilation operators for the symmetric input mode ($\hat{a}_1^\dagger$, $\hat{a}_1$) and antisymmetric input mode ($\hat{a}_2^\dagger$, $\hat{a}_2$) modes. Recall that there is a well established convention denoting the wave function of the two dimensional modes of the quantum harmonic oscillator [49], $|\alpha, \beta\rangle$, where α denotes the input symmetric mode and β refers to the input antisymmetric mode:

$$|\alpha, 0\rangle = \hat{D}_1(\alpha)\,|0, 0\rangle \tag{2.68}$$

The interesting results arising from this formulation is the expectation value turns out to be null,

$$\langle \hat{\mathbf{P}} \rangle = \langle \alpha, 0|\, \hat{\mathbf{P}}\, |\alpha, 0\rangle = 0 \tag{2.69}$$

However, the variance of the momentum transfer is non-zero,

$$\begin{aligned} \Delta\mathbf{P}^2 &= \langle \hat{\mathbf{P}}^2 \rangle - \langle \hat{\mathbf{P}} \rangle^2 \\ &= \left(\frac{2\hbar\omega}{c}\right)^2 \langle \alpha, 0|\, \hat{a}_1^\dagger \hat{a}_2 \hat{a}_1 \hat{a}_2^\dagger + \hat{a}_2^\dagger \hat{a}_1 \hat{a}_2 \hat{a}_1^\dagger - \hat{a}_2^\dagger \hat{a}_1 \hat{a}_1 \hat{a}_2^\dagger - \hat{a}_1^\dagger \hat{a}_2 \hat{a}_2 \hat{a}_1^\dagger\, |\alpha, 0\rangle \\ &= \left(\frac{2\hbar\omega}{c}\right)^2 |\alpha|^2 \end{aligned} \tag{2.70}$$

For some time interval ΔT, the input laser power consisting of $\langle N \rangle = |\alpha|^2$ photons is

$$P_{in} = \frac{\hbar\omega}{\Delta T}|\alpha|^2 \tag{2.71}$$

To solve for the amplitude spectral density of the displacement, Newton's second law can be applied in the frequency domain

$$M(2\pi f)^2 \tilde{x}(f) = \tilde{F}(f) = \frac{\Delta \mathbf{P}}{\Delta T} \tag{2.72}$$

Here, the quantum radiation force spectrum, $\tilde{F}(f)$, is actually flat in frequency because the impacting photons have a randomly distributed amplitude but this gives a straightforward pathway to calculate the displacement spectrum ,

$$\tilde{x}_{RP}(f) = \sqrt{\frac{\hbar\omega}{\Delta T}P_{\text{in}}}\frac{1}{2Mc(\pi f)^2} \tag{2.73}$$

This means the noise spectral density of radiation pressure for an interferometer with a mirror of mass $M = 40$ kg, input power $P_{\text{in}} = 125$ Watts, and laser frequency $\lambda = 1064$ nm

$$\tilde{h}_{RP}(f) = 2.04 \times 10^{-20}\frac{1}{f^2}\left[\frac{\text{Strain}}{\sqrt{\text{Hz}}}\right] \tag{2.74}$$

So it is shown that the contribution of quantum radiation pressure in a simple interferometer increases with the square root of the input power.

Shot Noise

Another way that quantum fluctuations at the antisymmetric port can vary the sensitivity is by adding phase noise. Imagine holding the test masses rigidly such that the only effects on the output light is due to a phase change in the laser light in the arms. By using the same formulation for radiation pressure but propagating the fields back to the beam splitter, equations 2.65 will have extra phase that depends on the arm lengths are denoted by l_x and l_y in a simple Michelson interferometer,

$$E_{x,\text{out}} = \frac{1}{\sqrt{2}}\left[iE_0 + E_{AS,\text{in}}\right]e^{-i2kl_x} \tag{2.75a}$$

$$E_{y,\text{out}} = \frac{1}{\sqrt{2}}\left[E_0 + iE_{AS,\text{in}}\right]e^{-i2kl_y} \tag{2.75b}$$

Therefore the antisymmetric port field is described by

$$\begin{aligned} E_{AS,\text{out}} &= \frac{1}{\sqrt{2}}(E_{x,\text{out}} + iE_{y,\text{out}}) \\ &= ie^{-ikl_x - ikl_y}\big[\cos(\Delta\phi)E_0 - \sin(\Delta\phi)E_{AS,\text{in}}\big] \end{aligned} \tag{2.76}$$

where $\Delta\phi = k(l_x - l_y)$ is used for brevity. The intensity is once again found by squaring the electric field,

$$\begin{aligned} \mathbf{I}_{AS,\text{out}} &= |E_{AS,\text{out}}|^2 \\ &= \Big[\cos^2(\Delta\phi)|E_0|^2 + \sin^2(\Delta\phi)|E_{AS,\text{in}}|^2 - \sin(\Delta\phi)\cos(\Delta\phi)\big[E_0E_{AS,\text{in}}^* + E_0^*E_{AS,\text{in}}\big]\Big] \\ \Rightarrow \hat{\mathbf{I}}_{AS,\text{out}} &= \Big[\cos^2(\Delta\phi)a_1^\dagger a_1 + \sin^2(\Delta\phi)a_2^\dagger a_2 - \sin(\Delta\phi)\cos(\Delta\phi)\big[a_1^\dagger a_2 + a_2^\dagger a_1\big]\Big] \end{aligned} \tag{2.77}$$

The expectation value for the intensity using an input coherent laser with α and quantum vacuum input at the antisymmetric port is

$$\begin{aligned} \langle\hat{\mathbf{I}}\rangle &= \langle\alpha, 0|\,\hat{\mathbf{I}}_{AS,\text{out}}\,|\alpha, 0\rangle \\ &= \cos^2(\Delta\phi)|\alpha|^2 \end{aligned} \tag{2.78}$$

which matches the classical description of a Michelson output described in section 2.1.1. Following the same methods to calculate the radiation pressure, photon number variance is

$$\begin{aligned} \Delta\mathbf{I} &= \sqrt{\langle\hat{\mathbf{I}}^2\rangle - \langle\hat{\mathbf{I}}\rangle^2)} \\ &= |\alpha|\big[\cos^2(\Delta\phi)\big] \end{aligned} \tag{2.79}$$

In order to cast the variance into an expected phase noise, consider the derivative of the intensity with respect to the phase and plugging in the input power,

$$\frac{\partial I}{\partial\phi} = -2|\alpha|^2\cos(\Delta\phi)\sin(\Delta\phi) \tag{2.80}$$

$$\delta\phi = \sqrt{\frac{\hbar\omega}{P_{\text{in}}}}\cot(\Delta\phi) \tag{2.81}$$

Here $\delta\phi$ is the microscopic change in phase due to shot noise, whereas $\Delta\phi$ is the DC offset in the arm lengths to begin with. So in general, the shot noise contribution is

dependent on the amount of light present at the anti-symmetric port and this will vary depending on what type of signal readout scheme is implemented. To calculate the shot noise sensitivity, the phase shift in shot noise can be scaled by a factor of $\frac{\lambda}{2\pi}\frac{1}{L}$ where λ is the laser wavelength and L is the DC length of the Michelson arms,

$$\tilde{h}_{SN}(f) = 8.2 \times 10^{-22} \left[\frac{\text{Strain}}{\sqrt{\text{Hz}}}\right] \tag{2.82}$$

Unsurprisingly, the shot noise is proportional to $1/\sqrt{P_{\text{in}}}$ and the initial phase difference between the interferometer arms. There are a few subtleties associated with measuring shot noise, this model assumes that the interferometer is a simple Michelson and the readout is a single photodetector located at the antisymmetric port. As shown in section 2.1.5, there is freedom to choose the readout scheme of the interferometer (heterodyne or homodyne) which will also affect the overall quantum sensitivity and introducing Fabry-Perot cavities will shape the shot noise for frequencies above the differential cavity pole in equations 2.48 and 2.58.

Seismic Noise

The main contributions to seismic noise are primarily caused by either natural occurrences (tectonic plates, wind driven microcosms, oceanic storms etc) or man-made disturbances (heavy automotive traffic, industrial machinery, etc) which contribute to the background hum of motion. Table 1 shows the large In general, this will be the low frequency barrier for all terrestrial gravitational-wave detectors. One of the biggest upgrades from eLIGO to aLIGO was the increase in complexity for seismic isolation and suspensions. Using multiple stages of actively controlled platforms [65] [66] [67][4], the noise contribution can be attenuated for frequencies larger than 1Hz; in addition, the use of quadruple pendulums to hang the main arm cavity optics further reduces the motion above the pendulum's resonance frequency[32][10]. This is a tremendous upgrade from the mostly passive isolation methods used in initial LIGO. An interesting point to note is that the estimate of noise contributions from seismic activities to the strain sensitivity is negligible for frequencies above 10 Hz, but absolutely vital for lock acquisition and resonator stability [92] [46].

Frequency Band	**Causes**
0.03 - 0.10 Hz	Wind and EQs
0.10 - 0.30 Hz	Wave driven micro-seismic motion
3.00 - 10.0 Hz	Anthropogenic and trucks

Table 1 : **Frequency bands of common seismic noise at LHO.**

Thermal Noise

Brownian motion [37] is the random movement of particles suspended in a fluid. The LIGO test masses that make up the 4 kilometer long Fabry-Perot cavities are large macroscopic objects but their constituent atoms can be excited by the ambient temperature which leads to random motion. Those atoms are interconnected which allow for the propagation of an infinite number of elastic wave modes that contain random relative phases and the linear superposition of the modes create distortions that result in thermal noise.

A good way to start analyzing thermal noise is to consider a simple harmonic oscillator with mass m that is in a thermal bath with a damping force, $F = -b\dot{x}(t)$:

$$\ddot{x}(t) + \gamma\dot{x}(t) + \omega_0^2 x(t) = F/m \tag{2.83}$$

where $\gamma = b/m$ and the force can be described by white noise. In this case, F represents work being done on the system by the external world, whereas the damping factor is the release of the system's energy to the outside world. By taking the Fourier transform, the equation of motion becomes

$$\tilde{x}(f) = \frac{\tilde{F}(f)}{m}\,\frac{1}{\omega^2 + i\gamma\omega + \omega_0^2} \tag{2.84}$$

This implies that the spectral density for viscous damping is

$$S_{\text{vis}} = \frac{S_F}{m^2}\,\frac{1}{(\omega^2 - \omega_0^2)^2 + (\gamma\omega)^2} \tag{2.85}$$

Because the noise is due to a thermal bath, the integrated power over all frequencies must satisfy this equation

$$\frac{1}{2}\int_{-\infty}^{\infty} S_{\text{vis}}(\omega)\frac{\mathrm{d}\omega}{2\pi} = \frac{k_B T}{m\omega_0^2} \tag{2.86}$$

where k_B is the familiar Boltzmann's constant and T is the ambient temperature. Solving the integral and plugging the result for S_F back into the equation 2.85 gives the power spectrum for viscous damping,

$$S_{\text{vis}} = \frac{4k_BT\gamma}{m}\frac{1}{(\omega^2-\omega_0^2)^2+(\gamma\omega)^2} \tag{2.87}$$

This equation shows that for three different frequency regimes, the response can vary wildly,

$$\omega << \omega_0 \rightarrow S_{\text{vis}} = \frac{4k_BT}{mQ\omega_0^3} \tag{2.88a}$$

$$\omega \approx \omega_0 \rightarrow S_{\text{vis}} = \frac{4k_BT}{m\omega_0^3}Q \tag{2.88b}$$

$$\omega >> \omega_0 \rightarrow S_{\text{vis}} = \frac{4k_BT}{mQ}\frac{\omega_0}{\omega^4} \tag{2.88c}$$

where $Q = \omega_0/\gamma$ is commonly known as the quality factor of a resonator. Qualitatively, this is directly proportional to the resonance height and its thinness. Figure 16 shows the resultant frequency dependent amplitude spectral density for a few different quality factors, for higher Q systems the amount of noise contribution from thermal noise is reduced at frequencies above the resonance. Another commonly used definition of the quality factor is the amount of energy loss per cycle, if the Q of a system is high, then the amount of energy loss per oscillation is very small and will take a longer time returning to equilibrium. A good description of the quality factor and its application to gravitational wave detectors can be found in section 7.5 of [77].

As system's mode number increases, the previous analysis becomes very difficult to solve analytically. However, the connection between a damped harmonic oscillator's energy loss and power spectrum can be described generically using the Fluctuation Dissipation Theorem,

$$S_x(f) = \frac{k_BT}{\pi^2 f^2}|\,\mathbb{R}\text{e}(Y(f))| \tag{2.89}$$

where $Y(f)$ is the complex mechanical admittance (inverse of the impedance) of a system. The physical interpretation of equation 2.89 can be viewed as a tunnel of energy between a system of interest and the outside world. If there is an ability to couple energy from one system to another via some process, then the reverse must be true as well. This subtle but powerful statement can be applied generally. For

example, a resistor which is able to dissipate thermal energy when current is flowing through it will convert random external temperature fluctuations into stray currents that results in *Johnson Noise*. Another principle which the FD theorem relies upon is that when the system is in thermal equilibrium, its response to fluctuations will be the same as applying a small force randomly.

Using this method, the mechanical admittance of a system is defined as $Y(f) = \dot{x}(f)/F(f)$ which can be written down directly for a damped harmonic oscillator using equation 2.84,

$$\begin{aligned} \frac{\dot{x}(f)}{F} &= \frac{i\omega}{m}\frac{1}{\omega_0^2 - \omega^2 + i\gamma\omega} \\ &= \frac{i\omega}{m}\frac{(\omega_0^2 - \omega^2 - i\gamma\omega)}{(\omega_0^2 - \omega^2)^2 + (\gamma\omega)^2} \end{aligned} \tag{2.90}$$

and by plugging this into the fluctuation dissipation theorem, the power spectral density matches equation 2.87 for the viscous damping. To extend the usage further, consider the thermal noise from a solid which has some thermoelastic dissipation from an internal mode given by $F_{diss} = -k(1+\phi_L)x(t)$ where the phase term comes from the lag between applied force and the system's response to said force. By solving Newton's second law with this new damping term, the displacement spectrum becomes

$$\tilde{x}(f) = \frac{\tilde{F}}{m}\,\frac{1}{(1 + i\phi_L)\omega_0^2 - \omega^2} \tag{2.91}$$

Unlike the previous example of viscous damping, the integral for thermoelastic dissipation only holds for some frequency regime but implementing the fluctuation dissipation theorem leads directly to the noise power spectrum,

$$S_{\mathrm{TN}}(f) = \frac{4k_B T\omega_0^2\phi_L}{m\omega}\frac{1}{(\omega^2 - \omega_0^2)^2 + (\omega_0\phi_L)^2} \tag{2.92}$$

The frequency response will also be different compared to viscoelastic dissipation,

$$\omega << \omega_0 \rightarrow S_{vis} = \frac{4k_B T}{mQ\omega\omega_0^2} \tag{2.93a}$$

$$\omega \approx \omega_0 \rightarrow S_{vis} = \frac{4k_B T}{m\omega_0^3}Q \tag{2.93b}$$

$$\omega >> \omega_0 \rightarrow S_{vis} = \frac{4k_B T}{mQ}\frac{\omega_0^2}{\omega^5} \tag{2.93c}$$

The structural damping formalism can also be applied to the suspension fibers which hold the 40 kilogram test masses [50], [77] which yield a noise spectral density that contains resonances at a variety of frequencies. In Advanced LIGO, the violin modes and their harmonics could get rung up from earthquakes and saturate the output mode cleaner's DC photodiodes so they must be actively damped in order to obtain nominal low noise.

The largest contribution to the total thermal noise for current interferometers do not stem from viscous damping [79], thermoelastic damping of the substrate [77], or internal friction of the suspension fibers. The most dominant type of thermal noise is from the mechanical loss of the dielectric coatings [52] [40] which cause phase noise at the high reflectivity surface of the mirrors.

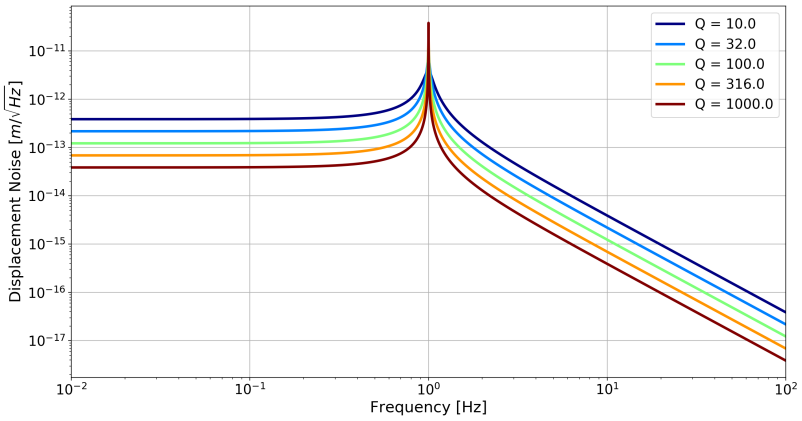

Figure 16 : **Displacement spectrum for thermal noise.** By varying the resonance width of a system, the thermal noise at frequencies above the resonant peak will be decreased for higher Q's.

Newtonian Noise

Described in the previous sections are noise sources which can be reduced using increasingly complicated techniques such as increased isolation stages for seismic or using squeezed states of light for quantum noise. However, for Newtonian noise caused by fluctuating gravitational fields from the wave motion of the ground cannot easily be reduced but possibly be measured and fed-forward or subtracted off-line [33][78][56].

2.3 Mode Matching with Squeezed States of Light

In Section 2.2, the quantum limited sensitivity for a Michelson interferometer was shown to be composed of shot noise and radiation pressure. Although quantum fluctuations are a fundamental noise source, their effects can be modified by manipulating the vacuum state with correlated photons and injecting these states of light into the antisymmetric port of the interferometer. Within the LIGO community, this procedure of modifying quantum vacuum is called squeezing. The production of squeezed states with nonlinear devices is a well understood subject and was successfully tested in the sixth LIGO science run [29][30]. An extension of the formalism described in Section 2.2 was developed by Caves-Schumaker [23] which describes two-photon quantum optics and squeezing, but it is outside of the scope in terms of mode matching.

However, it useful to understand the quantum noise in a way that scales the interferometer sensitivity in terms of the *Standard Quantum Limit* (SQL). The radiation pressure and shot noise add in quadrature to form the quantum noise and both are affected the input power but inversely from each other as shown in 2.2. The SQL refers to the input power minimizes the total quantum noise and is the minimum achievable noise without squeezing. The radiation-pressure back-action coupling constant, κ, is given by [60]

$$\kappa = \frac{4P_0\omega_0}{mc^2f^2} \tag{2.94}$$

where P_0 is the input power on the beamsplitter, ω_0 is the laser angular frequency, m is the optic mass, and f is the Fourier domain frequency. The SQL for a simple Michelson is given by [60],

$$S_{SQL} = \frac{4\hbar}{mL^2f^2} \tag{2.95}$$

With these two equations above, the total single-sided power spectral density for a simple Michelson is

$$S_{SM} = \frac{S_{SQL}}{2}\left(\frac{1}{\kappa} + \kappa\right) \tag{2.96}$$

Here the first term represents the shot noise while the second term is the radiation pressure contribution. Extending the Michelson quantum noise to the full Fabry Perot power recycled Michelson interferometer is essentially the same steps as Section 2.1.3, which showed that the gravitational wave signal became frequency dependent with

respect to the cavity pole of the arms. In addition, adding a power recycling mirror was analogous to increasing the input power by a PRC gain factor. The coupling constant for this configuration is

$$\Upsilon = 2I_0 \frac{4\omega_0}{mL^2} \frac{1}{f^2(\gamma^2 + f^2)} \tag{2.97}$$

where $\gamma = \frac{Tc}{2L}$ represents the cavity's full width half maximum and T is the input test mass transmissivity.

Modifying the field entering the antisymmetric port by replacing the quantum vacuum with a squeezed state has interesting effects on the strain sensitivity and reduces the noise floor below the standard quantum limit. The power spectral density for a power recycled Fabry Perot interferometer with injected squeezing is described by [60],

$$\begin{aligned} S_{\mathrm{PR}} &= \frac{S_{SQL}}{2}\left(\frac{1}{\Upsilon} + \Upsilon\right)[\cosh 2R - \cos(2(\phi_s + \theta_s))\sinh 2R] \\ &= \frac{S_{SQL}}{2}\left(\frac{1}{\Upsilon} + \Upsilon\right)e^{-2R} \qquad \text{for } \theta_s = -\phi_s x \end{aligned} \tag{2.98}$$

where R is the squeeze factor, θ_s is the squeeze angle, and $\phi_s = \cot^{-1}(\Upsilon)$. The squeeze angle can change the regime of strain which is affected, for example, when injecting for optimal shot noise reduction one would choose $\theta_s = \pi/2$. However, when trying to reduce the radiation pressure noise, then choosing $\theta_s = 0$ is optimal. For the second line in the equation above, to achieve broadband squeezing, the squeeze angle must be rotated as a function of frequency. Fortunately, this can be achieved by reflecting the squeezer beam off a filter cavity before injecting into the interferometer [70] [41]. Various configurations for squeezing is shown in Figure 17b. The addition of optical losses play a large role in the interferometer sensitivity for a number of reasons:

1. The arm cavities and output optical train have associated losses which couple vacuum fluctuations and contribute shot noise. Generally, the former will have associated frequency dependence and be proportional to the round trip loss in the arm cavities.

2. A back-action coupling will also increase as a function of the round trip loss and contribute to the radiation pressure.

3. Vacuum fluctuations originating from the antisymmetric port of the interferometer will also add losses.

4. And finally, the squeezing degradation will be affected by the losses injected into the interferometer and mode matching.

An equation found in Kimble [60] can describe the first three points by defining the loss coefficient as $\mathcal{L} = 2\mathcal{L}_{\mathrm{ARM}}/T$ where $\mathcal{L}_{\mathrm{ARM}}$ is the round trip arm loss so the fractional power loss will be

$$\varepsilon = \frac{2\mathcal{L}}{(1 + (f/\Upsilon)^2)} \tag{2.99}$$

which leads to a more complete equation for the quantum limited sensitivity with losses and optimal squeezing

$$S_{\mathrm{PR}_L} = \frac{S_{SQL}}{2}\left[\frac{\varepsilon + \varepsilon_{OT}}{\Upsilon} + \frac{\mathcal{L}}{2}\Upsilon + \left(1 - \frac{1}{2}\varepsilon\right)\left(\frac{1}{\Upsilon} + \Upsilon\right)e^{-2R}\right] \tag{2.100}$$

Here, ε_{OT} represents losses from the interferometer optical readout train due to mode mismatch between the IFO and the output mode cleaner. The fourth point for optical losses is handled differently because it has to deal with mode mismatched coupling between the squeezed light and the interferometer which reduces the effective squeezing level. It is shown in Chua's thesis [27] that quantum vacuum combines with the squeezed state through losses and forces the optical field variance back to the vacuum state, thereby degrading the squeezing benefits. By coupling the fundamental field that is squeezed to a combination of higher order modes, this will also act as a direct loss. Figure 1 of Dwyer et al [34] shows that squeezing efficacy depends strongly on total losses and the squeeze quadrature fluctuations. The details of mode mismatch will come in the next chapters but it is clear that reducing losses will play an important role for the operation of both a squeezed or non-squeezed interferometer.

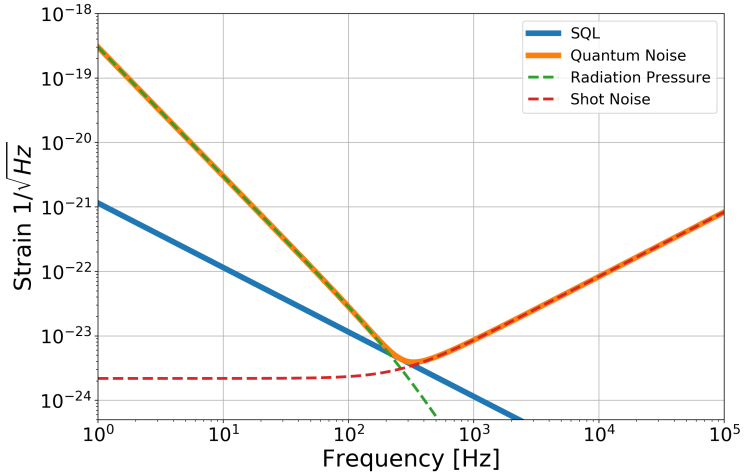

(a) Power recycled Fabry Perot Michelson quantum noise

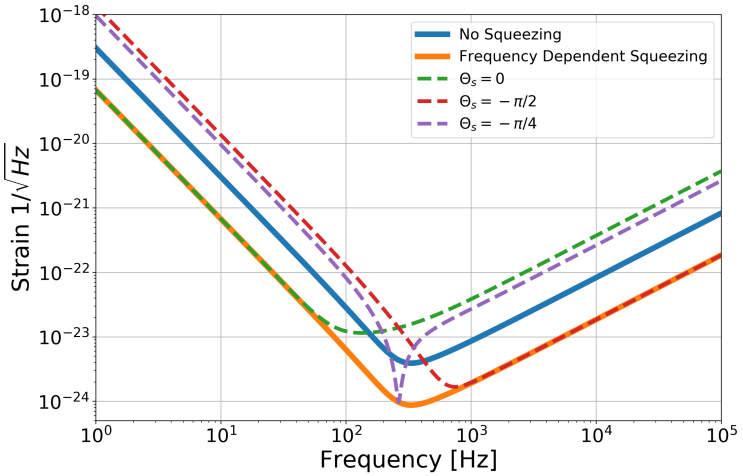

(b) Power recycled Fabry Perot Michelson quantum noise with various squeezing angles

Chapter 3

The Fundamentals of Mode-Matching

When dealing with the length sensing degrees of freedoms in Chapter 2, the plane wave approximation is sufficient for describing the resonator dynamics. However, when trying to understand the misalignment and mode mismatch signals, it is necessary to incorporate Gaussian beams and their associated higher order modes. This formalism plays a pivotal role in the LIGO detectors because the gravitational wave is sensed using the fundamental eigenmode of the arm cavities and any coupling to higher order modes results in a loss of signal at the antisymmetric port. Equally as important, the reduction of angular motion to remain locked relies on robust sensing of the cavity misalignment from external disturbances [46] and torque-to-angle coupling [83]. Mode matching is a second order effect but it will be shown in Chapter 6 that mismatches play an important role in the practical operation of a large scale interferometer.

3.1 Gaussian Beam Optics

To show that a Gaussian beam is a valid electromagnetic wave, consider the famous Maxwell's equations:

$$\begin{aligned} \nabla \times \mathbf{E} &= -\frac{\partial \mathbf{B}}{\partial t} \\ \nabla \cdot \mathbf{B} &= 0 \\ \nabla \times \mathbf{B} &= \mu\ \mathbf{J} + \frac{1}{c^2}\frac{\partial \mathbf{E}}{\partial t} \\ \nabla \cdot \mathbf{E} &= \frac{\rho}{\epsilon} \end{aligned} \tag{3.101}$$

Concentrating on the electric field in vacuum, we arrive at the Helmholtz Equation

$$(\nabla^2 + k^2)\mathbf{U}(\mathbf{r}, t) = 0 \tag{3.102}$$

where $k = \frac{2\pi\nu}{c}$ is the wave number and $\mathbf{U}(\mathbf{r}, t)$ is the complex amplitude which can describe either the electric or magnetic fields. There are a variety of solutions to equation 3.102 which include the plane and spherical waves [76]. These two types of solutions are the extremes when considering the angle and spatial distribution as a function of propagation. The plane wave which has been used in chapter 1 is a beam whose rays have no variance in the spatial direction as it propagates through space, whereas the spherical wave starts at a point and spreads as a function of distance from the origin. Somewhere in between these two extrema is the paraxial wave which is a wave pattern that consists of rays at small angles relative to the direction of propagation. It is possible to express the paraxial solution to equation 3.102 as a plane wave with a modulated complex envelope $\mathbf{A}(r)$,

$$\mathbf{U}(\mathbf{r}) = \mathbf{A}(\mathbf{r})e^{-ikz} \tag{3.103}$$

However, in order for the paraxial wave to exist, $\mathbf{U}(r)$ must satisfy the Helmholtz equation. Alternatively, the $\mathbf{A}(r)$ must satisfy a separate differential equation known as the paraxial Helmholtz Equation which can be derived explicitly by imposing constraints that force the envelope to vary slowly with respect to the z-axis within

the distance of one wavelength $\lambda = 2\pi/k$:

$$\left|\frac{\partial^2 \mathbf{A}}{\partial z^2}\right| \ll \left|k\frac{\partial \mathbf{A}}{\partial z}\right| \tag{3.104a}$$

$$\left|\frac{\partial^2 \mathbf{A}}{\partial z^2}\right| \ll \left|k\frac{\partial^2 \mathbf{A}}{\partial x^2}\right| \tag{3.104b}$$

$$\left|\frac{\partial^2 \mathbf{A}}{\partial z^2}\right| \ll \left|k\frac{\partial^2 \mathbf{A}}{\partial y^2}\right| \tag{3.104c}$$

The partial differential equation which arises is called the Paraxial Helmholtz Equation:

$$\nabla_T^2 A(r) - i2k\frac{\partial A(r)}{\partial z} = 0 \tag{3.105}$$

where $\nabla_T^2 = \frac{\partial^2}{\partial x^2} + \frac{\partial^2}{\partial y^2}$ is the transverse Laplacian. A simple solution for equation 3.105 is the complex paraboloidal wave,

$$A(\mathbf{r}) = \frac{A_0}{q(z)} e^{\frac{-ikr^2}{2q(z)}}, \quad q(z) = z + iz_0 \tag{3.106}$$

The parameter z_0 is referred to as the Rayleigh range and is directly proportional to the waist size squared. In order to separate the amplitude and phase portions of the wave, it is useful to rewrite $q(z)$ as

$$\frac{1}{q(z)} = \frac{1}{R(z)} - i\frac{\lambda}{\pi W^2(z)} \tag{3.107}$$

Plugging equation 3.107 into 3.106 leads directly to the complex amplitude for a Gaussian Beam

$$U(r,z) = A_0 \frac{W_0}{W(z)} e^{-\frac{r^2}{W^2(z)}} e^{-ikz - ik\frac{r^2}{2R(z)} + i\zeta(z)} \tag{3.108}$$

where

$$W(z) = W_0\sqrt{1 + \left(\frac{z}{z_0}\right)^2} \tag{3.109a}$$

$$R(z) = z\left[1 + \left(\frac{z}{z_0}\right)^2\right] \tag{3.109b}$$

$$\zeta(z) = \tan^{-1}\left(\frac{z_0}{z}\right) \tag{3.109c}$$

$$W_0 = \sqrt{\frac{\lambda z_0}{\pi}} \tag{3.109d}$$

The Gaussian beams are named as such because of the intensity distribution,

$$I(r,z) = |U(r,z)|^2 = I_0 \left[\frac{w_0}{w(z)}\right]^2 \exp\left[\frac{-2r^2}{w^2(z)}\right] \tag{3.110}$$

where $I_0 = |A_0|^2$ and has a peak at $r = 0$ and $z = 0$. The width increases as the beam propagates along the $\hat{z}$ axis away from the waist position and the intensity maximum on the beam axis decreases (see Figure 20),

$$I(0,z) = \frac{I_0}{1 + (z/z_0)^2} \tag{3.111}$$

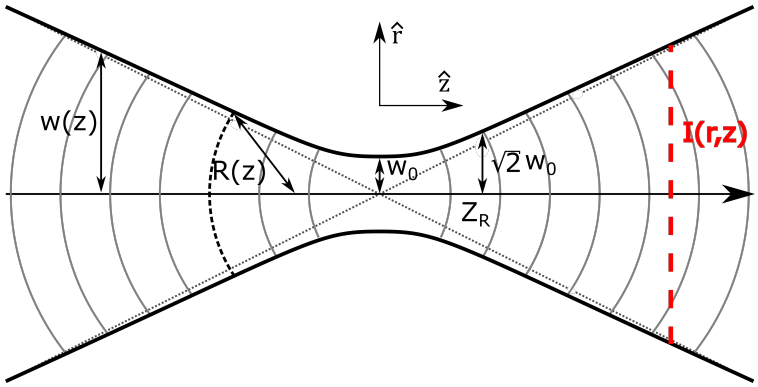

Figure 18 : **A depiction of the Gaussian beam properties with respect to cylindrical coordinates.** Because the beam is axially symmetric, the two coordinates are denoted by $\hat{r}$ for the radial and $\hat{z}$ for the axis of propagation with the origin located at the center. The thick dark lines represent the beam size, $w(z)$, which is minimal at the waist, $w(z) = w_0$ when $z = 0$ and asymptotic towards $\lambda/\pi w_0$ when $z \approx$ inf as shown by the dotted gray lines. The red dashed line represents the intensity cross section of the beam which changes to a wider and flatter profile as a function of distance from the waist.

Hermite-Gauss Modes

The fundamental Gaussian beam is not the only solution which can be used to solve equation 3.105. In fact, there exists a complete set of solutions that can solve the paraxial Helmholtz Equation in rectangular coordinates, which are referred to as

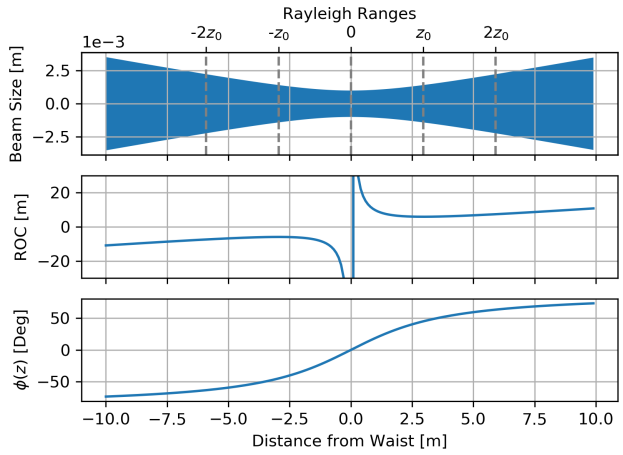

Figure 19 : **Beam size, radius of curvature, and Gouy phase as a function of distance propagation from the waist.** The vertical dashed gray lines represent the integer number of Rayleigh ranges. At the point $z = z_0$, the beam size is $\sqrt{2}$ of the waist size and the radius of curvature is minimal. At this point, the Gouy phase propagation is lagging the plane wave by $\pi/4$ and the beam intensity is half of that at the waist.

the Hermite Gauss modes

$$U_{mn}(x,y,z) = A_{mn}\left[\frac{W_0}{W(z)}\right]\mathbb{G}_m\left(\frac{\sqrt{2}x}{W(z)}\right)\mathbb{G}_n\left(\frac{\sqrt{2}y}{W(z)}\right) \times \exp\left\{-ikz - \frac{ik(x^2+y^2)}{2R(z)} + i(m+n+1)\zeta(z)\right\} \tag{3.112}$$

where,

$$\mathbb{G}(u) = \mathbb{H}(u)\exp(-u^2/2) \tag{3.113}$$

and $\mathbb{H}(u)$ are the well known Hermite polynomials. It is important to mention that the Gouy phase of the complex amplitude is different than the fundamental Gaussian beam by a factor of $(m+n+1)$ and that the intensity distribution of these higher order modes are much different. Both of these facts will become extremely important in the following wavefront sensing discussion.

Laguerre Modes

Another complete set of alternative solutions to equation 3.105 exists which are called the Laguerre-Gauss modes

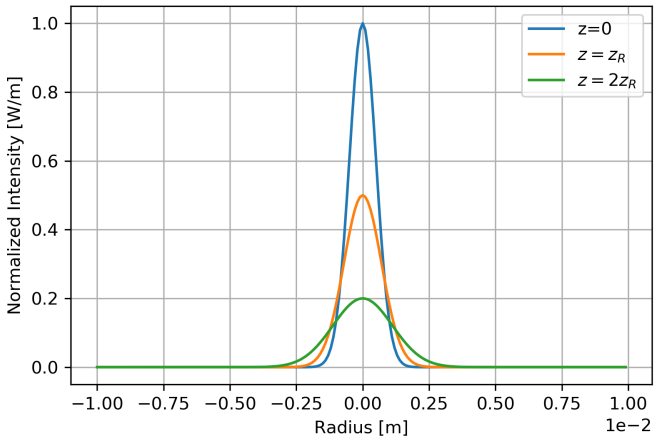

Figure 20 : Intensity

$$V_{\mu\nu}(\rho,\theta,z) = A_{\mu\nu}\left[\frac{W_0}{W(z)}\right]\mathbb{L}^{\mu}_{\nu}\left(\frac{\sqrt{2}x}{W(z)}\right) \times \exp\left\{-ikz - \frac{ik\rho^2}{2R(z)} + i(\mu+2\nu+1)\zeta(z)\right\} \tag{3.114}$$

where $\mathbb{L}^{\mu}_{\nu}\left(\frac{\sqrt{2}x}{W(z)}\right)$ is the Laguerre polynomial function. Both equations 3.112 and 3.114 are able to fully describe any complex electromagnetic amplitude; and because they both form complete sets, there is a rotation which can map from one basis to the other [7] [72]

$$U^{LG}_{\mu\nu}(x,y,z) = \sum_{k}^{N} i^k b(n,m,k) U^{HG}_{N-k,k}(x,y,z) \tag{3.115}$$

where

$$b(n,m,k) = \sqrt{\left(\frac{(N-k)!k!}{2^N n!m!}\right)}\frac{1}{k!}\frac{\mathrm{d}^k}{\mathrm{d}t^k}[(1-t)^m(1+t)^m]|_{t=0} \tag{3.116}$$

3.1.1 Misalignment and Higher Order Modes

Morrison and Anderson [5] [68] derived a simplistic way of how small misalignments and mode mismatch in cavities can couple the fundamental Gaussian beam into various higher order modes. This is done by taking a linear cavity and using its perfectly matched Gaussian beam as a reference, and then varying the input electric field with

small perturbations and expanding in terms of the higher order modes. So long as the mismatches are small, it is possible to consider only the first few terms of the expansion which have gained most of their power from the fundamental mode. Between various texts, the terms misalignment and mode mismatch are used interchangeably, which is not incorrect but creates some confusion. This thesis will try to distinguish the two effects because the actuators and sensors used for correction can be quite different.

Consider the first three Hermite-Gauss modes of equation 3.112 in one dimension and normalized to set the total optical power to unity:

$$\begin{aligned} U_0(r) &= \left(\frac{2}{\pi w^2(z)}\right)^{1/4} e^{-r^2/w^2(z)} \\ U_1(r) &= \left(\frac{2}{\pi w^2(z)}\right)^{1/4} \frac{2r}{w(z)} \quad e^{-r^2/w^2(z)} \\ U_2(r) &= \left(\frac{2}{\pi w^2(z)}\right)^{1/4} \frac{1}{\sqrt{2}}\left(\frac{4r^2}{w^2(z)} - 1\right) e^{-r^2/w^2(z)} \end{aligned} \quad , \tag{3.117}$$

Beam Axis Tilted

If the input beam entering an optical cavity is tilted by an angle α with respect to the nominal cavity axis, the wave front of the input beam will have an extra phase propagation relative to the cavity that is approximately proportional to $e^{ik\alpha r}$. By implementing the small angle approximation, which is valid if the misalignment is much smaller than the divergence angle of the fundamental mode $k\alpha r << 1$, the resultant input beam is

$$\Psi \approx U_0(r)e^{ik\alpha r} \approx U_0(r)(1 + ik\alpha r) = U_0(r) + \frac{ik\alpha w(z)}{\sqrt{2\pi}} U_1(r) \tag{3.118}$$

Here, the factor associated with the first higher order mode is complex, indicating there is a 90 degree phase difference between the fundamental and off-axis mode.

Beam Axis Displaced

If the input beam is displaced in the transverse direction by a quantity Δr, the resultant waveform will be

$$
\begin{aligned}
\Psi &= U_0(r+\Delta r) \\
&= \left(\frac{2}{\pi w^2(z)}\right)^{1/4} e^{-(r+\Delta r)^2/w^2(z)} \\
&= \left(\frac{2}{\pi w^2(z)}\right)^{1/4} e^{-(r^2+2r\Delta r+\Delta r^2)/w^2(z)} \\
&\approx \left(\frac{2}{\pi w^2(z)}\right)^{1/4} e^{-r^2/w^2(z)} e^{-2r\Delta r/w^2(z)} \\
&\approx \left(\frac{2}{\pi w^2(z)}\right)^{1/4} e^{-r^2/w^2(z)} \left(1-\frac{2r\Delta r}{w^2(z)}\right) \\
&= \left(U_0(r) - \sqrt{\frac{2}{\pi}}\frac{\Delta r}{w(z)} U_1(r)\right)
\end{aligned}
\tag{3.119}
$$

Similar to a tilted input beam axis, the displaced beam axis couples power to the first higher order mode, however, the latter does not have a 90 degree phase difference. This point is extremely important when trying to discern between the two effects. Although comparing the two cases in Figure 21b, one can already see the difference between wavefronts in the near field, $z << z_R$, and the far field, $z >> z_R$. In the near field, there is no wavefront phase difference between the original beam and the displaced beam, but there is one for a tilted beam. Conversely in the far field, there is no phase difference due to a tilted beam, but there is one from a displaced beam. In order to implement a closed loop feedback system, the wavefront sensors discussed in Section 3.2 will use this precise logic to extract an error signal.

3.1.2 Mode Mismatch and Higher Order Modes

Using the same formalism as above, determining the second order mode coupling from mode mismatch is repeated.

Waist Size Shifted

By considering the effect of evaluating the fundamental mode at the waist position, $z = 0$, but changing the waist size by a small amount ϵ, it is possible to see coupling

into higher order modes by expanding to first order.

$$\begin{aligned}
\Psi &= U_0\big(r, w(z) = w_0/(1+\epsilon)\big) \\
&= \left(\frac{2}{\pi w_0^2}\right)^{1/4} \sqrt{1+\epsilon} \quad e^{-r^2(1+\epsilon)^2/w_0^2} \\
&\approx \left(\frac{2}{\pi w_0^2}\right)^{1/4} (1+\epsilon/2) \quad e^{-r^2/w_0^2} \quad e^{-2r^2\epsilon/w_0^2} \\
&\approx \left(\frac{2}{\pi w_0^2}\right)^{1/4} (1+\epsilon/2) \quad e^{-r^2/w_0^2} \quad (1-2r^2\epsilon/w_0^2) \\
&\approx \left(\frac{2}{\pi w_0^2}\right)^{1/4} \left(1+2\epsilon\left(\frac{1}{4}-\frac{r^2}{w_0^2}\right)\right) \quad e^{-r^2/w_0^2} \\
&= U_0(r) \; - \; \frac{\epsilon}{\sqrt{2}}\, U_2(r)
\end{aligned} \tag{3.120}$$

By changing the waist size by a small amount, the mismatch will couple the fundamental mode to the in-phase second order Hermite Gauss mode.

Waist Position Shifted

To repeat the process from above with a waist position shift, it is useful to start with a more general equation that includes the phase that is gained from including the radius of curvature,

$$\Psi = \left(\frac{2}{\pi w^2(z)}\right)^{1/4} \quad e^{-r^2/w^2(z)} \quad e^{-ikr^2/2R(z)} \tag{3.121}$$

where $R(z)$ is from equation 3.109b. It is also useful to approximate the shift in waist position along the longitudinal axis is small compared to the Rayleigh range of the beam, $\Delta z << z_0$, which leaves the waist size approximately the same and the radius of curvature inversely proportional to the shift.

$$w^2(\Delta z) = w_0^2\left[1+\left(\frac{\Delta z}{z_0}\right)^2\right] \approx w_0^2 \tag{3.122a}$$

$$R(\Delta z) = \Delta z\left(1+\left(\frac{z_0}{\Delta z}\right)^2\right) \approx \frac{z_0^2}{\Delta z} \tag{3.122b}$$

Plugging the equations above into 3.121,

$$\begin{aligned}\Psi &\approx \left(\frac{2}{\pi w_0^2}\right)^{1/4} \quad e^{-r^2/w_0^2} \quad e^{-ikr^2\Delta z/2z_0^2} \\ &\approx \left(\frac{2}{\pi w_0^2}\right)^{1/4} \quad e^{-r^2/w_0^2} \quad \left(1-\frac{ikr^2\Delta z}{2z_0^2}\right) \\ &= U_0(r) - \left(\frac{2}{\pi w_0^2}\right)^{1/4} e^{-r^2/w_0^2} \quad \frac{ikr^2\Delta z}{2z_0^2} \\ &= U_0(r) - i\frac{\Delta z}{2kw_0^2}\Big(4U_2(r)+U_0(r)\Big)\end{aligned} \tag{3.123}$$

The equations above show that a fundamental Gaussian mode that is shifted in waist position will couple power to the second order Hermite Gauss mode. Although changes in the waist size or position couple power to the same mode, they differ by a 90 degrees in phase as denoted by the extra factor of i in the coupling coefficient. By recognizing the two effects are in different quadrature phases will allow a user to design a system to distinguish between the different types of physical couplings, this is shown in Section 3.2.

In order to be physically valid one would need to consider the full two dimensional space so that the equation would encapsulate the full transverse mode, however, the x and y components would follow the exact same derivation. On that point, it is important to note that only the mode mismatch couplings from either a varying waist position or size has higher order modes that are circularly symmetric.

3.2 Wavefront Sensing

In Chapter 2.1.1 and 2.1.5, a heterodyne detection scheme was used to sense the longitudinal degree of freedom for optical cavities. Analogously, a technique using sidebands can employ a modal decomposition of the full electric field which allows the use of wavefront sensors to extract an error signal. Hefetz et.al [53] created a formalism to describe the use of wavefront sensors by creating frequency sidebands which accumulate a different Gouy phase than the electric field at the carrier frequency when passed through the optical system. By observing the demodulated signal of the intensity, it is possible to obtain a linear signal that corresponds to a physical misalignment or mode mismatch. Fundamentally, the purpose of wavefront sensing

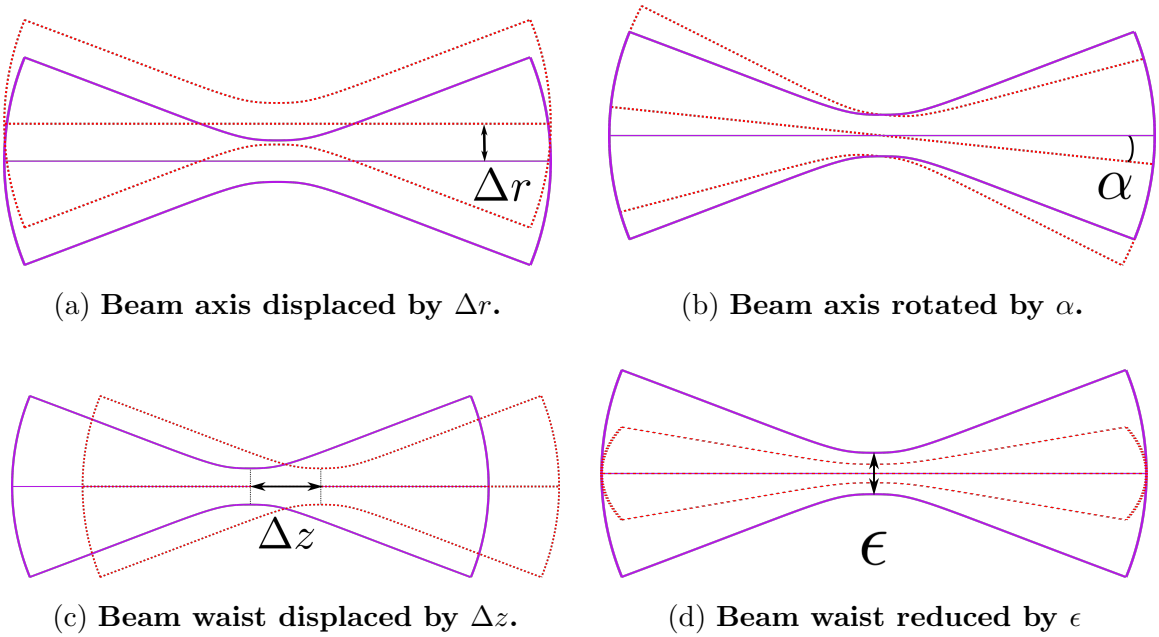

(a) **Beam axis displaced by Δr.**

(b) **Beam axis rotated by α.**

(c) **Beam waist displaced by Δz.**

(d) **Beam waist reduced by ϵ**

Figure 21 : **Misaligment and mode mismatch between two different Gaussian beams.** The purple solid curves represent the original Gaussian shape and the red dotted curves are beams which have been augmented in one degree of freedom. It is important to note that using this representation uses the eigenmode of the cavity as a starting basis, if one were to create these misalignments using the actual optics, there needs to be a linear combination of rotations or curvature changes.

is to detect the content of higher order modes due to physical disturbances of the optical cavity and by extension, it is examining the difference between the incoming beam and the cavity eigenmodes.

Consider a general equation for an electric field which is a linear combination of all higher order modes of the complex amplitude

$$E(x,y,z) = \sum_{m,n}^{\infty} a_{mn} U_{mn}(x,y,z) \tag{3.124}$$

where $U_{mn}(x,y,z)$ are the eigenmodes described in equation 3.112 (or 3.114) and a_{mn} is the complex amplitude. It is also convenient in the following analysis to use vectors when describing the composition of the electric fields.

$$|E(x,y,z)\rangle = \begin{pmatrix} E_{00} \\ E_{01} \\ E_{10} \\ E_{20} \\ E_{02} \end{pmatrix} \tag{3.125}$$

When creating a theory that involves laser beams, it is useful to define operators that are important in describing physical situations. For example, laser beams propagate through space and pick up phase according to equation 3.112 which can be represented by the spatial propagation operator,

$$\hat{P}_{mn,kl} = \delta_{mn}\delta_{kl} \quad \exp[-ik(z_2 - z_1)]\exp[i(m+n+1)\zeta(z)] \tag{3.126}$$

However, it is useful to compare how the fundamental Gaussian mode propagates compared to the higher order modes,

$$\hat{\eta}_{\mu\nu} = \begin{pmatrix} e^{i\zeta} & 0 & 0 & 0 & 0 \\ 0 & e^{2i\zeta} & 0 & 0 & 0 \\ 0 & 0 & e^{2i\zeta} & 0 & 0 \\ 0 & 0 & 0 & e^{3i\zeta} & 0 \\ 0 & 0 & 0 & 0 & e^{3i\zeta} \end{pmatrix} \tag{3.127}$$

From the above diagonal elements, it is clear that the higher order modes have an extra phase compared to the fundamental 00 mode, this effect will be extremely important on how an error signal can be derived from the optical system.

$$|E(x,y,z_2)\rangle = \hat{M}(x,y,z_1,z_2)\,|E(x,y,z_1)\rangle \tag{3.128}$$

where $\hat{M}(x,y,z_1,z_2)$ is the misalignment operator. Since we are using the paraxial approximation, the z-components of the misalignment operator are small so we can approximate $\hat{M}(x,y,z_1,z_2) \approx \hat{M}(x,y)$ and the expectation value is

$$M_{mn,kl} = \langle U_{mn}(x,y,z_1)|\, M(x,y)\,|U_{kl}(x,y,z_2)\rangle \tag{3.129}$$

where the product is an integral over the transverse space $\iint_{D(x,y)} \mathrm{d}x\mathrm{d}y$

$$\hat{\Theta}_{\mu\nu} = \begin{pmatrix} 1 & 2i\theta_x & 2i\theta_y & 0 & 0 \\ 2i\theta_x & 1 & 0 & 0 & 0 \\ 2i\theta_y & 0 & 1 & 0 & 0 \\ 0 & 0 & 0 & 1 & 0 \\ 0 & 0 & 0 & 0 & 1 \end{pmatrix} \tag{3.130}$$

$$\hat{\mathbb{D}}_{\mu\nu} = \begin{pmatrix} 1 & \alpha_x/\omega_0 & \alpha_y/\omega_0 & 0 & 0 \\ \alpha_x/\omega_0 & 1 & 0 & 0 & 0 \\ \alpha_y/\omega_0 & 0 & 1 & 0 & 0 \\ 0 & 0 & 0 & 1 & 0 \\ 0 & 0 & 0 & 0 & 1 \end{pmatrix} \tag{3.131}$$

$$\hat{\mathbb{Z}}_{\mu\nu} = \begin{pmatrix} 1 & 0 & 0 & \Delta z_x & \Delta z_y \\ 0 & 1 & 0 & 0 & 0 \\ 0 & 0 & 1 & 0 & 0 \\ \Delta z_x & 0 & 0 & 1 & 0 \\ \Delta z_y & 0 & 0 & 0 & 1 \end{pmatrix} \tag{3.132}$$

where $\Delta z_{(x,y)} = \frac{i}{\sqrt{2}} \frac{\lambda b}{2\pi\omega_0}$

$$\hat{\mathbb{Z}}_{0,\mu\nu} = \begin{pmatrix} 1 & 0 & 0 & \Delta z_{0,x} & \Delta z_{0,y} \\ 0 & 1 & 0 & 0 & 0 \\ 0 & 0 & 1 & 0 & 0 \\ \Delta z_{0,x} & 0 & 0 & 1 & 0 \\ \Delta z_{0,y} & 0 & 0 & 0 & 1 \end{pmatrix} \tag{3.133}$$

where $\Delta z_{0,(x,y)} = \frac{1}{\sqrt{2}} \frac{\omega' - \omega_0}{\omega_0}$

Gouy Phase

Understanding the relationship between Gouy phase as defined by 3.109c and how the term is used colloquially within the LIGO experimental community is not very straightforward. Gouy phase given by equation 3.109c is the phase lag between a Gaussian beam and a perfect plane wave that occurs as a function of propagation along the $\hat{z}$-axis which ranges from $\zeta(z) = \pm\pi/2$ for $z = \pm\,\text{inf}$. Physically, this could be interpreted as the difference between the laser beam behaving like a plane wave when $z \approx 0$ (or near field) and eventually evolving into a spherical wave when $z \approx \pm\,\text{inf}$ (or far field), see Figure 19. Although this phenomenon is interesting mathematically, most texts do not consider how to practically use or measure the Gouy phase. In LIGO technical notes and electronic logs, the Gouy phase of sensors or actuators is often used to describe where along the beam path the piece of equipment is located. This will indicate what degree of freedom is being observed or adjusted. For example, in ray optics [76] a laser beam has two degrees of freedom, the displacement and angle from the optical axis. If an actuator such as a piezo-electric transducer with an attached reflective mirror is placed near the origin or focus of the laser beam, then the controlled degree of freedom is only the angle. Alternatively, if the actuator is placed in the far field then the controlled degree of freedom is almost entirely displacement. So to have full control over the alignment of a laser beam, it is required to have two actuators separated by 90 degrees in Gouy phase.

This is also true of sensors at various points along the $\hat{z}$-axis to determine the exact alignment of the optical beam. In practice, it is impossible to sense the true waist of an optical system because it could be inside a Fabry-Perot cavity. So the clever

designer must insert a pick-off beam to sample the transmission or reflection of the interested optical system and use a combination of lenses to create a telescope for the sensors and infers the degrees of freedom. Then, by rotating to the two-dimensional space created by the sensors to represent the interested space spanned by the optical system's degrees of freedom; colloquially, this is known as a sensing matrix. Using this method, sensors do not have to be exactly at the near or far field because it is only required that the two sensors are separated by $\pi/2$ in Gouy phase, in fact, it is usually easier to place one sensor at $+\pi/4$ and the other at $-\pi/4$. Unfortunately, there is no transducer that directly measures the Gouy phase so in order to *determine* the Gouy phase of a particular sensor or actuator, one must model the beam propagation and fit the waist location.

Another way which Gouy phase is presented in many LIGO discussions is regarding the round trip accumulation of phase while propagating in an optical cavity. This plays an important role because the round trip Gouy phase is directly proportional to the transverse mode spacing. Recall that the free spectral range of a cavity is equal to $f_{\mathrm{FSR}} = c/2L$ which sets the frequency separation between the fundamental modes, and that the Gouy phase propagation for higher order modes is equal to $(m+n+1)\zeta(z)$ so these modes will effectively *see* a different cavity than the zeroth. Gouy phase can be calculated explicitly by using the ABCD formulation and relating the matrix elements to the round trip phase,

$$\zeta = \mathrm{sgn}B \arccos\left(\frac{A+D}{2}\right) \tag{3.134}$$

where A, B, C, and D are the matrix elements of the optical system. The Gouy phase is related to the transverse mode spacing by

$$f_{\mathrm{TMS}} = \frac{\zeta}{2\pi} f_{\mathrm{FSR}} \tag{3.135}$$

The extra Gouy phase that a higher order mode accrues as a function of z shows up as in the frequency or cavity length domain as one sweeps through a full free spectral range using an offset in the length or frequency error signal. This can be directly used to measure the higher order mode separation and becomes important if the cavity has a low finesse which means the fundamental Gaussian mode has a spread comparable

in frequency to the first order mode then it is easy to hop from one to the other (see Figure 22).

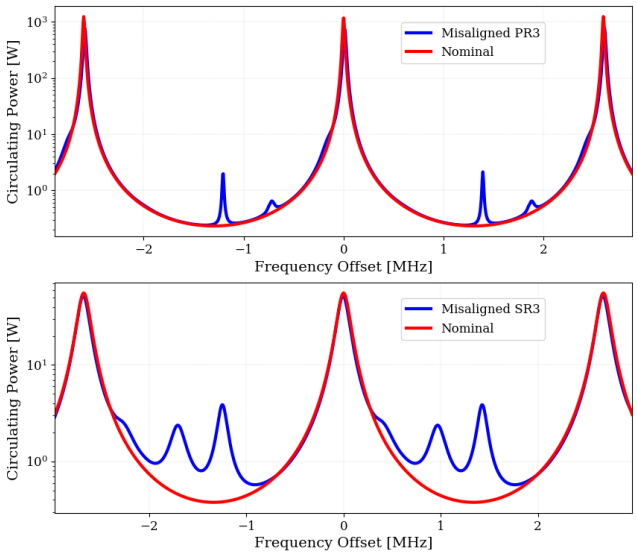

Figure 22 : **A Finesse model of a longitudinal mode scan comparing the Advanced LIGO power recycling and signal recycling cavities** The upper and lower plots represents the PRC and SRC, respectively. The main difference between these two optical cavities is obvious when comparing the three large peaks corresponding to the 00 mode resonances. The power recycling cavity has a much higher and sharper peak which indicates a larger finesse where as the signal recycling cavity is a much lower finesse has a broader and shorter peak. The red traces are with nominal alignment compared with the blue lines corresponding to misalignments of PR3 and SR3 by 1μrad. This allows higher order mode content to resonate as a function of length or frequency.

Chapter 4

Simulating Mode-Matching with FINESSE

In Chapter 2, the optical gain from differential arm motion was determined analytically with very few approximations but in actuality, LIGO has more degrees of freedom which make precise calculations very cumbersome. The complexity scales very rapidly in application to the main interferometer and mode matching is no exception so it is useful to use a full scale numerical simulation to extract as much information as possible. FINESSE [71] [11] is one of the leading full-scale interferometer simulation tools which uses the linear input-output relations of electromagnetic fields to model optical properties of the LIGO interferometer. This chapter uses FINESSE to model the quantum limited noise sensitivity with mode mismatch at key points in the interferometer and determine which actuators are needed for optimal matching into the output mode cleaner. This is extremely important in the current generation of Advanced LIGO when squeezing is implemented because of the sensitivity to losses between the optical parametric oscillator and the interferometer cavities. By using FINESSE's ability to incorporate higher order beams and RF sidebands, it is possible to quickly and accurately model mode matching.

4.1 FINESSE Simulations

The power of numerical simulations has an interesting dual advantage, firstly, optical parameters which are difficult to measure such as Gouy phase or higher order mode

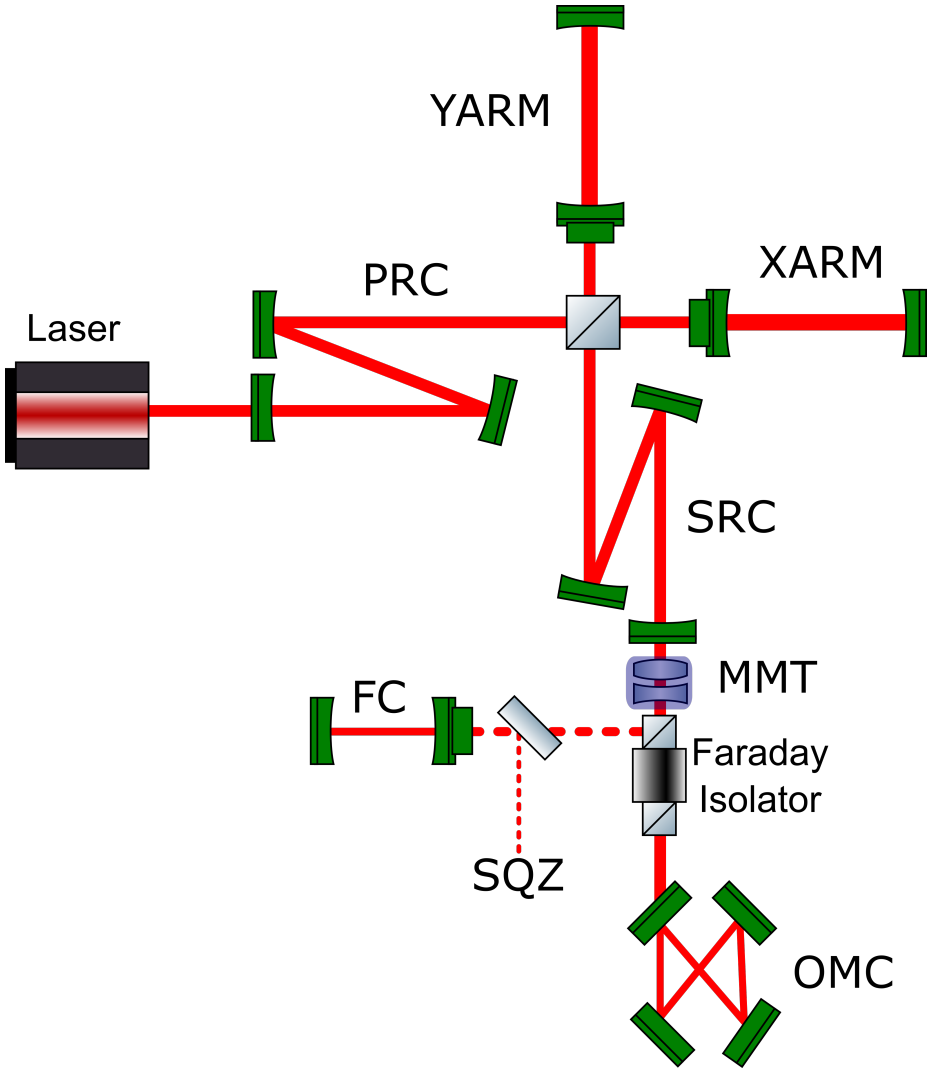

Figure 23 : **Full interferometer simulation with FINESSE.** This includes squeezed light injection, a lossless 16-meter filter cavity, and an ideal mode matching telescope (highlighted in blue) at the signal recycling output port which can be turned on/off to determine the SRC mode mismatches without additional lensing effects when changing the radius of curvatures. For brevity, the input mode cleaner is omitted in the schematic but is also a resonant cavity in the simulation where it is approximated to have small thermal effects and is at least 99.9% mode matched to the interferometer. Optical parameters are taken from the as-designed values for advanced LIGO and a few key variables are replaced with H1 specific constants.

content can be directly calculated to guide in designing future systems. Secondly, when analytical calculations become unwieldy, numerical methods accurately describe complicated optical responses in the presence of perturbations or imperfections.

An Advanced LIGO configuration file [12] which utilizes as-designed values for

$$\begin{bmatrix} 0 & r_b e^{i\phi} & it_b & 0 \\ r_b e^{i\phi} & 0 & 0 & it_b \\ it_b & 0 & 0 & r_b e^{-i\phi} \\ 0 & it_b & r_b e^{-i\phi} & 0 \end{bmatrix} \begin{bmatrix} \text{In1} \\ \text{In2} \\ \text{In3} \\ \text{In4} \end{bmatrix} = \begin{bmatrix} \text{Out1} \\ \text{Out2} \\ \text{Out3} \\ \text{Out4} \end{bmatrix}$$

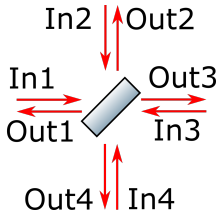

Figure 24 : **How FINESSE sees a beamsplitter.** An example of the coupling matrix for an arbitrary beamsplitter with reflectivity, r_b, and transmissivity, t_b. Another free parameter for a beamsplitter is the phase shift $\phi = 2\phi_u \frac{\omega}{\omega_0} \cos(\alpha)$, where ϕ_u is a user defined phase that can be varied for a simulation (such as dithering), ω/ω_0 is the ratio of the reflected to incident angular wave frequency and α is the angle between the beamsplitter front surface and the incident field vector In1. As it turns out, most of the resonators in the following simulations use beamsplitters to represent the cavity mirrors.

the lengths and optical parameters serves as a good starting point for simulating the entire interferometer. To incorporate more realistic numbers, in-situ measurements were taken at Hanford with a beam scanner and ruler at HAM6 to understand the Gaussian beam shape entering the output mode cleaner. By defining the optical parameters and distances, FINESSE creates coupling matrices for individual components which are generally comprised of mirrors, spaces, or beamsplitters. Some specialized components are also useful such as modulators to create sideband fields, Faraday isolators, and detectors (both amplitude and power). For each component, there are corresponding nodes that link the entire optical system together. The coupling matrices are compiled into an interferometer matrix and the solutions are found numerically,

$$\hat{M}_{ij}^{\text{IFO}} \left| x_{\text{sol}} \right\rangle = \left| x_{\text{input}} \right\rangle \tag{4.136}$$

where $|x_{\text{sol}}\rangle$ and $|x_{\text{input}}\rangle$ are the solution and input vectors, respectively. Generally, the right hand side is made up of laser inputs, modulator sidebands, noise, and signal sidebands. This form has incredible efficiency and can represent the entire interferometer in a single matrix with direct access to all field amplitudes. In addition, changing optical parameters during a simulation is made easier by varying the coupling coefficients after the matrix has been calculated so the algorithm does not have to re-compute every term.

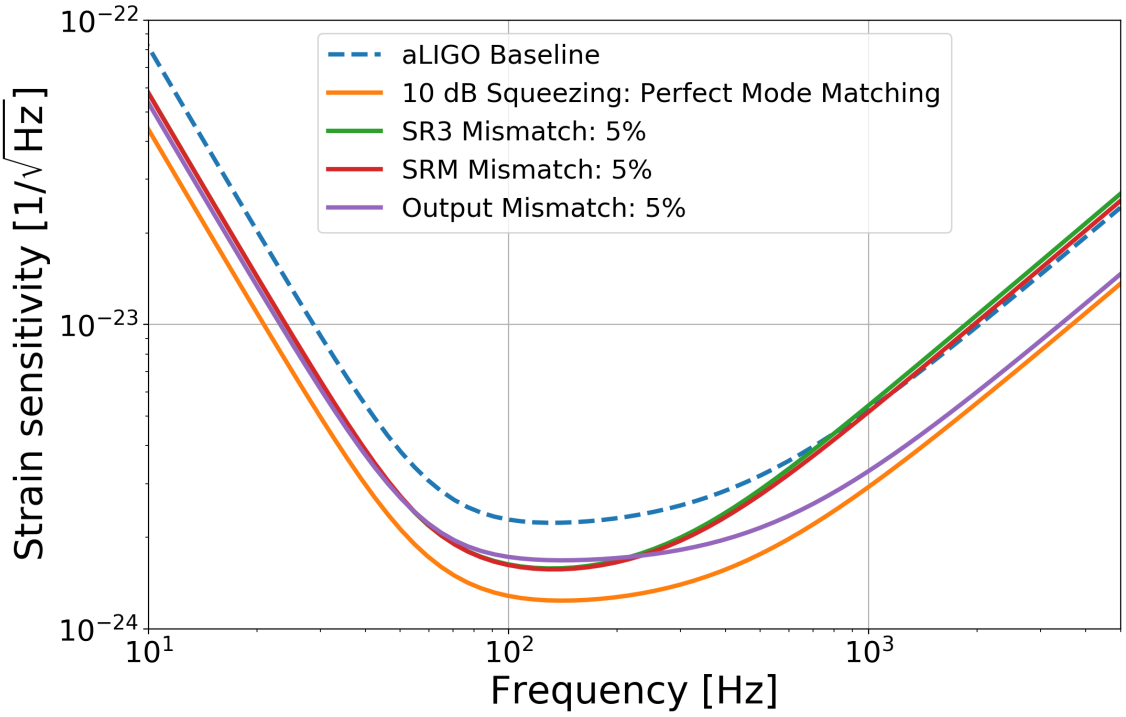

Figure 25 : **Quantum limited sensitivity simulation to compare mismatches in the presence of squeezed light.** With 10 dB of broadband squeezing, the simulation introduced mismatch at various actuators to change the mode shape at the output port. Although there is still 5% mismatch in each case, the introduction of quantum noise and the degradation of squeezing is much worse when introducing losses in the signal recycling cavity as opposed to the output train. In addition, mismatching the signal recycling cavity will change the relative phase angle between the interferometer and squeezed light which has to be re-optimized.

4.2 Effects of Signal Recycling Mismatch

Beam tracing in FINESSE starts by determining the q-parameters for each user defined cavity. If there are multiple cavities, it will calculate in the order written and the last cavity in the parameter file sets the basis of populating the rest of the interferometer. Table 4 shows the extracted cavity values for reference. The algorithm continues by automatically propagating the laser beam through each node via ABCD transformation methods. For a perfectly mode-matched interferometer, the q's at each node are the same no matter which cavity basis is chosen but this is not true when introducing thermal lensing or errors for individual resonators. At this point, it becomes extremely important to properly track the q-parameters because they are

used to calculate the overall mismatch between cavities. To simplify the use of multiple coupled resonators, it is useful to turn all but one of the cavity commands off so that only one basis q-parameter is explicitly used and there is no ambiguity.

FINESSE has the ability to determine two parameters which calculate the sensitivity: noise and signal. By default, vacuum fluctuations are present at each unused port and associated optical losses. This methodology can be verified analytically using the full quantum mechanical description in Section 2.2 and the semi-classical Schottky shot noise estimation. For radiation pressure effects, the mechanical transfer function is defined by a simpled pendulum with $H(f) \propto \frac{1}{M f^2}$ dependence above the resonance frequency which is chosen to be approximately 0.1 Hz for these simulations. As previously shown in Section 2.2, the radiation pressure effects are proportional to the input laser power and convert amplitude fluctuations into phase noise. Naturally, this is a nonlinear equation so FINESSE makes certain approximations which reduces the complexity,

1. Induced motion from radiation pressure is very small compared to the light wavelength so the equations of motion can be linearized.

2. Signal sideband frequencies are very small compared to the optical sidebands created by the modulator such that the carrier creates a much larger radiation pressure effect.

3. The amplitude of signal sidebands are much smaller than the carrier.

In terms of gravitational wave detectors, these approximations are reasonable because the machines tend to operate with closed-loop control systems and in steady-state equilibrium. Also, the signal sidebands never reach above 8 kilohertz for two reasons: astrophysical sources from compact binaries coalesce at around 1.5 kHz and the Nyquist frequency for the differential arm channel is sampled at 16 kHz so the Nyquist frequency is much smaller compared to the 9 MHz sideband from the electro-optical modulator.

To generate the signal, differential arm motion is simulated by varying the two arm cavity lengths 180 degrees out of phase and measuring the optical gain transfer function at the output mode cleaner transmission port. The results can be compared directly to the analytical transfer function described be equation 2.60 to verify the right DC amplitude and pole frequency.

With regards to the squeezer implementation, the model applies both squeezed light and a filter cavity before entering the interferometer to compare the effect of mode-matching losses on the quantum limited sensitivity. In FINESSE, the squeezer node employs a classical sideband implementation while in reality, modified vacuum is generated using the optical parametric oscillator (OPO) [49]. This requires using a bow-tie cavity with a nonlinear optic that is not yet handled by the available FINESSE components and the nonlinear crystal actually keeps the cavity from being geometrically unstable. So for now, it is enough to use quantum noise sidebands whose defined phase and amplitude variances have two open parameters, the squeezing gain and phase angle.

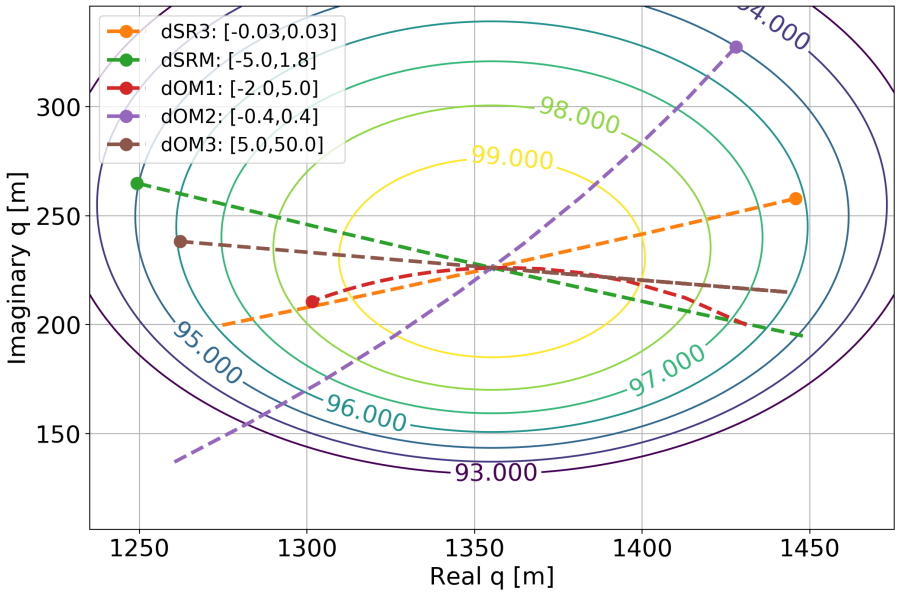

Figure 26 : **Simulating the output actuator phase spaces projected onto the OMC mode basis.** The ending dots indicate the positive direction for changing radii of curvature as seen by the various optics. Also, the change in radii of curvature in units of meters is shown on the legend.

LIGO's coupled optical cavities allow for a large parameter space when trying to match multiple resonators. Changing the curvature of an optic in the signal recycling cavity will obviously change its overlap with the output mode cleaner but the effect will also vary the arm mode propagation to the OMC as well. This will have a confusing result because it is impossible to discern whether the degradation in performance

is due to the arm or SRC mismatch. One of the ways to get around this is to implement a perfect mode-matching telescope between the SRC and OMC to keep the arm modes consistent with the output mode cleaner so that the only effect on the interferometer is a non-optimal signal recycling cavity. The deterioration in sensitivity when mismatching the SRC has a two-fold effect. The introduction of vacuum fluctuations will degrade the squeezed field in a nonlinear fashion hence increasing the noise (even with perfect squeezing phase). On top of that, extra SRC losses will affect the total optical signal gain at the antisymmetric port, which means using the SRC to mode match the squeezer field will not actually improve the sensitivity if the SRC will be mismatched from the arm cavities. Comparatively, mode mismatch introduced at the antisymmetric port before entering the output mode cleaner will only create extra noise from the degradation of squeezing. The comparison is shown in Figure 25.

By allowing FINESSE to do the ray tracing algorithm for the entire interferometer, it is relatively straightforward to change the radii of curvature for different optics and project the effect onto the OMC in order to understand the orthogonality when choosing mirrors for mode matching. In Figure 26, the most orthogonal actuators for small mismatches happen to be SRM and OM2. However, OM1's actuation intersects SRM in phase space at about 96% mode mismatch in the negative direction so for large mismatches OM1 may be more orthogonal to OM2. (It is worthwhile to note that some literature will convert the phase space units to waist size and curvature instead of the imaginary and real parts of the q-parameter.)

A useful tool to understand the actuation matrix in a full interferometer configuration is to calculate the induced waist position or size shift per diopter in Tables 2 and 3. The code runs through each optic and slightly varies the radius of curvature or focal length and traces the beam for every cavity eigenmode. This assumes the mismatches are relatively small so the slope is linear and can give a bit of insight on the directionality and magnitude of the actuators.

The simulations in this chapter correctly models the interferometer fields and showed that mode mismatch between various cavities to the output mode cleaner will affect the quantum limited sensitivity differently. Further, signal recycling cavity mode mismatching will degrade the squeezing more than mismatch originating from optical train prior to entering the output mode cleaner even if the amount mismatched is the same.

	PRC w	PRC S	SRC w	SRC S	ARMs w	ARMs S	OMC w	OMC S
PRM	4.537	0.006	0.000	0.000	0.000	0.000	0.000	0.000
PR2	-45.004	-0.058	0.000	0.000	0.000	0.000	0.000	0.000
PR3	-3321.891	-4.315	0.000	0.000	0.000	0.000	0.000	0.000
SRM	0.000	0.000	-5.097	-0.006	0.000	0.000	0.875	1.114
SR2	0.000	0.000	-128.889	-0.160	0.000	0.000	-2.792	-99.513
SR3	0.000	0.000	-5460.964	-6.774	0.000	0.000	-19.564	-4294.447
ITMTL	-3188.263	4142.666	-5254.308	4140.289	0.000	0.000	0.000	0.000
ITM	-2310.433	3002.047	-3807.633	3000.325	-1827.435	3002.782	0.000	0.000
ETM	0.000	0.000	0.000	0.000	3774.807	4.682	0.000	0.000
OM1	0.000	0.000	0.000	0.000	0.000	0.000	0.164	0.552
OM2	0.000	0.000	0.000	0.000	0.000	0.000	0.511	-0.889
OM3	0.000	0.000	0.000	0.000	0.000	0.000	-0.222	-0.453

Table 2 : **Mode matching actuation matrix for the transverse x direction.** Each of the row elements represent actuators and columns show the affected cavity defocus S or beam size w per diopter change, which are scaled by the initial perfect mode matching values. For small mismatches, the slope is assumed to be linear.

	PRC w	PRC S	SRC w	SRC S	ARMs w	ARMs S	OMC w	OMC S
PRM	5.092	0.006	0.000	0.000	0.000	0.000	0.000	0.000
PR2	-52.019	-0.062	0.000	0.000	0.000	0.000	0.000	0.000
PR3	-3852.041	-4.569	0.000	0.000	0.000	0.000	0.000	0.000
SRM	0.000	0.000	-6.870	-0.007	0.000	0.000	0.870	1.105
SR2	0.000	0.000	-178.704	-0.169	0.000	0.000	-2.783	-99.469
SR3	0.000	0.000	-7589.021	-7.189	0.000	0.000	-19.509	-4292.095
ITMTL	-3700.089	4142.316	-7309.182	4139.780	0.000	0.000	0.000	0.000
ITM	-2681.338	3001.794	-5296.743	2999.956	-1827.470	3002.700	0.000	0.000
ETM	0.000	0.000	0.000	0.000	3774.854	4.697	0.000	0.000
OM1	0.000	0.000	0.000	0.000	0.000	0.000	0.172	0.557
OM2	0.000	0.000	0.000	0.000	0.000	0.000	0.508	-0.887
OM3	0.000	0.000	0.000	0.000	0.000	0.000	-0.165	-0.344

Table 3 : **Mode matching actuation matrix for the transverse y direction.**

Parameters	IMC	XARM	YARM	PRX	PRY	SRX	SRY	OMC
Rayleigh Range [m]	13.338	427.807	427.807	5.314	5.314	2.132	2.132	0.708
Waist to 1st Mirror [m]	-16.473	-1834.220	-1834.220	6.940	6.940	4.733	4.733	0.141
Cavity Length [m]	16.473	3994.500	3994.500	57.711	57.632	56.065	55.985	0.566
FSR [MHz]	9.099	0.038	0.038	2.597	2.601	2.674	2.677	264.975
RT Gouy Phase [deg]	102.008	-48.661	-48.661	51.724	51.722	38.311	38.309	78.979
Pole Frequency [kHz]	8.636	0.045	0.043	309.692	309.939	409.982	410.283	321.971
Finesse	526.837	413.523	436.867	4.193	4.196	3.261	3.263	411.488
A	1.000	-2.559	-2.559	-0.406	-0.406	-0.591	-0.591	-0.004
B	32.946	-6225.726	-6225.726	11.286	11.286	7.835	7.835	0.722
C	-0.073	0.002	0.002	-0.148	-0.148	-0.291	-0.291	-1.387
D	-1.416	3.880	3.880	1.645	1.645	2.161	2.161	0.386

Table 4 : **Calculated cavity parameters for the advanced LIGO interferometer.** The values were obtained using FINESSE's *cav* commands which are an integral part of the beam tracing algorithm. Here, the power (and signal) recycling cavity is split into two linear resonators made up of the PRM and HR surface of the respective ITMs. In an ideal world, the reflectivity of ITMX and ITMY are the same but can actually vary up to 5% in the case of H1 [28]. This mostly affects the arm cavity finesse but can have small effects on the power recycling cavity as well.

Chapter 5

Experimental Mode Matching Cavities at Syracuse

In conjunction with Magaña-Sandoval et al [64], the table-top adaptive mode matching experiment was able to show the feasibility of a fully dynamical system at Syracuse University. Most of the work done by the author of this dissertation was focused on converting and upgrading the real-time digital sysem (RTCDS) from being used by the optical trap experiment [73] to adaptive mode matching and interfacing the analog RF sensors into the digital system. There is also a section on the usage of cylindrical lenses and quadrant photodiodes as a viable method of extracting a mode matching error signal.

5.1 Commissioning the Real Time Digital System

Dynamic control systems require both actuators and sensors which are interfaced in a real-time manner and this requires the use of analog-to-digital (ADC) and digital-to-analog (DAC) converters. A LIGO standard system uses a front end computer that reads in data and processes the signals based on a Simulink graphical model that allows for simple logic, mathematical operations, and frequency-dependent filtering. The real time data acquisition code is user-interfaced with a Motif Editor and Display Manager (MEDM) that is able to report and execute variables such as gains and matrix elements. The use of a LIGO standard digital system means that hardware and software developed at Syracuse can be transferred smoothly to the LIGO sites.

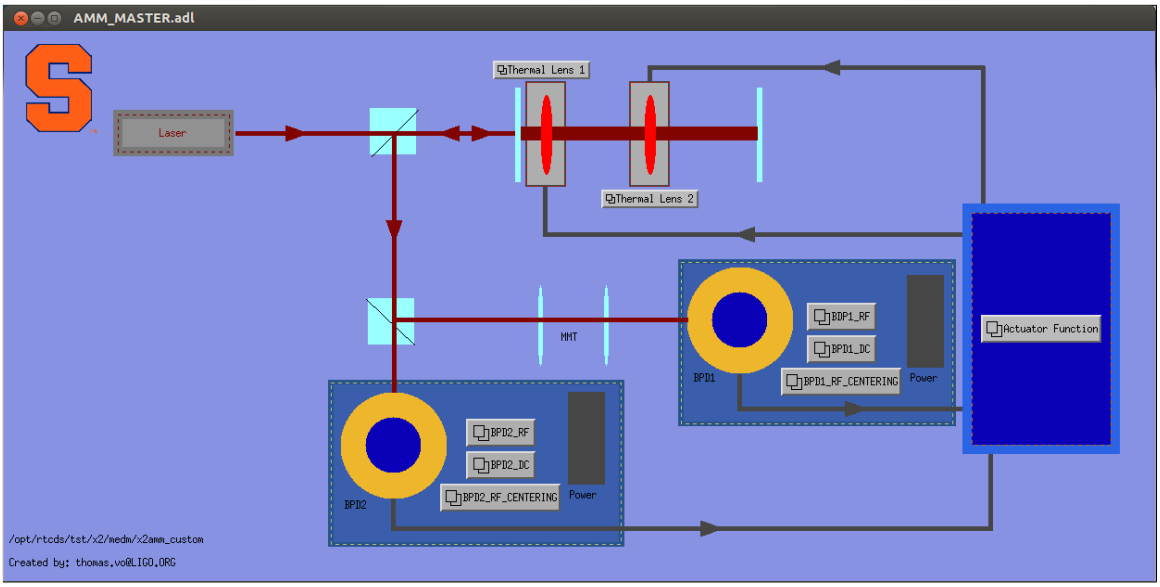

Figure 27 : **MEDM master screen for adaptive mode matching at Syracuse.** Here, the demodulated error signal in reflection of the Fabry-Perot cavity is divided by a beamsplitter and fed into two RF detectors, one of which is depicted to have a mode matching telescope MMT to project a different Gouy phase to sense an orthogonal degree of freedom. Then the signal is sent to an actuator function which allows for diagonalizing the signals and can be sent to a set of thermal lens at different Gouy phases for actuation. The adaptive lenses are actually placed in the beam path before entering the cavity but for demonstrative purposes, they are portrayed at two different Gouy phases of the resonator.

5.2 Sensors

Recall in Section 3.2 that the RF modal decomposition technique relies on comparing the Gouy phase of higher order modes to the fundamental Gaussian mode with an array of RF photodiodes in order to extract an error signal. The complication arises when using this method to extract the beat note between the fundamental mode and symmetric donut mode because the photodetector arrays must match the higher order mode geometry. This is easier to deal with when trying to sense angular distortions from a misaligned cavity because the 01 and 10 modes can be sensed with a split photodetector, however, using a quadrant photodiode will not work to sense mode mismatch due to the cylindrical symmetry of the 02 and 20 modes. Currently, Advanced LIGO uses no RF sensors to detect mode mismatch so the next sections will provide sensing methods which can be used for dynamic closed loop feedback control.

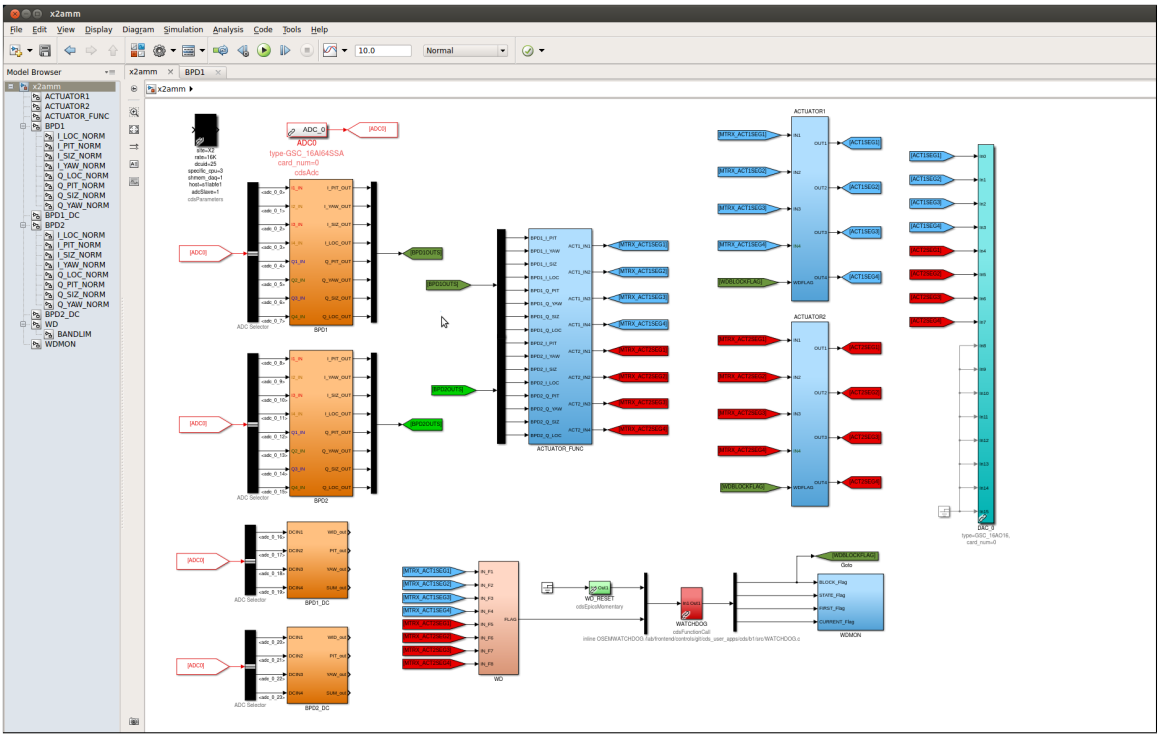

Figure 28 : **Model overview for adaptive mode matching.** Using the LIGO digital system as a test bed for technology development has the advantage of easy integration at both LIGO sites. The Syracuse system uses a Simulink style model with LIGO standard modules to read in data from the analog-to-digital converter (ADC) that contain signals from each RF photodiode segments, apply a phase rotation to get the signal into one quadrature (nominally I for a linear cavity) and normalize by the total power on the sensor. Afterwards, the signals are sent to a master actuator function that diagonalizes the sensor signals into an actuators basis and sent to the digital-to-analog converter (DAC) to control the heater drivers.

5.2.1 Bullseye Photodiodes (BPD)

It is clear that using a quadrant photodetector to measure the symmetric $U_{20} + U_{02}$ mode which arises from mismatch is futile because the integrated power on each side will be exactly the same due to donut mode symmetry. So it is simplest to try subtracting the inner beam power from the outer ring of the electric field in order to measure a phase difference using a specialized RF photodiode called a Bullseye Photodetector (BPD) shown in Figure 29. This method was proven to work in the Enhanced LIGO era [69] and is the most natural extension of the angular wavefront sensing/controls that is widely implemented in Advanced LIGO.

Figure 29 : **RF Bullseye Photodiode.** The left figure shows the analog readout electronics and the right gives segment numbers used in the sensing matrix.

Calibration

To use the BPDs, there are a few steps required in designing the optical setup which is different than the standard PDH or WFS method. Most notably, the beam size incident on the BPD must be tuned such that the zero crossing of the $(U_{20} + U_{02})$ matches the boundary between the inner and outer segments. This condition is met if $\omega_0 = \sqrt{2} r_0$ which gives a well defined power ratio of the outer to inner segments as

$$\text{Power Ratio} = \frac{\mathrm{P}_1 + \mathrm{P}_2 + \mathrm{P}_3}{\mathrm{P}_4} = \frac{e^{-2r_0^2/\omega_0^2}}{1 - e^{-2r_0^2/\omega_0^2}} \approx 0.582 \tag{5.137}$$

In Appendix C, the complete derivation for the sensitivity of QPDs (Pitch/Yaw) and BPDs (Pitch/Yaw/Width) is explicitly shown for DC mismatches. Another constraint is that the Gouy phase separation between successive BPDs must be close to 45 or 135 degrees such that the error signals from each BPD can be orthogonalized, this is in contrast to angular wavefront sensors which require 90 degree Gouy phase separation.

5.2.2 Mode Converters

The bullseye photodiodes can be difficult to calibrate and manufacture so a particularly interesting method of sensing mode mismatch is to convert the axially symmetric fields with a cylindrical telescope such that an error signal can be extracted with a

quadrant photodiode. This process is shown to preserve both the angular and modal mismatch error signals. Using lenses which have two radii of curvature for each direction (x or y) with one being flat and the orthogonal is curved with some focal length, f. The idea is to break the cylindrical symmetry of the donut mode (Figure 30) and convert the beam into a pringle mode by advancing the phase of one axis by a factor of $\pi/2$ to create a relative sign flip. Then, an error signal can extracted using the radio frequency quadrant photodiode that the angular wavefront sensors employ.

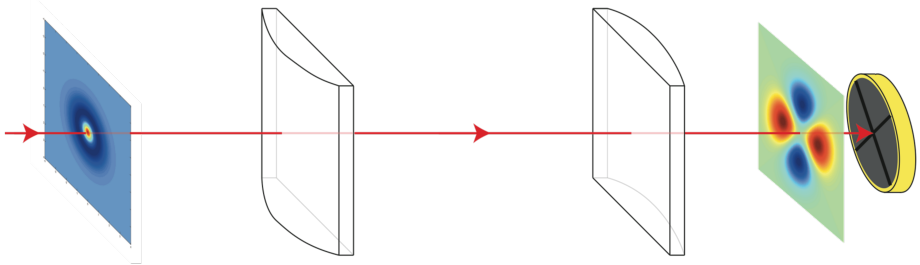

$$|\mathrm{LG}_{1,0}\rangle = \frac{1}{\sqrt{2}}\big(|\mathrm{HG}_{2,0}\rangle + |\mathrm{HG}_{0,2}\rangle\big) \qquad \frac{1}{\sqrt{2}}\big(|\mathrm{LG}_{2,0}\rangle + |\mathrm{LG}_{0,-2}\rangle\big) = \frac{1}{\sqrt{2}}\big(|\mathrm{HG}_{2,0}\rangle - |\mathrm{HG}_{0,2}\rangle\big)$$

Figure 30 : **Passing a bullseye mode through a $\pi/2$ mode converter.** The reflected fields of a well aligned Fabry-Perot cavity with a slight mode mismatch will have a large contribution from the $|\mathrm{HG}_{20}\rangle + |\mathrm{HG}_{02}\rangle$ mode which is cylindrically symmetric. After passing through a cylindrical telescope which has a $\pi/2$ phase advance for one axis, there is a relative sign flip which breaks the the symmetry and the error signal can be extracted with an RF quadrant photodiode.

Vector formalism for laser beams and optical cavities

Consider an optical cavity that is longitudinally resonant on the TEM_{00} mode using the Pound-Drever-Hall technique shown in Section 2.1.2 and also locked with angular wavefront sensors shown in Section 3.2. When there is a small mismatch between the waist size and position of the input beam relative to the cavity, this is equivalent to coupling the TEM-00 mode into higher order modes. Since mode matching is only concerned with coupling to the second order modes, the resultant field in reflection (r_{FP}) of a Fabry-Perot resonator will have the form

$$|U_{refl}\rangle = r_{FP}\begin{pmatrix} U_{00} \\ 0 \\ 0 \end{pmatrix} + \epsilon\begin{pmatrix} 0 \\ U_{20} \\ U_{02} \end{pmatrix} \tag{5.138}$$

$$\epsilon = \frac{1}{\sqrt{2}}\left(\frac{\delta w}{w_0} + i\frac{\delta z}{z_R}\right) \tag{5.139}$$

where δw and δz are the mismatches in waist size and position, respectively. O'Neil et al [72] wrote down a formalism that explicitly showed the effects of cylindrical telescopes on the full range of Hermite Gauss modes. An arbitrary mode conversion system, $\hat{M}$, is comprised of two cylindrical lenses and can be described by two distinct operators,

$$\hat{M} = \hat{R}\hat{C} \tag{5.140}$$

where $\hat{R}$ is a rotation operator that depends on a angle θ which can rotate about the axis of propagation and $\hat{C}$ is the mode converting operator which depends on the amount of phase advance seen by higher order modes. Physically, $\hat{R}$ can be shifted by rotating the entire cylindrical telescope about the axis of propagation whereas the phase advance can be changed by choosing various focal lengths. Since mode matching primarily couples power into the 02 and 20 modes of the cavity, we can use a 3x3 matrix. For rotations about the axis of propagation, the operator is

$$\hat{R}_{ij} = \begin{pmatrix} 1 & 0 & 0 \\ 0 & \cos(\Delta\theta) & \sin(\Delta\theta) \\ 0 & -\sin(\Delta\theta) & \cos(\Delta\theta) \end{pmatrix} \tag{5.141}$$

For the mode converter phase advance, the operator is

$$\hat{C}_{ij} = \begin{pmatrix} 1 & 0 & 0 \\ 0 & e^{-i\Omega_{20}} & 0 \\ 0 & 0 & e^{i\Omega_{02}} \end{pmatrix} \tag{5.142}$$

where $\Omega_{mn} = (m+\frac{1}{2})\tan^{-1}\left(\frac{d}{z_{R,x}}\right) + (n+\frac{1}{2})\tan^{-1}\left(\frac{d}{z_{R,y}}\right)$ and d is the distance from one cylindrical lens to the waist. Ω_{mn} is the amount of phase advance that a higher order mode will experience due to the mode converter. It is important to note, the matrices above show that the Gaussian beam is only astigmatic within the region of between the cylindrical lenses and unchanged outside of the telescope. If the beam reflected from the cavity is well mode matched to the cylindrical telescope, then a mode converter will introduce an astigmatism and vary the separate Rayleigh ranges

[7],

$$\frac{z_{R,x}}{z_{R,y}} = \frac{1 + d/f}{1 - d/f} \tag{5.143}$$

Of course, the tuning of θ, d and f is left up to the optical designer's choice. The obvious selection for θ should rotate the output beam such that the pringle mode intensities are centered on the individual quadrant photodiodes. The choice of separation distance d and focal length f are a bit more subtle.

The second order coupling to higher order HG modes from mode mismatch creates a cylindrically symmetric intensity profile. This can be broken by creating a phase difference between HG20 and HG02 such that there is a relative sign flip. In Figure 31 of O'Neil [72], the only conversion that transforms the diagonal HG mode into a symmetric donut mode is with $\Delta\Omega = \pi/2$. This implies the converse is also true if one desires to transform the donut mode into an HG mode of the same order. Making this choice of phase propagation automatically constrains the optical setup and the second order mode along the lens axis will see a phase advance equal to

$$\frac{\pi}{2} = 2\left[\tan^{-1}\left(\frac{d}{z_{R,x}}\right) - \tan^{-1}\left(\frac{d}{z_{R,y}}\right)\right] \tag{5.144}$$

$$\Rightarrow \sqrt{2} - 1 = \frac{d}{z_{R,y}} = \frac{z_{R,x}}{d} \tag{5.145}$$

The equation above only shows a relation between the Rayleigh ranges and the lens separation. However, by imposing mode matching conditions it is possible also constrain the focal length of the cylindrical lenses as well.

$$f = \left[\frac{1}{R_x(d)} - \frac{1}{R_y(d)}\right]^{-1} = \frac{d}{\sqrt{2}} \tag{5.146}$$

where $R_i(d) = d[1 + (\frac{z_{R,i}}{d})^2]$.

Extracting information from mode

Mueller et al [69] showed that the error signal from mode mismatch could be extracted by using an RF detection scheme. Using this formalism, the error signal on a quadrant

photodetector from a mismatched cavity after a mode converter is

$$
\begin{aligned}
S \propto \mathrm{Im}\Bigg\{\epsilon^*\Bigg[\int_{A1,A3} \hat{M}_{00}^\dagger \langle U_{00}| \left[\hat{M}_{U_{20}}^\dagger |U_{20}\rangle + \hat{M}_{U_{02}}^\dagger |U_{02}\rangle\right] - \\
\int_{A2,A4} \hat{M}_{00}^\dagger \langle U_{00}| \left(\hat{M}_{20}^\dagger |U_{20}\rangle + \hat{M}_{02}^\dagger |U_{02}\rangle\right)\Bigg]\Bigg\} \qquad (5.147) \\
\propto \mathrm{Im}\Bigg\{\epsilon^*\Bigg[\int_{A1,A3} \langle U_{00}| \left(|U_{20}\rangle - |U_{02}\rangle \right) - \int_{A2,A4} \langle U_{00}| \left(|U_{20}\rangle - |U_{02}\rangle\right)\Bigg]\Bigg\}
\end{aligned}
$$

where the surface integrals are over each segment. In the above equation, $\hat{C}_{ij}$ was chosen with $\Delta\Omega = \pi/2$ and $\hat{R}_{ij}$ should rotate the beams such that the intensities in Figure ModeConverter are aligned with the quadrant photodiodes.

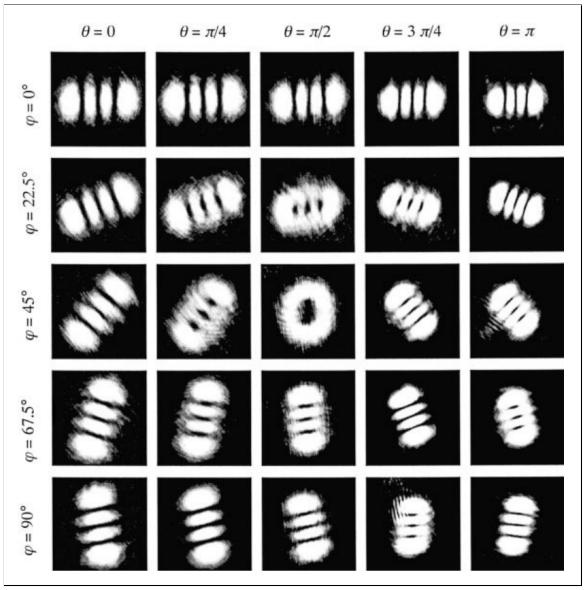

Figure 31 : **Intensity profiles passing through a mode converter [72].** The image in upper left corner represents the $m = 3$ and $n = 0$ Hermite Gauss (LG) mode which gets transformed through a converter for different rotations and phase advances. The only combination which gives a symmetric Laguerre Gauss (LG) mode is $\phi = 45\,\mathrm{deg}$ and $\theta = \pi/2$. This gives some intuition about how to reverse this process to take an input LG mode and breaks the cylindrical symmetry so that the modal content can be sensed by a quadrant photodiode.

5.2.3 DC Mode Matching

The benefit to using the RF sensing scheme for generating an error signal is the automatic reduction of the higher order mode content which can use actuators to adjust

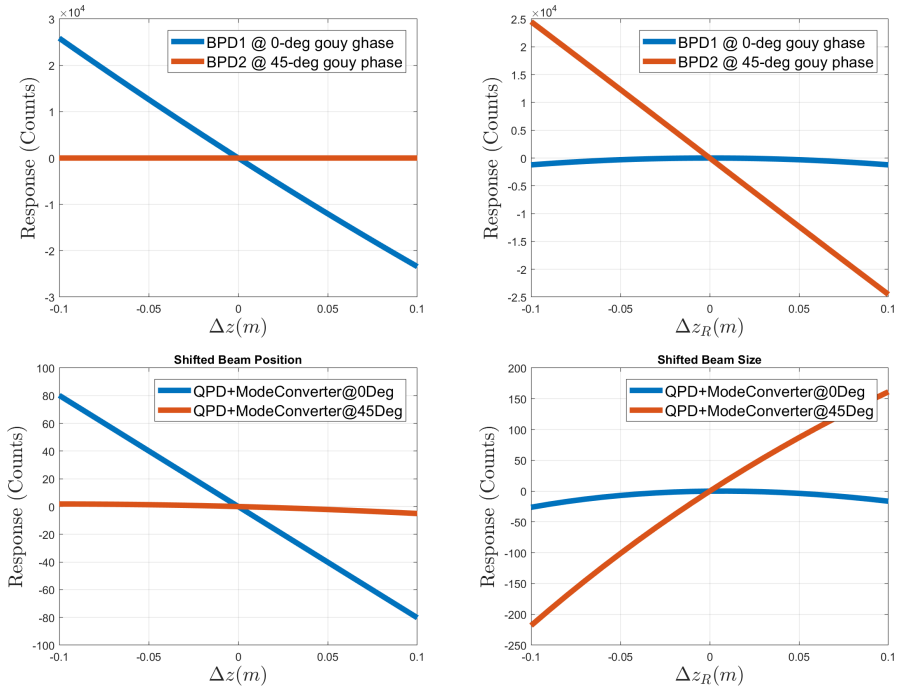

Figure 32 : **Simulated error signals from MATLAB (QPD) and FINESSE (BPD).** A numerical simulation of the error signal in reflection from a linear Fabry Perot cavity with different detectors when varying either the waist position (Δz) or Rayleigh range (Δz_R). The error signal orthogonality at two different Gouy phases is demonstrated using both sensing schemes for active wavefront control.

the incoming mode of the beam to whatever the cavity requires. This is particularly useful in areas where the laser power density is high and absorption on the high reflectivity surfaces cause thermal distortions in the cavity mode. However, the output mode cleaner remains fixed in its eigenbasis regardless of interferometer heating such that the nominal input mode is also static; in fact, the current alignment scheme uses DC quadrant photodiodes to feed back to the OMC suspensions and the control loop offsets are tuned to minimize the 10/01 modes. If there was a low-noise way to continually measure the beam size at two different Gouy phases prior to entering the output mode cleaner, then there could be an error signal which would be used for thermal actuators directly after the signal recycling cavity. This can be achieved with bullseye sensors that read power ratio relatively quickly. Another interesting way of measuring the mode is using a slowly rotating razer blade with known angular frequency in front of a single photodiode and inferring the error function which will directly give the beam size.

Chapter 6

Wavefront Control at LIGO Hanford

Simulations and calculations are wonderful guides to understanding and building intuition about mode matching, no model is perfect and experiments have a way of presenting the most interesting and challenging problems. Preparation for the third observing run (O3) required extensive work to understand Advanced LIGO's path to achieve higher arm power. One of the most important tasks was tuning the thermal compensation and interferometer sensing/controls systems in order to maintain the power build-ups in the PRC and the long interferometer arms during nominal low noise operation. This chapter will explain how lensing affects the interferometer fields and describe a few strategies to tune the Thermal Compensation System (TCS) at LIGO Hanford. Then, it summarizes in-situ measurements that were taken to understand the mode matching between the squeezer optical parametric oscillator (OPO) and the output mode cleaner in single bounce configuration.

For Advanced LIGO, test mass heating comes from main two sources: absorption by arm cavity optics from the main interferometer beam and heat applied by the TCS which is meant to combat the wavefront distortion by applying heat in key places. Thermal compensation currently utilizes ring heaters at all four main test masses, a disk heater at the SR3, and CO_2 lasers at the input test masses.

6.1 Hot vs. Cold Interferometers

When fully operational, the arm cavities can have approximately 150 kilowatts of circulating power. An estimated but useful description of the total arm power in each arm is

$$P_{\mathrm{ARM}} \approx \frac{1}{2}(g_{\mathrm{PRC}} * g_{\mathrm{ARM}} * P_{\mathrm{in}}) \tag{6.148}$$

where $g_{\mathrm{PRC}} \approx 45$ is the power recycling cavity gain and $g_{\mathrm{ARM}} \approx 225$ is the single arm cavity gain. For O3, the intended input power P_{in} will reach approximately 30 W which means $P_{\mathrm{ARM}} \approx 150,000$ W. A fraction of that power between (0.2-0.8 ppm), will be absorbed by the high reflectivity surface creating a *thermo-elastic* effect which changes the radius of curvature. By changing the test mass curvatures, the resonant Gaussian mode will also change its profile. Additionally, the *thermo-refractive* effect will vary the index of refraction within the bulk as a function of absorbed light power creating a thermal lens that turns out to be an order of magnitude larger than the wavefront distortion from thermo-elastic effects in fused silica [91].

6.1.1 Thermal Lensing

As seen in Section 2.1.5, the sideband and carrier frequencies propagate differently in the interferometer by design, which means their fields see different thermal lensing effects. The ITM substrate which sees the thermo-refractive change from absorption will play the largest role because the carrier is not affected to first order (shown below). To understand how the fields change, the easiest way is to invoke the ABCD transfer matrix approach to track how the phase changes as they propagate through the optical system [62].

Carrier

The carrier is resonant in the 4 kilometer arm cavities as well as the PRC, so a simplified model resembles a coupled cavity setup where there is already a locked resonator with some leakage beam and there is an input mode propagating from the power recycling cavity. Consider the diagram in Figure 33, which shows a two-mirror optical system with an input carrier beam, $|E^c_{\mathrm{in}}\rangle$, that has a portion promptly reflected

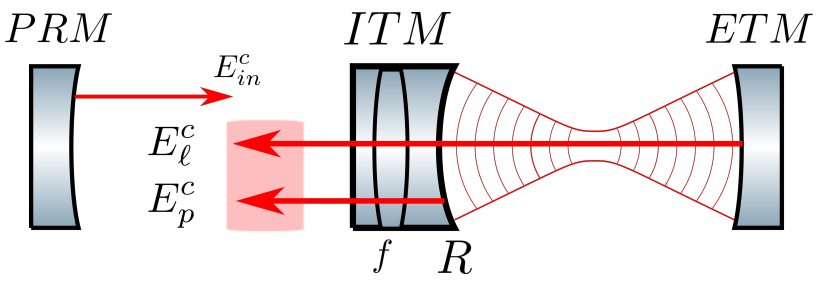

Figure 33 : **A simplified model for the effect of a substrate thermal lens on the carrier field.** An input beam, $E^c_{\rm in}$, from the power recycling mirror (PRM) will have a radius of curvature that mode matches to the input test mass (ITM). The promptly reflected beam, E^c_p, is denoted by equation 6.151 and the leakage beam, E^c_ℓ, is expressed by equation 6.152 where the sum of them would make the total reflected beam. The leakage field will have the same shape as the ITM radius of curvature R when exiting the arm and see the thermal lensing f. The promptly reflected field will also see the lens f twice but when combined with the leakage beam, the *total* reflected field is not affected by the thermal lens.

off the input mirror to create $|E^c_p\rangle$

$$|E^c_p\rangle = \hat{M}^c_p\,|E^c_{\rm in}\rangle \tag{6.149}$$

The prompt reflection is made up of a beam incident on a converging lens from the substrate and a single reflection from the input coupler's convex surface, therefore, the transfer matrix is

$$\hat{M}^c_p = \begin{bmatrix} 1 & 0 \\ -\frac{1}{f} & 1 \end{bmatrix} \begin{bmatrix} 1 & 0 \\ +\frac{2}{R} & 1 \end{bmatrix} \begin{bmatrix} 1 & 0 \\ -\frac{1}{f} & 1 \end{bmatrix} \tag{6.150}$$

where R is the radius of curvature of the high reflectivity (HR) surface and f is the thermal lens of the mirror substrate. In general, this can be a combination of the static lens and any thermal effects which create additional (intentional or non-intentional) lensing.

$$|E^c_p\rangle = \hat{M}^c_p \begin{bmatrix} 1 \\ \frac{1}{q_{\rm in}} \end{bmatrix} = \begin{bmatrix} 1 \\ \frac{1}{q_{\rm in}} + 2\left(\frac{1}{R} - \frac{1}{f}\right) \end{bmatrix} = \begin{bmatrix} 1 \\ \frac{1}{q_{\rm p}} \end{bmatrix} \tag{6.151}$$

Here, $\frac{1}{q_{\rm in}} = -\frac{1}{R_{\rm in}} - i\frac{\lambda}{\pi w^2}$, is the q-parameter of the input beam where w is the beam size on the HR surface and $R_{\rm in}$ is the radius of curvature entering the cavity and is converging at that point.

In addition, there is also a circulating field inside the cavity which leaks out in reflection and can be denoted by $|E^c_\ell\rangle$ which exits with the input coupler's radius of curvature and sees a single pass through the substrate lens,

$$|E^c_\ell\rangle = \begin{bmatrix} 1 & 0 \\ -\frac{1}{f} & 1 \end{bmatrix} \begin{bmatrix} 1 \\ \frac{1}{R} - i\frac{\lambda}{\pi w^2} \end{bmatrix} = \begin{bmatrix} 1 \\ \frac{1}{R} - i\frac{\lambda}{\pi w^2} - \frac{1}{f} \end{bmatrix} \tag{6.152}$$

The total reflected beam is a summation of the prompt and leaked cavity fields. LIGO uses arms which are highly over-coupled optical cavities so the promptly reflected amplitude is $|E^c_p| \approx |E_{\rm in}|$ and using equation 2.32, the leakage amplitude is $|E^c_\ell| \approx -2|E_{\rm in}|$. Putting all this together, the total reflected field of the carrier is

$$\begin{aligned} E^c_{\rm REFL} &= E^c_\ell + E^c_p \\ &= E_{\rm in}\left[\exp\left(\frac{-ikr^2}{2q_p}\right) - 2\exp\left(\frac{-ikr^2}{2q_\ell}\right)\right] \\ &\approx E_{\rm in}\left[-1 - \frac{ikr^2}{2}\left(\frac{1}{q_p} - \frac{2}{q_\ell}\right)\right] \\ &\approx E_{\rm in}\left[-1 - \frac{ikr^2}{2}\left[\frac{1}{q_{\rm in}} + \frac{2}{R} - \frac{2}{f} - 2\left(\frac{1}{R} - i\frac{\lambda}{\pi w^2} - \frac{1}{f}\right)\right]\right] \\ &\approx -E_{\rm in}\left[1 + \frac{ikr^2}{2}\left[-\frac{1}{R_{\rm in}} + i\frac{\lambda}{\pi w^2}\right]\right] \\ &\approx -E_{\rm in}\exp\left(\frac{-ikr^2}{2}\left[\frac{1}{R_{\rm in}} - i\frac{\lambda}{\pi w^2}\right]\right) \end{aligned} \tag{6.153}$$

The fourth line is where the phase gain due to the substrate thermal lens and test mass radius of curvature will cancel for the prompt reflection and the leakage beams. The last line shows that the total reflected carrier field will be negative of the original amplitude with the same beam size and absolute curvature, however, now the beam is diverging instead of converging. **The amazing part is that the end result is independent of the substrate lensing to first order**. Here, the approximation used to expand the exponential from the second to the third line is valid when considering points close to the beam center ($\frac{kr^2}{R} << 1$) where the paraxial approximation is true [76]. If considering areas where this condition is not strictly true, the model is only meant to show that the first leading order term between the leakage and promptly reflected fields cancel, which will **not** be true for second order effects. Another point

where this model breaks down is when the power recycling mode is altered so much by lensing effects that the PRC is no longer well mode matched to the arms; this leads to the input beam not having the right radius of curvature. At that point, there will be extra losses from higher order mode-coupling. Lensing can also change the radius of curvature to a point where the PRC g-factor makes the resonant mode no longer geometrically stable (see Appendix A), however, this requires significant thermal lensing well beyond what is expected in Advanced LIGO [62]. A numerical FINESSE model uses this simplified geometry to calculate the power recycling gain and arm build up in Figure 48 as a function of round trip losses and thermal lensing.

Sidebands

Using the same formalism as the carrier fields, the sidebands will have the same input curvature, however, they do not resonate in the arms so there is no cavity leakage field. Therefore, the sidebands will see the phase change due to the substrate lens and this has very important consequences on the sideband build up within the power recycling cavity.

GW Signal

As mentioned in Section 2.1.5, LIGO currently employs a DC readout scheme that extracts the signal by beating the carrier field with the audio frequency sidebands created by the gravitational wave. Although the carrier field was shown to be immune from substrate thermal lensing, the gravitational wave sideband field will see a single-passed lensing effect as it propagates out of the cavity and towards the beamsplitter. If there is differential lensing, the signal recycling cavity will see an effective thermal lens, TL_{-}, which will scatter light into higher order modes. This causes a reduction in the amount of gravitational wave signal at the anti-symmetric port that is directly proportional to the mode mismatch between the arms.

6.2 Wavefront Distortions from Thermal Effects

In the previous section, it was shown that lensing in the substrate affects fields in the interferometer differently. The thermal distortions were modeled as a simple addition of phase, however, it is useful to understand how the optical path varies from first

principles. This provides theoretical groundwork for modeling interferometer heating as well as corrective measures using TCS. A lot of work in this field was introduced in the context of gravitational wave detectors by Hello and Vinet [54] [87] where they implemented the Heat Diffusion equation in order to analytically derive the phase change due to thermal aberrations. In general, there are two effects which occur when a beam interacts with an optic which has a temperature field: thermo-refractive and thermo-elastic.

The first arises from the index of refraction changing as a function of the temperature distribution $T(r, z)$,

$$\Delta n_r(r, z) = \frac{\mathrm{d}n}{\mathrm{d}T} T(r, z) \tag{6.154}$$

where $\frac{\mathrm{d}n}{\mathrm{d}T}$ is the temperature index coefficient and is dependent on the optic material, which can be (and often is) inhomogeneous. For example, if the heating source comes from a laser beam which imparts onto the optic a Gaussian-like intensity pattern, inhomogeneities in the optic cause the temperature profile to be non-uniform and thus leading to a varying index of refraction that causes wavefront distortions (see Figure 34).

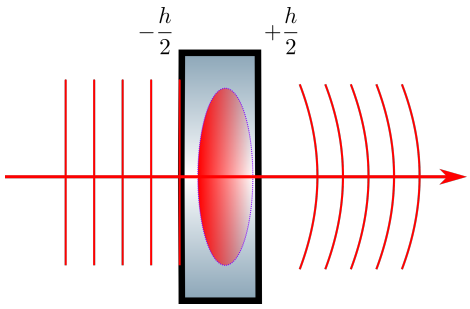

Figure 34 : **A plane wave passing through a lens with a temperature gradient.** The index of refraction, n, depends on the material and temperature so when a plane wave moves through a medium with a non-uniform temperature field, a phase lag or lead occurs in the wavefront. Since $\frac{\mathrm{d}n}{\mathrm{d}T}$ is negative, the distortion will resemble a diverging lens.

To understand how changing the index of refraction varies the optical path length, consider the function $S(r)$ which describes surfaces that are perpendicular to the rays. If $S(r)$ is a known function then the rays can be reconstructed using the gradient, $\nabla S(r)$. As an analogy to electrostatics, $S(r)$ is similar to the potential function V and the electric field is described by $\mathbf{E} = -\nabla \mathbf{V}$. As an extension of ray optics, Fermat's

principle requires that the Eikonal equation be satisfied,

$$|\nabla S|^2 = n^2 \tag{6.155}$$

By integrating along the axis of propagation ($\hat{z}$) in Figure 34 through the substrate, one can find the optical path distortion

$$Z(r) = \frac{\mathrm{d}n}{\mathrm{d}T} \int_{-h/2}^{+h/2} T(r,z)\mathrm{d}z \tag{6.156}$$

It is clear that the temperature field is key to understanding exactly how the wavefront is distorted. In order to analytically solve for $T(r,z)$, one must invoke the famous Heat equation,

$$\kappa \nabla^2 T(r,z) = \rho C \frac{\partial T}{\partial t} \tag{6.157}$$

where κ is the thermal conductivity, ρ is the density, and C is the specific heat. A complete solution for such an equation will be a sum of two parts:

$$T(r,z,t) = T_s(r,z) + T_t(r,z,t) \tag{6.158}$$

where the first term is the steady-state solution which includes the an ambient temperature and a perturbation, $T_s(r,z) = T_p(r,z) + T_0$. The main goal for the remainder of the section will be finding a solution to the perturbation field. The second term is the transient time-dependent solution which will converge to the stead-state as time goes to infinity. For the LIGO test masses which are approximately cylindrical, the heat equation in steady-state equilibrium is

$$\kappa \left[\frac{1}{r} \frac{\partial}{\partial r} \left(r \frac{\partial}{\partial r} \right) + \frac{\partial^2}{\partial z^2} \right] T_s(r,z) = 0 \tag{6.159}$$

The next step is to understand the boundary conditions using Figure 35 and the balance of heat fluxes at each of the surfaces,

$$\mathbf{n} \cdot [\mathbf{F} + \kappa \nabla T_s]_{\mathrm{surf}} = 0 \tag{6.160}$$

Assuming that the outward flux is from radiation which follows the Stefan-Boltzmann

law,

$$\mathbf{n}\cdot\mathbf{F}t_{\text{surf}} = \sigma_B[T_s^4 - T_0^4] = \sigma_B[(T_p(r,z)+T_0)^4 - T_0^4] \approx 4\sigma_B T_0^3 T_p(r,z) \tag{6.161}$$

where σ_B is the Stefan-Bolzmann's constant. It is important to note that σ_B depends on the material and may vary by a scalar amount but for brevity, it is used as a constant here. The last part of the equation assumes that the temperature field is only a small perturbation from the ambient surroundings, $T_p(r,z) << T_0$, which allows the radiation term to become linear. Figure 35 shows boundary conditions for the LIGO test masses,

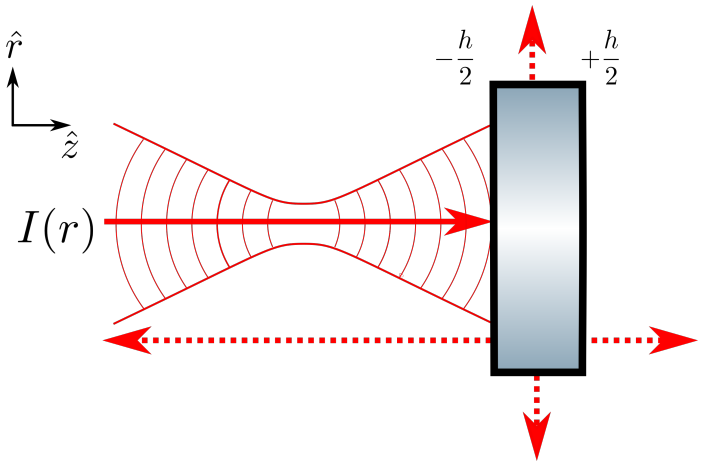

Figure 35 : **A conceptual model of flux balance for a cylindrical object.** The red dotted lines represent the radiative fluxes escaping the optic while a Gaussian beam with intensity profile $I(r)$ is pumping energy in as denoted by the red solid line.

At the surface where $z = h/2$ the total flux is radiative,

$$-\kappa\frac{\partial T_p(r,h/2)}{\partial z} = 4\sigma_B T_0^3 T_p(r,h/s) \tag{6.162}$$

At the barrel of the cylinder where $r = a$, total flux is also radiative,

$$-\kappa\frac{\partial T_p(a,z)}{\partial r} = 4\sigma_B T_0^3 T_p(a,z) \tag{6.163}$$

At the surface where $z = -h/2$ there are two components of flux, one is radiative

and the second is the input power from the laser beam striking the optic surface,

$$-\kappa\frac{\partial T_p(r,-h/2)}{\partial z} = -4\sigma_B T_0^3 T_p(r,-h/s) + \epsilon_a I(r) \tag{6.164}$$

where $I(r) = \frac{2P}{\pi w^2}\exp\{-2r^2/w^2\}$ is the laser beam intensity with power P over a beam size of w and ϵ_a is the absorption coefficient. Here, the radiative term has a negative sign to represent the flux direction. Once boundary conditions are established, most introductory textbooks that deal with partial differential equations will apply an educated guess for the solution. In this case, the resulting temperature field will be a harmonic function,

$$T_p(r,\phi,z) = (Ae^{+kz} + Be^{-kz})J_0(kr) \tag{6.165}$$

where J_0 is the spherical Bessel function of the first kind and k is a constant. Although this particular temperature distribution can be even more general by allowing all the orders of J_n, this form is sufficient. Using the boundary condition from 6.163 and the property $\frac{\partial J_0(x)}{\partial x} = -J_1(x)$,

$$-\kappa k\frac{\partial J_0(kr)}{\partial r}\bigg|_{r=a} = 4\sigma_B T_0^3 J_0(ka) \tag{6.166}$$

$$kaJ_1(ka) - \chi J_0(ka) = 0 \tag{6.167}$$

where $\chi = 4\sigma T_0^3 a/\kappa$ is the reduced time constant. There exists an infinite number of discrete solutions which can solve 6.167 using various values of $k_n a = \rho_n$. The temperature field then becomes,

$$T_p(r,z) = \sum_{n=0}^{\infty}(A_n e^{+k_n z} + B_n e^{-k_n z})J_0(k_n r) \tag{6.168}$$

In order to solve the conditions from equations 6.162 and 6.164, the strategy is use the orthogonality of the spherical Bessel functions in order to expand the equations into a solvable algebraic form. This will include expanding the intensity profile $I(r)$ in this basis as well. Consider the boundary from $r = 0$ to $r = a$, the functions $J_0(k_n r)$ form a complete basis set and the normalization constant is given by the Sturm-Louisville

problem,

$$\int_0^a J_0(k_n r) J_0(k_m r)\, r\, \mathrm{d}r = \delta_{mn} \frac{[\chi^2 + (k_n a)^2]}{2k_n^2} J_0^2(k_n a) = \delta_{mn} \frac{1}{N_n} \tag{6.169}$$

Then expanding the intensity profile in terms of the Bessel function: $I(r) = \sum_n^\infty p_n J_0(k_n r)$ and inverting to solve for p_n leads to,

$$\begin{aligned} p_n &= N_n \int_0^a I(r) J_0(k_n a)\, r\, \mathrm{d}r \\ &= N_n \int_0^a \left[\frac{2P}{\pi w^2}\right] J_0(k_n a) \exp\{-2r^2/w^2\}\, r\, \mathrm{d}r \\ &\approx N_n \frac{P}{2\pi a^2} \exp\left\{-\frac{(k_n w)^2}{8}\right\} \end{aligned} \tag{6.170}$$

The approximation came from integrating to infinity instead of a which is reasonable if diffraction losses are small on the substrate. Plugging in the equation 6.168 and $I(r)$ into the remaining boundary conditions,

$$\left[k_n - \frac{4\sigma_B T_0^3}{\kappa}\right] e^{-k_n h} A_n - \left[k_n + \frac{4\sigma_B T_0^3}{\kappa}\right] B_n = \frac{\epsilon p_n}{\kappa} e^{-k_n h/2} \tag{6.171a}$$

$$\left[k_n + \frac{4\sigma_B T_0^3}{\kappa}\right] A_n - \left[k_n - \frac{4\sigma_B T_0^3}{\kappa}\right] B_n e^{-k_n h} = 0 \tag{6.171b}$$

Solving for A_n and B_n,

$$A_n = \frac{\epsilon_a p_n}{\kappa} e^{-3k_n h/2} \frac{\eta_+}{\eta_+ - \eta_- e^{-2k_n h}} \tag{6.172a}$$

$$B_n = \frac{\epsilon_a p_n}{\kappa} e^{-k_n h/2} \frac{\eta_-}{\eta_+ - \eta_- e^{-2k_n h}} \tag{6.172b}$$

where $\eta_\pm = k_n \pm \frac{4\sigma_B T_0^3}{\kappa}$ is used for brevity. Now it is possible to write down the entire steady-state temperature field for a cylindrical test mass with a laser beam impinging on the surface,

$$T_p(r,z) = \sum_{n=0}^{\infty} \frac{\epsilon_a p_n}{\kappa} \frac{\eta_- e^{-k_n(3h/2 - z)} + \eta_+ e^{-k_n(h/2 - z)}}{\eta_+ - \eta_- e^{-2k_n h}} J_0(k_n r) \tag{6.173}$$

Once the temperature profile is solved, the path length distortion from the thermo-refractive effect can be found by solving by equation 6.156,

$$Z_{\mathrm{TR}}(r) = \frac{\mathrm{d}n}{\mathrm{d}t}\frac{\epsilon_a}{\kappa}\sum_{n=0}^{\infty}\frac{p_n}{k_n}\frac{1-e^{-k_n h}}{[\eta_+ - \eta_- e^{-k_n h}]}\,J_0(k_n r) \tag{6.174}$$

where p_n contains information about the heating profile so it is possible to directly plug in equation 6.170 to represent the distortion from a Gaussian beam,

$$Z^G_{\mathrm{TR}}(r) = \frac{\mathrm{d}n}{\mathrm{d}t}\frac{\epsilon_a P}{2\pi a^2\kappa}\sum_{n=0}^{\infty}\frac{N_n}{k_n}\,e^{-(k_n w)^2/8}\,\frac{1-e^{-k_n h}}{[\eta_+ - \eta_- e^{-k_n h}]}\,J_0(k_n r) \tag{6.175}$$

The thermo-refractive effect due to coating and substrate absorption is only one type, there is also an effect which elastically curves the surface from thermal expansion [87]. This thermo-elastic effect deals with the internal stresses of the material and employs the stress-strain relations in order to derive the wavefront curvature. For the LIGO test masses which use fused silica, this effect is smaller than the thermo-refractive wavefront distortion by about an order of magnitude.

6.3 Contrast Defect

Generally, the contrast defect is defined as the ratio of the darkest to the brightest power at a given point in the interferometer, which in practice is the ratio of power at the antisymmetric and reflected port when locked on a dark fringe. In other words, it is the amount of junk light that is present in the interferometer when light between the two arms do not perfectly interfere with each other. This junk light can be the symptom of various causes, for example, an imbalance of reflectivity between ITMX and ITMY will cause non-perfect destructive interference at the antisymmetric port and a camera would see a TEM00 beam when locked on length. Another cause of contrast defect could be from misalignment between the ITMs or beamsplitter which will result in seeing a TEM 01/10 mode. However, if both of the aforementioned causes are fixed with a combination of stringent design specifications for the reflectivity and alignment loops closed to minimize angular jitter, then the contrast defect will be dominated by mode mismatch which can be fixed by a combination of ring heaters and CO_2 lasers. The picture gets even more complicated when adding in the

absorption for individual optics and introducing multiple Fabry-Perot cavities which will treat the sidebands and carrier fields differently.

One of the main goals for the Thermal Compensation System is to correct the cold and hot interferometer differences in radii of curvature.

6.3.1 Simple Michelson Contrast Defect

The simple Michelson can give a first estimate of the contrast defect when starting to commission the interferometer's thermal system, however, it is not used in nominal low noise since the dual-recycled Michelson is implemented. By propagating the input mode cleaner beam to the beamsplitter and taking a single bounce at the high reflectivity surface, one can approximate the resultant mode overlap by measuring the power at the antisymmetric port. The static mismatch correction was measured this way and is compensated using one of the CO_2 lasers to reduce the contrast at 2 Watts of input power from 0.4% to 0.1%.

At this point the carrier and sideband fields follow the same ABCD matrix transfer function, so only one calculation is needed to estimate the contrast defect. A keen reader will notice that this model will not take the Schnupp asymmetry into account which allows the $\hat{x}$-direction beam to travel an extra 8 centimeters further than the $\hat{y}$, however, this effect will only change the end result by approximately 10%. In fact, for this interferometer configuration, the dominate source of mismatch will be from the prompt reflection off the HR surfaces of the ITMs where most of the phase change occurs. The sideband contribution at the antisymmetric port can be estimated by using equation 2.24 and measuring the modulation depth, Γ_Ω, for the 9 and 45 MHz RF fields that enter the interferometer,

$$\begin{aligned} P_{\mathrm{SB}} &= 2P_{\mathrm{in}}\left(\frac{\Gamma}{2}\right)^2 t_{SB\pm} \\ &= 2P_{\mathrm{in}}\left(\frac{\Gamma}{2}\right)^2 \sin^2(k_\Omega \Delta\ell) \end{aligned} \tag{6.176}$$

Additionally, the beamsplitter RMS motion will also contribute extra power at the AS and can be estimated by calculating the coupling coefficient from the 00 to 01 HG

mode,

$$P_{01} = 2P_{\text{in}}\left(\frac{\pi\,\alpha\,w(z)}{\lambda}\right)^2 \tag{6.177}$$

where $w(z)$ is the beam size on the test mass and α is the misalignment RMS.

6.3.2 Modal Contrast Defect

During full lock, the formalism must be extended to include the mode shape of two arm cavities interfering at the beamsplitter. Using the Laguerre-Gauss modes is useful for brevity because the mode mismatch couples to only one higher order mode. Contrast defect can be defined using the zeroth eigenmode of each arm and then expanded to project the X-arm's basis onto Y-arm using higher order LG modes, $LG_y^{00} \rightarrow LG_x^{00} + \alpha LG_x^{10}$. Where $\alpha = \frac{1}{\sqrt{2}}\left(\frac{\Delta\omega_0}{\omega_0} + i\frac{\Delta z}{z_R}\right)$ is the amount of higher order mode coupling due to mismatch in beam size and location, respectively (see Chapter 3).

$$\begin{aligned}
\text{CD} &\equiv \frac{P_{AS}}{P_{REFL}} \\
&= \frac{|LG_x^{00} - LG_y^{00}|^2}{|LG_x^{00} + LG_y^{00}|^2} \\
&= \frac{|LG_x^{00}|^2 + |LG_x^{00} + \alpha LG_x^{10}|^2 - 2\,\text{Re}(LG_x^{00}[LG_x^{00*} + \alpha LG_x^{10}])}{|LG_x^{00}|^2 + |LG_x^{00} + \alpha LG_x^{10}|^2 + 2\,\text{Re}(LG_x^{00}[LG_x^{00*} + \alpha LG_x^{10}])} \\
&\approx \frac{\alpha^2}{4} \\
&\approx \frac{1}{8}\left[\left(\frac{\Delta\omega_0}{\omega_0}\right)^2 + \left(\frac{\Delta z}{z_R}\right)^2\right]
\end{aligned} \tag{6.178}$$

Mismatch between the arm cavities can stem from a few sources such as the difference between the radii of curvature on the high reflectivity surfaces that will cause the resonant modes to be shaped differently between the X-arm and Y-arm. LIGO tries to optimize this effect by pairing the optics based on their properties, however, during the upgrades from O2 to O3 at Hanford, ITMX was replaced but ITMY was not which lead to a static mismatch between the input test masses.

6.4 Tuning Thermal Compensation for LIGO

As mentioned in Section 6.1.1, the circulating power in each of the arms can be close to 150 kW for O3 and will be higher for the subsequent observation runs. Even with absorption only in the range of $0.2 - 0.8$ parts per million, the induced substrate lensing can be significant. The Thermal Compensation System (TCS) [62] [17] [91] [84] was developed to correct the wavefront by applying heat to cancel the deformities caused by interferometer heating. Ease of lock acquisition and gravitational-wave noise minimization are the main criteria for success when commissioning most LIGO systems. To aid in the former, TCS is required to thermally lens the ITM substrate such that the optical path difference is minimized for the carrier and sideband power recycling gains.

To optimize the TCS settings for the best power build-ups, there are two separate strategies: The first requires estimating the amount of absorption on the test masses with the Hartmann Wavefront Sensors to measure the optical path distortion induced by the interferometer during a lock loss. Then pre-load the ring heaters with the nominal settings which would cancel carrier beam's thermal absorption in the "hot" state. The ring heaters have a very long time constant (30 hours) to reach thermal equilibrium with a step response of electrical power, so if there is compensation needed, the heaters must be energized at all times. However, turning them on will change the radius of curvature and induce a substrate lens (see Section 6.4.2) that has to be canceled out by the CO_2 (Carbon Dioxide) lasers which create a lens on the compensation plate of the quadruple pendulum. Since the CO_2 lasers have a time constant of approximately 0.5 hours, they can be turned up during lock acquisition and reduced as needed when the interferometer input power is increased.

The second method is to use relevant interferometer RF signals at various ports to experimentally adjust the lensing commonly or differentially to maintain power recycling build-ups while increasing the interferometer input power. In principle, either method should lead to the same answer but in practice, both are used to find the nominal thermal compensation configuration. The section below describes how to tune the Hartmann Sensors and how the system can be used to determine the uniform absorption.

6.4.1 Hartmann Wavefront Sensors

All estimates of steady-state curvature changes due to heating by the main interferometer beam depend linearly on the absorption. This can be quite difficult to detect when the coating absorption are typically less than one part in a million.

In order to diagnose this effect, the Hartmann Wavefront Sensors (HWS) [13] [85] was developed by Adelaide and Caltech [15] [16]. It uses an auxiliary beams and charged-coupled imaging devices (CCD) to sense the wavefront distortions formed by heating from the interferometer beam during power up and a lock loss. Currently, there are four Hartmann sensors installed at each test mass, which are injected from the AR surface side of the optics. Technical constraints require the ITM HWSs optical paths to differ from the ETM HWSs but the concept is still the same, so for brevity, only the ITMs HWSs will be discussed in detail. In Figure 36, the system starts with an auxiliary super-luminous LED (SLED) beam being injected into the vacuum system and a telescope (Lens 1, Lens 2) which collimates/expands the beam to sample a space 200 mm in diameter on the test mass HR surface. The return beams are picked-off and sent to a CCD with a Hartmann plate mounted on the front which effectively decompose the wavefront into individual rays. Using a wavefront from a previous time with a cold optic as a reference. The Hartmann code creates a gradient vector field between the two times which have information about thermal lensing. Then numerically integrates the gradients to fit a wavefront field which is normally referred to as the optical path distortion in length units. The algorithm then uses the Zernike polynomials as a single basis to represent the effective thermal lens. [14]

Tuning the Hartmann Sensors

It was found that the CCDs (Dalsa pantera 1m60) had a number of hot pixels, which would create large spikes in their intensity counts and these produce large artifacts in the gradient plots that corrupted the spherical lens fitting (see Figure 38). One of the requirements for the HWSs is a wavefront distortion resolution of 1.35 nm [17] and a single hot pixel could register a few orders of magnitude higher. A solution for this was implemented by using the dark images to locate the bad pixels by averaging the counts over a few minutes and finding all the pixels which have counts higher

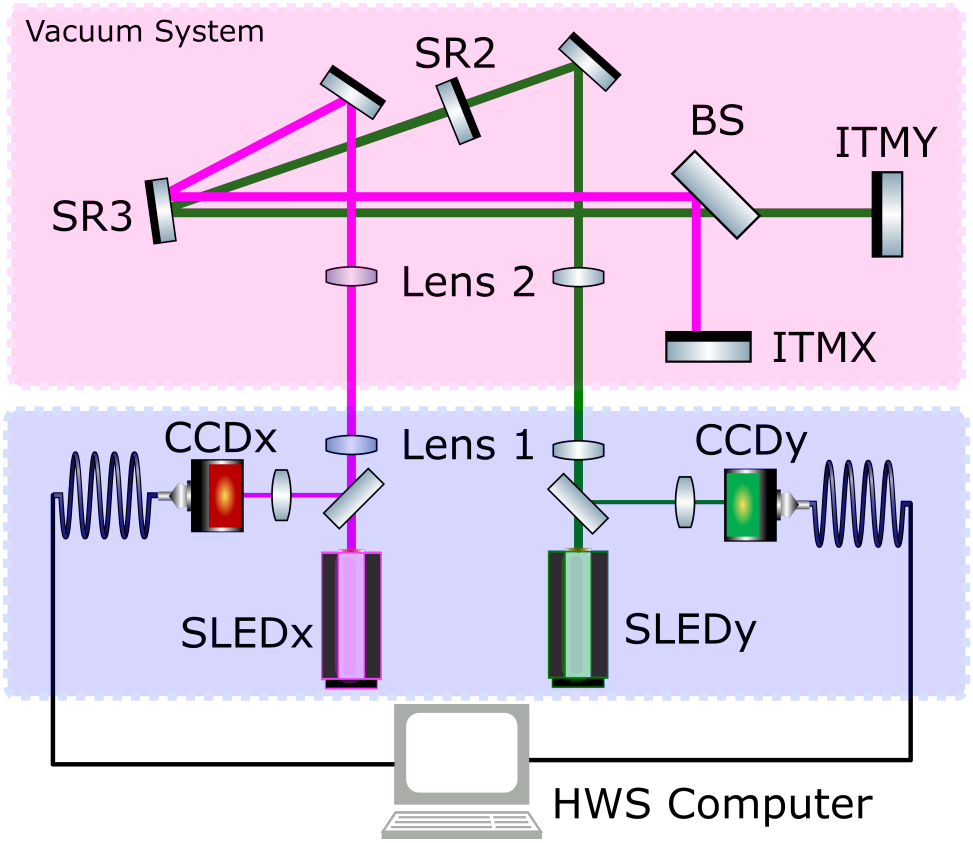

Figure 36 : **ITM Hartmann sensors optical layout.** The path for injection is different for the two Hartmann sensors which use separate wavelengths to take advantage of the main beamsplitter AR/HR surface reflectivity. The ITMX (magenta) and ITMY (green) probe beam wavelengths are 800 nm and 833 nm, respectively, and have a 40 nm linewidth [17]. The beams are sent into the vacuum system and retro-reflected off their respective optics back towards the pick-off mirrors before going into the CCDs with a Hartmann plate attached. The cameras are then sent via fiber to a computer that runs the analysis pipeline on the images and exports the data to EPICS so the users can interface with the real time digital system in the control rooms.

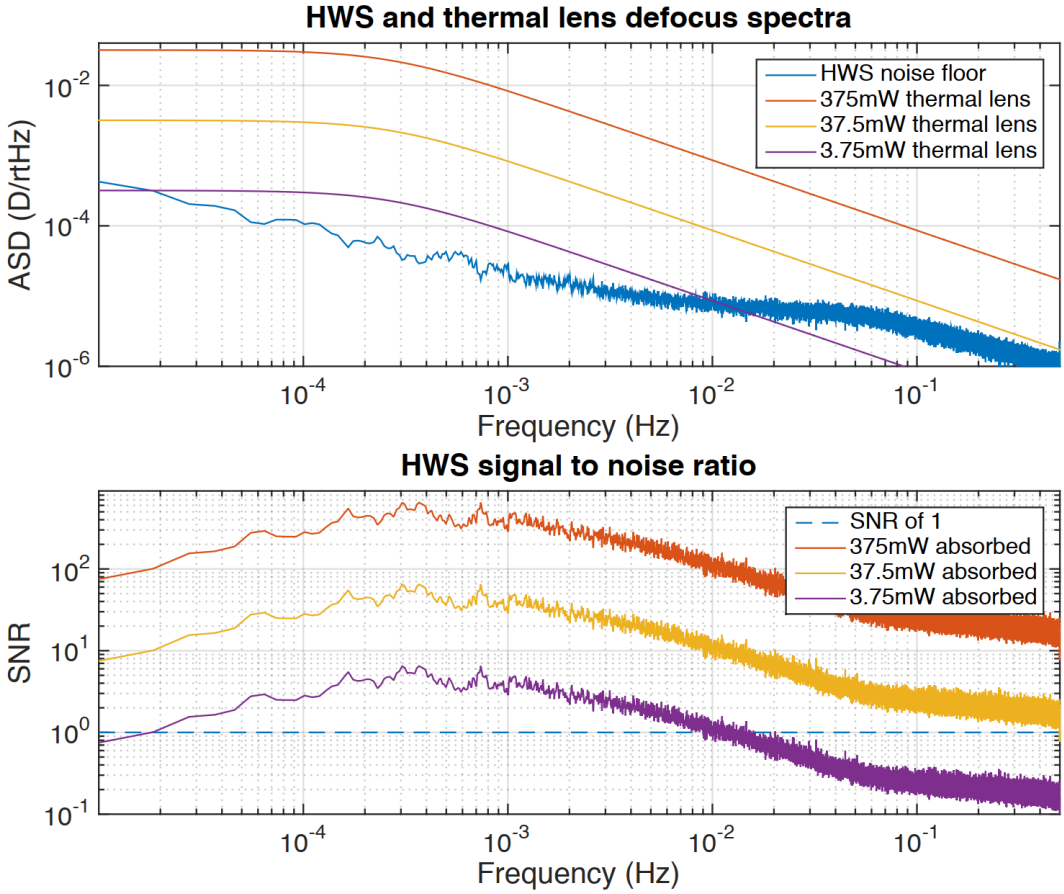

Figure 37 : **Noise spectra for the HWS spherical lensing.** Taken from [17], this puts a lower bound on the Hartmann sensitivity to distortions for various time scales.

than a particular threshold, generally 1.5 times above the average ambient dark noise level (about 50 counts). The dark frames would be read in by the Hartmann code, which uses the dark images as a reference to find the average of surrounding pixels and replace the problematic pixel. This digital procedure greatly reduced the impact of hot pixels in the Hartmann sensor data.

Another source of systematic error was from beam clipping along the in-vacuum beam path on the ITMX HWS, see Figure 39. This creates diffraction fringes which are extremely sensitive to misalignment; one fix that was applied to reduce this noise was to digitally mask the fringes so they do not confuse the fitting algorithms. Hand tuning must be done so that the mask is wide enough and centered around the interferometer lensing but not so large that the Hartmann fitting is corrupted by the fringes. Two in-air periscope mirrors with pico-motors were used for alignment, but beam clipping could not be fully removed. This artifact was also found at LLO so it suggests a design flaw in the initial alignment scheme. A possible fix could be implemented by replacing an in-vacuum steering mirror with a pico-motor that could be aligned remotely.

When increasing the input power into the interferometer, there were large spikes associated with the spherical power estimation on the ITMX corresponding to time scales of less than a second which is not likely due to lensing from uniform absorption. This was eventually tracked down to a leakage beam caused by stray light from the interferometer. At times, the leakage beam was 40% the intensity of the main Hartmann beam which severely distorted the fitting algorithms. ITMY HWS did not see this effect because SR2 is such a good high reflector and attenuated any 1064 nm contributions down to the ppm level.

Measuring Uniform Absorption

After the arm power drops suddenly, the lensing decays exponentially at a rate that depends on the amount of absorption on the high reflective surfaces of the arm cavity. Using the HWS, it is possible to fit the decay rate to a finite element model of a cylindrical mass in order to solve for a single uniform absorption estimate. It is extremely important to have reliable measurements to aid in pre-determining the amount compensation necessary to prepare the test masses for lock acquisition.

Figure 43 shows the measured spherical power from interferometer heating for

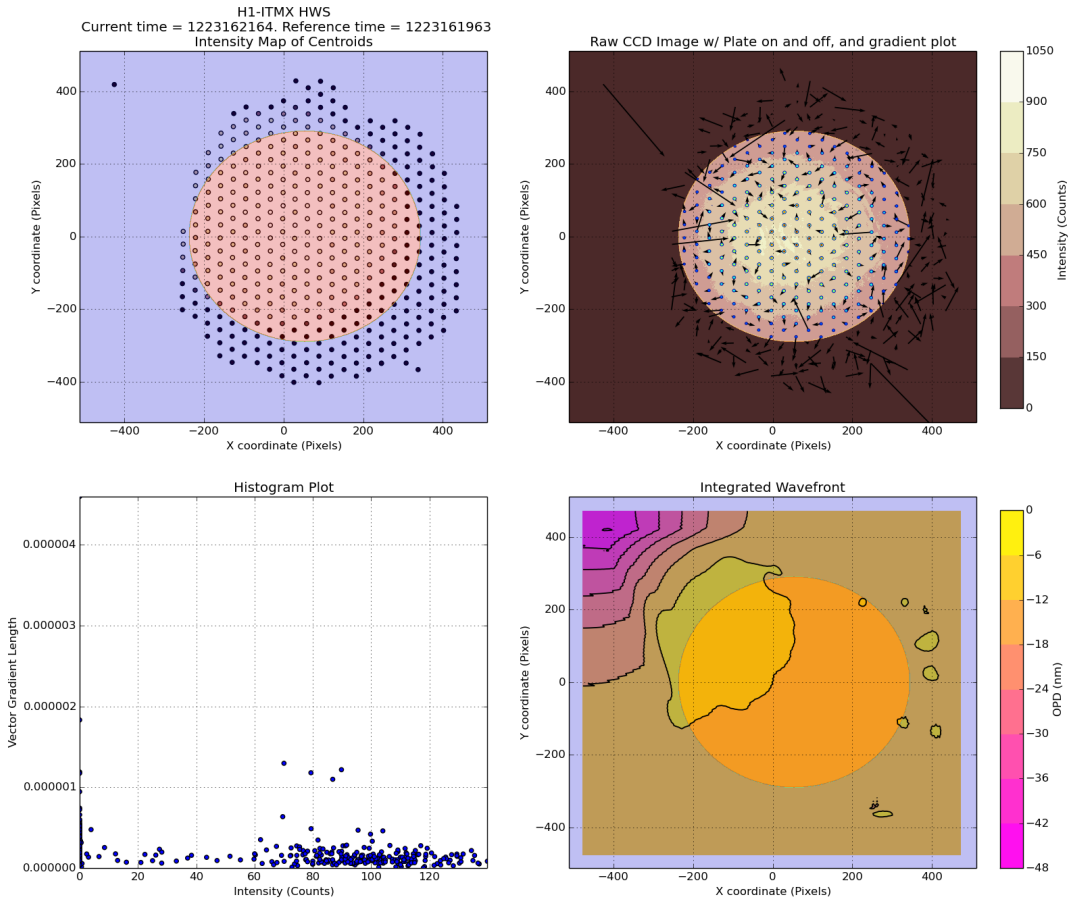

Figure 38 : **ITMX Hartmann Sensor output.** Between the reference and current times for this measurement, no heating was applied to the test masses so the expectation is a relatively flat and smooth wavefront. This is mostly true except for a large, anomalous arrow at pixel coordinate [X,Y] = [-410, 405] of the gradient plots (upper right) which leads to a false wavefront distortion in the same area for the contour plot (lower right). The sharp iris in the middle represents a digital mask that is can be turned on to reduce the effects of fringing. A histogram in the bottom left plot shows the intensity distribution for each of the gradients; if the HWS beams are co-aligned well with the interferometer beam, then most of the information about thermal lensing occurs near the center of the intensity distribution.

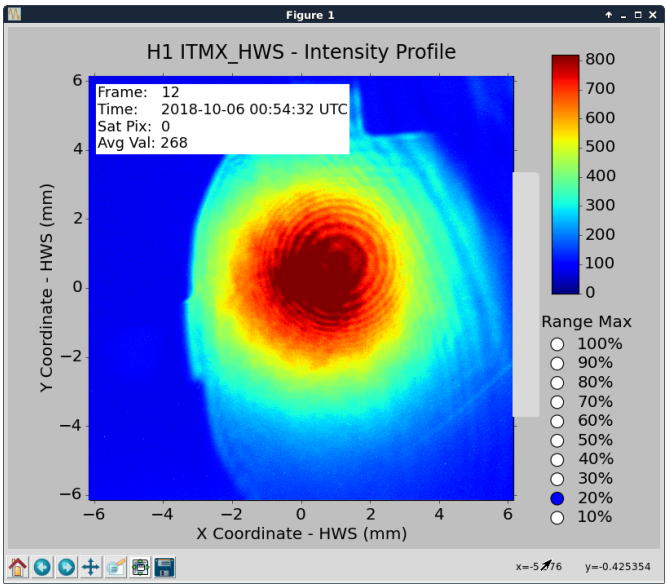

Figure 39 : **Clipping on ITMX Hartmann Sensor.** A source of systematic error found at both sites when trying to simultaneously align ITMX and ITMY Hartmann Sensors. The CCD spot positions are very sensitive to the SR3 alignment so control loops and initial alignment are not recommended for this particular optic. An in-vacuum pico-motor may help alleviate the clipping.

ITMX/ITMY and comparing the two optics shows that the spherical power difference for ITMY is almost a factor of 2 larger than ITMX. Applying an Markov Chain Monte-Carlo method allows some statistical uncertainty estimates for the exponential fitting to the data shown in Figure 44, where the priors are assumed to be random Gaussian noise and the initial guesses are scaled roughly with a least squares fitting algorithm. One of the main differences between the O2 and O3 observing runs was the replacement of ITMX, ETMX, and ETMY test masses. With a fully running Hartmann Sensor system in place which monitors the wavefront curvature across the optic, long-term trends over the observation runs will be able to determine how absorption changes as a function of time and whether test masses have an innate lifetime. This will be particularly important if the next generation of detectors use much higher power levels in order to achieve better high frequency sensitivity [18]. Using this method, the current absorption estimates for the H1 input test masses are as follows:

$$\begin{aligned} A_{\mathrm{ITMX}} &= 328 \pm 84 \text{ ppb} \\ A_{\mathrm{ITMY}} &= 688 \pm 85 \text{ ppb} \end{aligned} \tag{6.179}$$

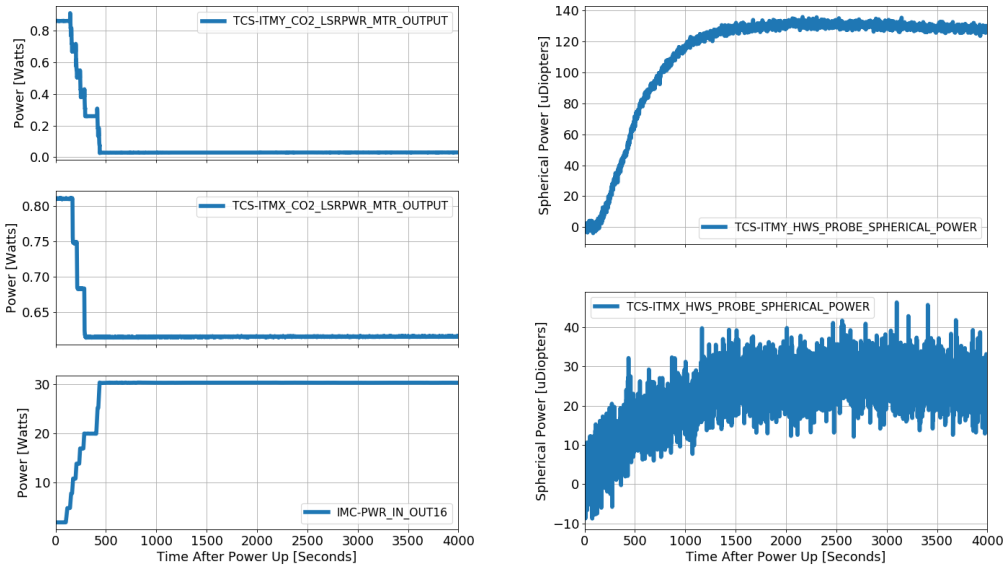

Figure 40 : **A time series of the interferometer power increase sequence.** During this time, the interferometer is using DC-readout and locked at 2 watts of PSL input power with all of the angular control loops closed with high-bandwidth, in this configuration, the power recycling gain is approximately 45. The left figure shows the increase of PSL input power (bottom) and the CO_2 lasers (top two) stepping down in power where levels of compensation were experimentally determined such that the angular control loops were stable and sideband build ups remained as high as possible. The right plot shows the Hartmann sensor spherical power as a function of time with the starting point scaled to zero micro-diopters for ITMX and ITMY. Although the point absorbers do not exhibit the same spatial structure as uniform heating so it is difficult to derive absolute absorption for ITMY, the spherical fitting gives some information about the relative scale of heating absorption between the two optics.

6.4.2 Ring Heater and CO_2 Laser Commissioning

To counteract the effects of interferometer heating, Advanced LIGO uses a ring heater [75] [88] which has two heating elements mounted on the suspension cage. Each of them are comprised of a semi-circular glass cylinder that is wrapped by nichrome wire, which has current running through the wire to radiate an annular heating pattern. The ring heaters will have two effects: it will induce a substrate lens and a radius of curvature change. As shown in Section 6.1, the carrier beam will not see the substrate lens but the radius of curvature difference will change the overall modal shape of the cavity. Similar to the distortion derived in section 6.2 where the thermo-refractive

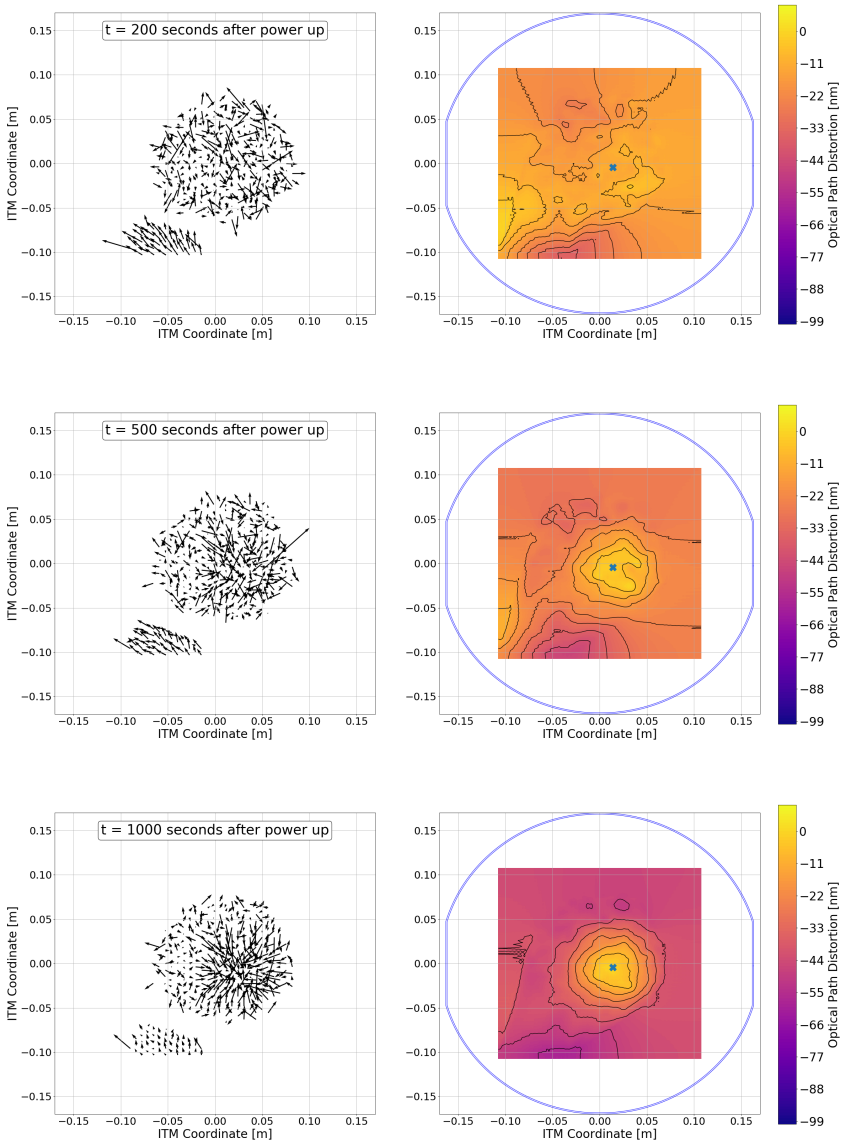

Figure 41 : **ITMX gradient plots (left) and wavefront maps (right) during a power up to 30 Watts of input power.** It is important to note that there is a back-reflected stray beam from the super-luminous LED that is incident in the bottom left portion of the camera which is digitally cropped out during the real-time analysis. As previously noted, this particular Hartmann sensors suffers from beam clipping on the right side of the image which adds to the systematic noise. A blue cross denotes the origin which is fitted with the Zernike polynomials to derive a spherical power. The arrow lengths in the gradient plots are normalized to each individual plot and are meant to guide the eye in discerning the directionality and pattern of lensing.

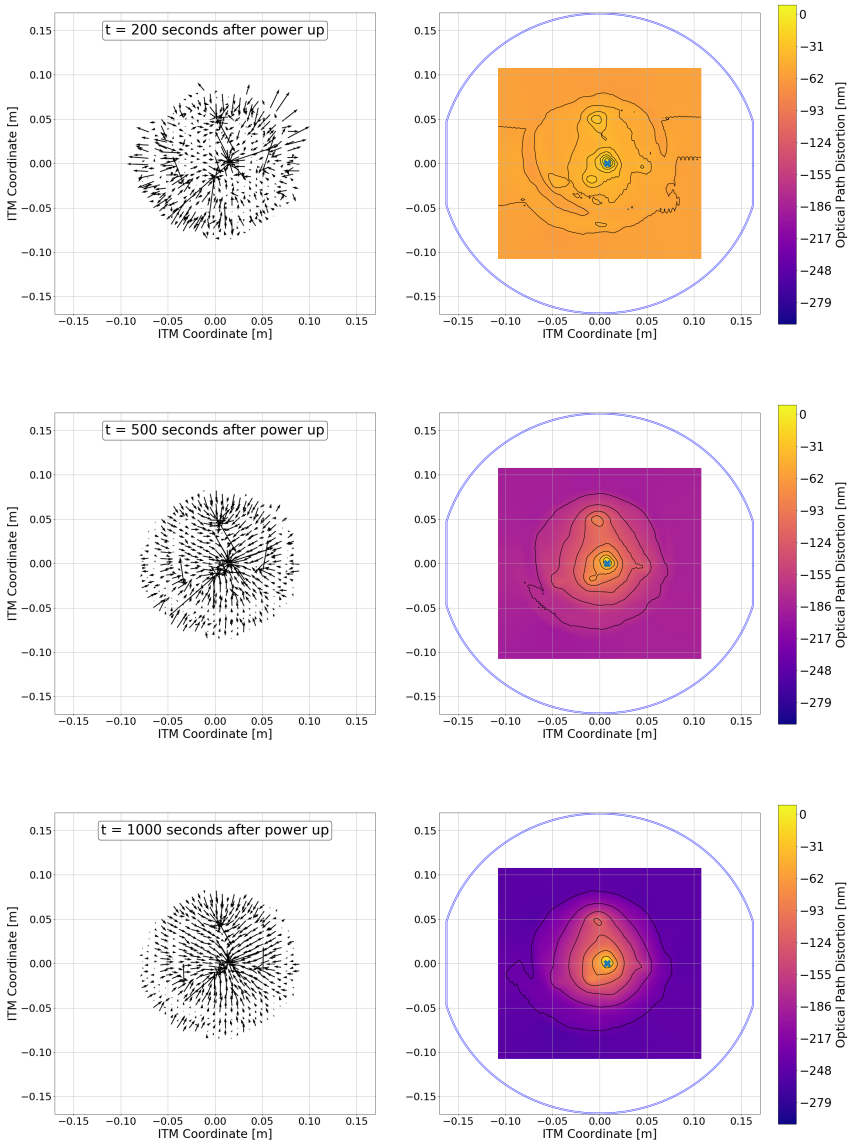

Figure 42 : **ITMY gradient plots (left) and wavefront maps (right) during a power up to 30 Watts of input power.** Compared to the ITMX phase map in Figure 41, ITMY has a much larger overall heating pattern and higher spatial frequencies in the contours which was the first clue that revealed multiple (possibly 4) point absorber on the test mass. There is also a halo of gradients on the outer rim of the plots which is most prominent on the lower left corner. This is due reducing the CO_2 laser power in an attempt to compensate the lensing effects as the interferometer beam heats up the test mass. The overall scale of self-heating with the higher spatial frequencies of the point absorbers makes it very difficult to compensate with using the CO_2 lasers as designed by Advanced LIGO.

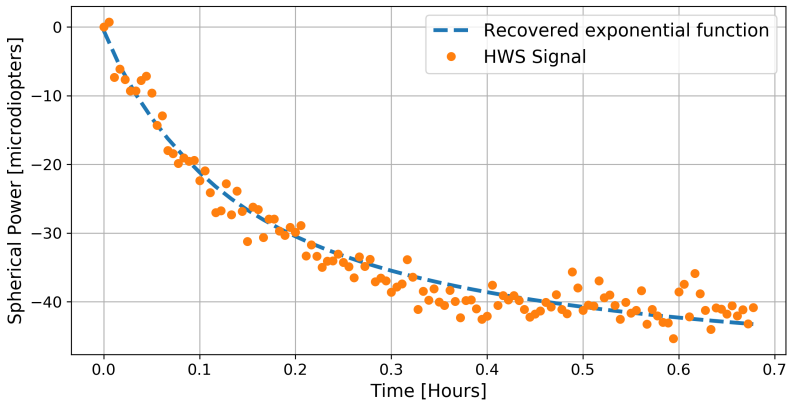

(a) ITMX absorption

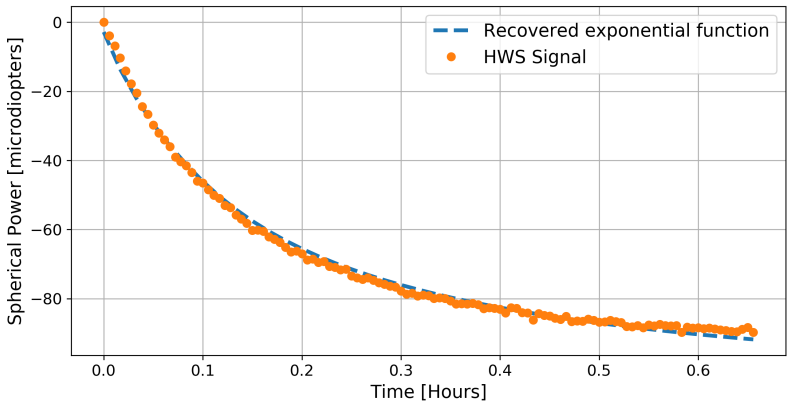

(b) ITMY absorption

Figure 43 : **Thermal lensing as seen by the ITM Hartmann Sensors after a lock loss.** A finite element simulation from COMSOL shows an impulse response which resembles an exponential decay can be linearized and fitted to the spherical power. The model assumes a beam size of 54 mm and 1 Watt of uniformly absorbed power then uses MCMC to fit the offset and scale to the data. Comparing ITMX and ITMY at Hanford shows a huge overall difference between the two optics, mostly due to the fact that ITMY has multiple point absorbers adding to the absorption estimate. In addition, fitting ITMY data points with the model does not seem to agree very well which indicates extra physics that stems from non-uniform heating by a 54 mm beam.

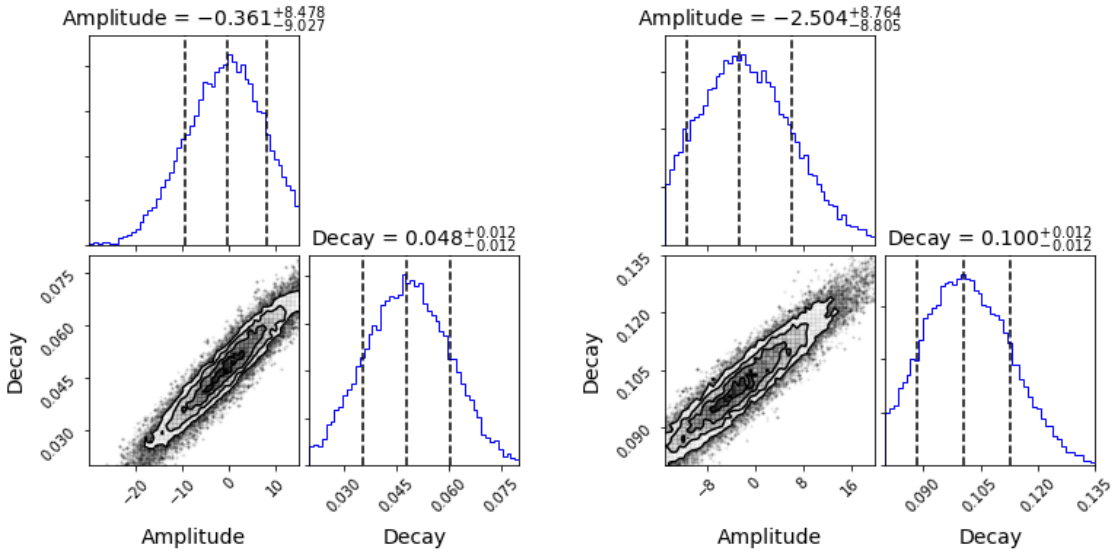

(a) ITMX (b) ITMY

Figure 44 : **Posterior distributions from fitting the Hartmann sensor spherical power.** Using the MCMC Hammer [44] to fit the finite element model from Figure 43, the two open parameters to solve for the decaying exponential is the amplitude and the decay rate which is related to the level of uniform absorption.

effect dominates when dealing with a Gaussian beam, the same is true from the ring heaters.

After using the Hartmann sensors to determine the absorption and pre-loading the ring heaters to compensate the interferometer lensing, the fact that the substrate is cold makes lock acquisition difficult. Therefore, it is necessary to use CO_2 (Carbon Dioxide) lasers to mimic the interferometer's heating by delivering heat to the compensation plate. The CO_2 lasers are located on each input test mass chamber and injected through a double zinc selenide viewport, then two steering mirrors direct the heating beam to the compensation plate of the reaction mass. In initial LIGO, the CO_2 beams were injected onto the high reflectivity surfaces of the test masses which created both a radius of curvature on the cavity side and a thermo-refractive change in the substrate. However, in advanced LIGO, the CO_2 lasers will only affect the substrate lensing. Tuning the CO_2 power will have a dramatic effect on the interferometer auxiliary degrees of freedom because the sidebands get rejected by the arm cavity and only resonate in the recycling cavities. The self-heating caused by

	Substrate	HR surface	Compensation Plate
Self Heating	*4.9e-4	*-3.6e-5	N/A
Ring Heater	-9.0e-6	*9.9e-7	N/A
CO_2x	N/A	N/A	1.5e-5
CO_2y	N/A	N/A	2.5e-5

Table 5 : **Single pass actuator lensing calibrations for aLIGO TCS in micro-diopters/Watt.** The asterisks indicate the values are extracted from a model and the measured values use the Hartmann sensors which cannot distinguish between surface and substrate lensing, however, the latter is larger by an order of magnitude. CO_2x and CO_2y were measured to be different in their actuation strength which could stem from either misalignment or a misplaced central mask. The uncertainty is expressed by the last digit available.

the interferometer beam is assumed to have a Gaussian intensity profile, while the CO_2 heating beam is meant to have a uniform profile across the test mass surface which allows for a consistent phase distortion as a beam passes through the substrate. Settings for the ITM ring heaters and CO_2 lasers are calculated in Figure 45 based off the Hartmann measurements. Adding the effect of pre-loading will inherently change the Gaussian mode overlap between the x-arm and y-arm. Using equation D.221, one can directly calculate the power overlap between a pre-loaded cavity and the original, as it turns out, the effect varies the overlap by less than 0.1% so the addition of ring heater power for O3 will not change the modal contrast defect by much.

Determining the ITM ring heaters and CO_2 power levels still leaves the end test mass ring heaters to be set. In Figure 46, the goal is to maintain the mode matching between the arms while simultaneously searching for the optimal overlap with the power recycling cavity. This is done by determining the spatial mode overlap between all three cavities (XARM, YARM, and PRC). The linear portion of the graph shows a combination of common and differential adjustment of each ETM ring heater that keeps the mode matching between the arms at less than 1 ppm by calculating the Gaussian beam overlap. Once that region is found where both arms are well mode matched, sampling the ara where there is maximal mode overlap with the power recycling cavity can be determined and is shown with contour plots.

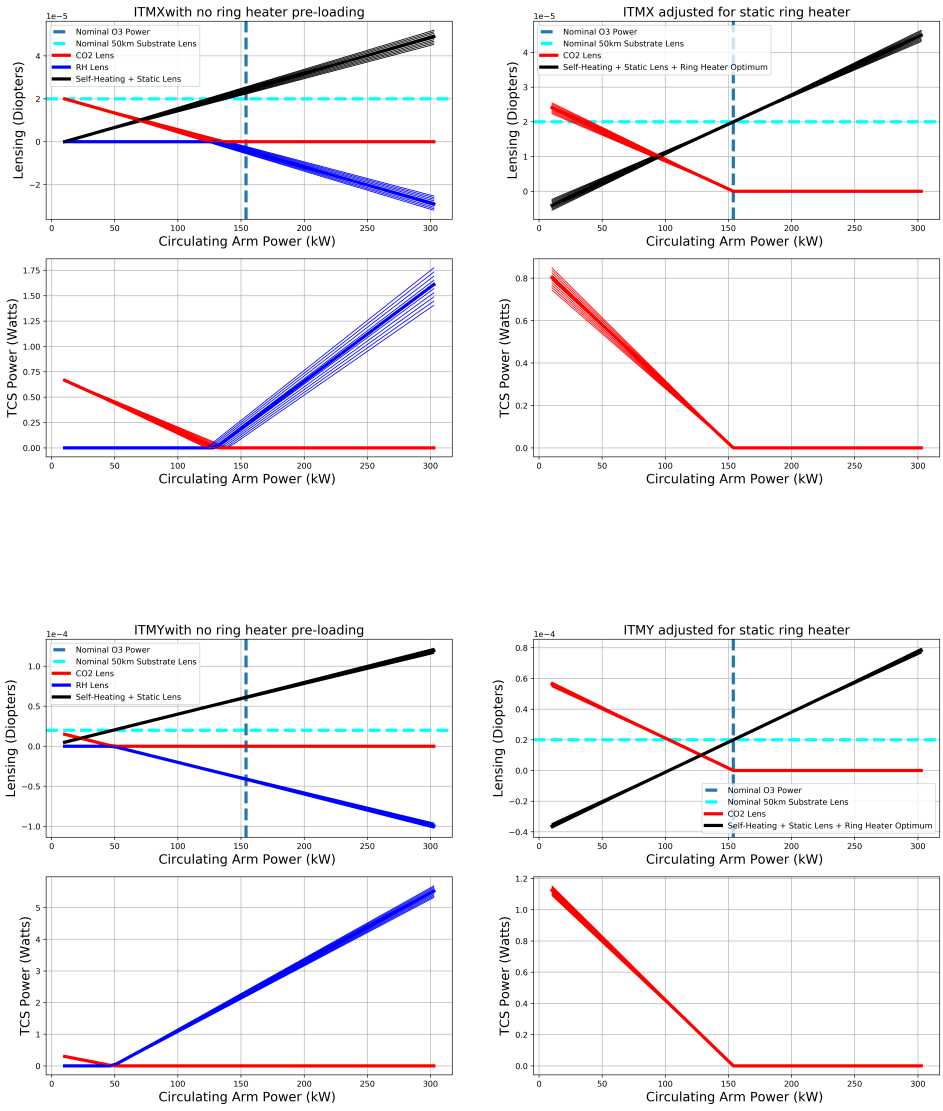

Figure 45 : **Calculated TCS settings to balance the substrate lens.** The nominal circulating power denoted by the vertical blue line is a function of the input power, the recycling gain, and the arm cavity gain. The nominal input power for O3 will be 50 Watts and the power recycling gain is around 45. The arm cavity gain can be estimated by calibrating the transmitted power from each of the arms and is approximately 228. The horizontal, dashed turquoise line represents the nominal substrate lens with a focal length of 50 km. The total substrate thermal lensing from ring heaters, CO_2 lasers, and interferometer heating should sum up to the turquoise line. The left column of graphs show the necessary ring heater and CO_2 laser powers required to compensate the interferometer heating. The left column of graphs show the required CO_2 power if the ring heaters are constantly energized during lock acquisition because their thermal time constants are on the order of a few hours. The spread in the estimates stem from uncertainty in the uniform absorption which is crucial in determining the correct TCS settings

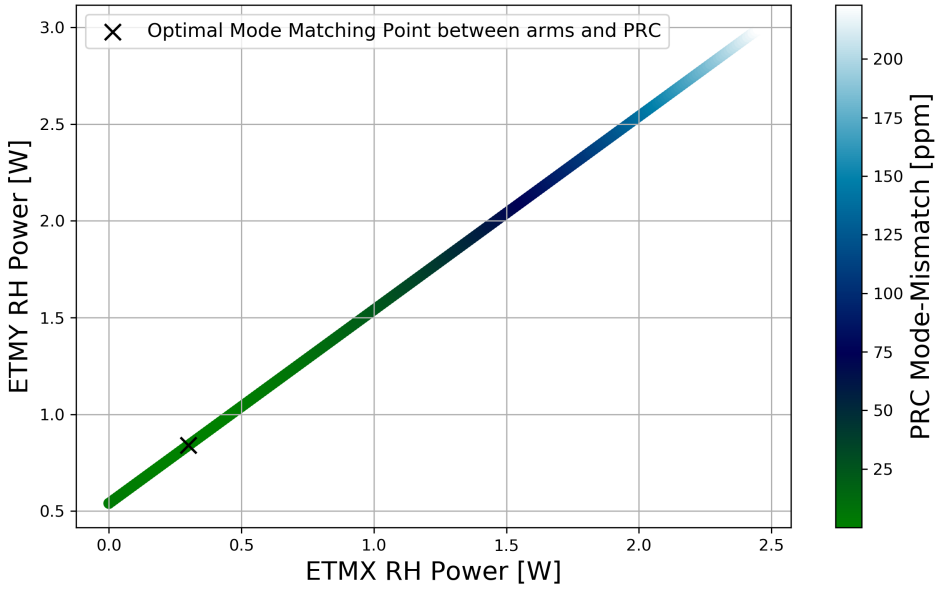

Figure 46 : **Mode matching the arm cavities to the power recycling cavity.**

6.5 Point Absorbers

Up till now, all actuators models, and measurements assumed uniform absorption across the optics which results in second order Hermite-Gauss coupling with the fundamental Gaussian beam . As it turns out, the instrument is not so simple. One of the main successes for the Hartmann Wavefront Sensors have been the ability to find excess absorption due to point absorbers on the high reflectivity surfaces of the test masses. During the second observation run (O2), there was an absorber found on ITMX that made increasing the input power past 30 watts extremely difficult and futile because of increased coupling intensity noise into DARM. The exact origin of these point absorbers is still an active area of research but incursions into the vacuum system will always pose a risk of spreading particulate on the HR surfaces.

Part way into commissioning for O3, another point absorber on ITMY was detected that showed similar characteristics. Since their spatial frequencies are much higher than the uniform absorption, many of the models for scattered power and thermal effects require significant adjustment to predict the interferometer behavior. To decompose the differential phase map into the Hermite Gauss basis requires a relatively high order and makes full interferometer simulations very difficult. For example, FINESSE calculations on a laptop tend to become unwieldy at around $n+m=6$. The high spatial frequency of point absorbers affects the HWS's ability to properly evaluate a singular thermal lens from the interferometer, therefore changing the estimated absorption.

A way to separate the point absorber effect from uniform absorption could be considering the temporal effects which quadratically depend on the point absorber size. The thermo-refractive transient solution found in Vinet [87] has the form

$$Z_{\mathrm{TR}}(t) \propto 1 - \exp\{-t/\tau\} \tag{6.180}$$

where $\tau = \frac{\rho C w_{\mathrm{pa}}^2}{3\kappa}$ is the characteristic time constant that depends on the beam size w_{pa}, the thermal conductivity κ, the specific heat C and the material density ρ. A simple model can consist of two beams with different sizes which will have separate time constants. Another interesting way of characterizing what can be compensated for O3 could be to Fourier transform the optical path distortion and low pass the high spatial frequency components with a Gaussian filter. The cut-off frequency can

be estimated by the approximate point absorber size (10-20 mm). Of course, early detection and replacement of an optic may be the most efficient way to avoid custom thermal compensation. Figure 47 shows a comparison between ITMX and ITMY while the interferometer is increasing input laser power from 2 to 30 Watts. Within the first few hundred seconds, the point absorbers begin showing up in the optical path distortion map.

There are two main parts which allow point absorbers to adversely affect interferometer performance. The first is scattering from the arm cavity that takes away carrier light and couples to higher order modes, and secondly, the thermal lens in the substrate distorts the power recycling cavity for the sideband build ups dramatically.

An interesting coupling that was discovered which the point absorbers could be responsible for is higher order mode 9 Mhz leakage through the OMC. Generally, the OMC is very good at rejecting both the sidebands and first few higher order modes but the addition of point absorbers couples greater spatial frequencies than anticipated. Careful analysis by Koji Arai [6] shows the Hanford OMC can allow some 9th order Hermite Gauss modes from the 9 MHz sidebands onto the OMC DCPDs. This coupling should provide a decent metric for indicating the point absorber's induced noise on the interferometer.

During commissioning periods, the highest starting priority is to achieve full resonance as quickly as possible, and that is easier to accomplish using approximately 2 W of input laser power. This requires locking the arm length stabilization (ALS) system with 532 nm, the vertex degrees of freedom (DRMI) and complete the common arm length (CARM) transition. Additionally, closing all angular degrees of freedom (ASC) will take a lot of time and energy. If major upgrades or fixes have occurred such as replacing main test masses then all the prior steps require many months of commissioning. Generally, vacuum incursions into the main vertex cost the most time and money because of the large volume needing to be pumped. All this is to say: the earlier point absorbers are detected, the better. However, this requires a high level of arm power which historically has come much later on the road to nominal low noise. In Figure 37, the signal-to-noise ratio is 10 at 0.01 Hz for 37.5 mW of absorbed power which means the circulating arm power must reach at least 75 kW (assuming absorption is approximately 0.5 ppm) to be detectable within the time constant of point absorbers.

The power recycling gain for a single arm is described by

$$g_{\text{PRC'}} = \left| \frac{t_{\text{p}}}{1 - r_p r_{1\frac{1}{2}}} \right|^2 \approx 0.12 \tag{6.181}$$

where the factor of 0.5 comes from the main beamsplitter. This is much different than a gain of 45 for a full interferometer but it is still a factor of 4 larger than direct transmission through the PRM. So with a single power recycled arm cavity the expected circulating power absorbed on the HR surface of the test masses is

$$\begin{aligned} P_{\text{1-ARM}} &= P_{\text{in}} * g_{\text{ARM}} * g_{\text{PRC'}} * \epsilon_a \\ &\approx 0.94\ mW \left[\frac{P_{\text{in}}}{70\,\text{Watts}}\right] \left[\frac{g_{\text{ARM}}}{225}\right] \left[\frac{g_{\text{PRC'}}}{0.12}\right] \left[\frac{\epsilon_a}{0.5\,\text{ppm}}\right] \end{aligned} \tag{6.182}$$

where the coefficient ϵ_a is the estimated absorption from a point absorber. Using $D_{\text{sub}} \approx 487 \frac{\mu\text{D}}{1\,\text{Watt}}$ as the modeled conversion from absorbed power to steady-state spherical thermal lensing, the expected substrate lensing in units of micro-diopters [μD] is

$$S_{\text{1-ARM}} = P_{\text{1-ARM}} * D_{\text{sub}} \approx 0.46\ \mu\text{D} \tag{6.183}$$

which is not detectable by the current Hartmann sensors but the overall effect will be dependent on the absorption coefficient. Commissioning and installation schedules are ever-changing entities and there have been times when the end stations are not ready for integration simultaneously. This provides a window where only single arm commissioning is available so this method may be able to detect the existence of point absorbers much sooner.

Once these anomalies are found, the question remains, what can be done?

One consideration is a complete re-design of Thermal Compensation to account for higher frequency spatial corrections. There are already custom masks at Hanford which are designed to smooth the optical path distortion in the substrate and can be implemented with the CO_2 lasers on the compensation plate to increase the sideband build ups, which is one of the biggest difficulties associated with point absorbers. However, this does not solve the fundamental problem of losing power recycling gain due to power scattering where the quadratic losses of the arm cavity set an upper limit for increasing power. Another way to avoid these effects is to move the beam

spot away from the point absorber on the HR surface but it must be sufficiently far or the odd higher order modes will couple very strongly with asymmetry. These two strategies are not necessarily orthogonal since moving the spot position changes the required correction mask.

In terms of noise, the 9 MHz RIN coupling to the OMC DCPDs could be reduced by changing the OMC transverse mode spacing by locking on a different carrier resonance a free spectral range away. The introduction of a well-tuned custom mask should also reduce higher order mode content in the recycling cavities.

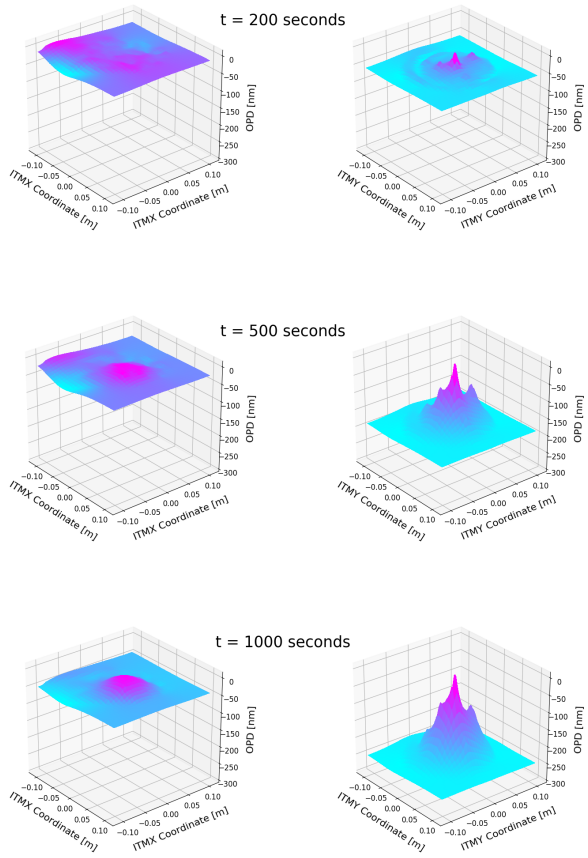

Figure 47 : **Comparing 3-D plots of the optical path distortion for ITMX and ITMY test masses after powering up the interferometer.** The horizontal axes represent the test mass coordinates as seen on the Hartmann sensors and the vertical axis is the optical path distortion in units of nanometers. The color map is scaled for each plot and is meant to show particularly hot areas and roughly compare the high frequency spatial distribution of point absorbers. Plots in the left column (ITMX) have smooth spatial features that stem from uniform absorption and the effects are not prominent till after approximately 500 seconds. In contrast, plots in the right column (ITMY) have very sharp spatial features which already rise above the floor at 200 seconds into powering up. Comparing the overall surface deformation on the same scale, the difference between ITMX and ITMY is striking and it is clear how an interferometer with point absorbers on the surface will struggle to increase powers above 200 kW within the arm cavities.

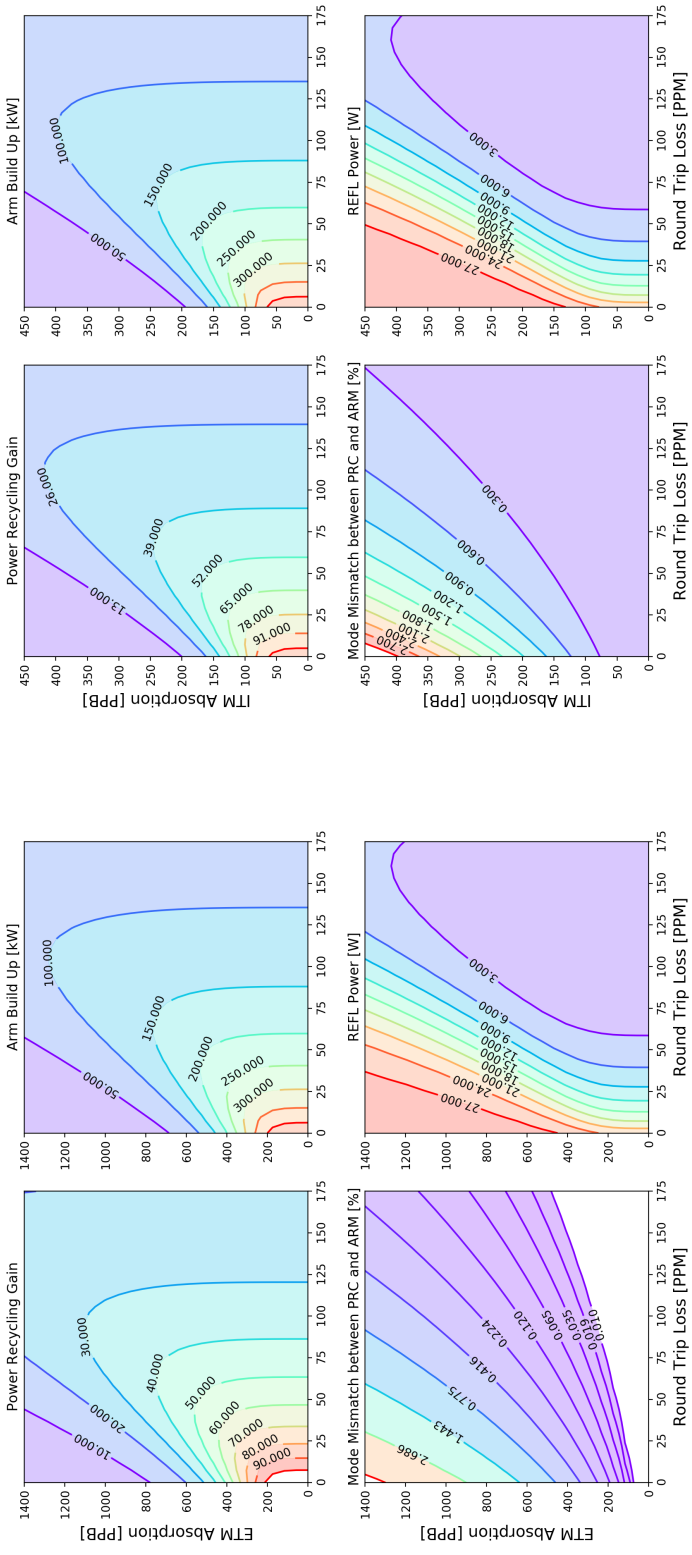

Figure 48 : **Interferometer DC powers as a function of round trip arm loss and test mass absorption.** Simplifying the power recycling cavity and a combined arm model to understand the powers as a function of loss has a few advantages with regards to computational time and the results are easier to conceptually understand. Here, absorption changes the radius of curvature and substrate thermal lens which results in some mode mismatch while the round trip loss takes into account the rest of the higher order modes from point absorbers. The ITM absorption has a much larger effect on the overall power recycling gain loss by almost a factor of 3 compared to ETM absorption. Of course, the simplified model will fall short in describing effects on the antisymmetric signals of the full interferometer.

6.6 Higher Power Operation

The goal for O3 is 150 kW of circulating power in the arms. With the sensors and tests described in the preceding sections, a cohesive plan to pre-load the interferometer was implemented in order to achieve stable higher power operation in the detectors. Generally, the Thermal Compensation System has two goals: Firstly, the actuators are used to pre-load the test masses with heat in anticipation of the lensing due to the interferometer while operating at full lock and higher power. Secondly, the amount of mode-matching between the coupled cavities must be optimized in order to achieve the best sensitivity. Using the absorptions measured in Figure 43, it is possible to estimate the total amount of lensing from self-heating as a function of input power (see Figure 45).

In principle, the Hartmann measurements of absorbed power should provide sufficient information to pre-load the interferometer in anticipation of 50 W of input power. The biggest difficulty associated with implementing this thermal compensation scheme was consistently locking DRMI in high micro-seismic conditions. This could be attributed to misalignment of CO_2 lasers to the test masses, which were initially aligned using the Hartmann sensors and double-checked by cycling the lasers on/off to measure the single bounce interferometer beam deflection at the anti-symmetric port. At Hanford, this difficulty for reliably locking the interferometer forced a reduction in pre-loading, so with the combination of estimates provided by the Hartmann Sensors and experimentation with the CO_2 power levels at each stage of increasing the PSL power, the interferometer is able to consistently lock at 30 Watts of PSL input power and $\approx 140\ kW$ of circulating arm power.

During the early phases of commissioning for higher power at Hanford, most of the lock losses occurred when the 18 MHz sidebands in transmission at PR2 (POP-18) would fall below a certain threshold level of approximately 70% of buildup compared to locking at 2 W of input power. This effect was not observed at Livingston and can be attributed to the point absorber that uniquely contaminated H1-ITMY. To study the effects of differential uniform lensing in an interferometer, FINESSE is able to simulate the POP-18 signal at the power recycling pick-off port demodulated at 18 MHz which shows the sideband power buildup in the power recycling cavity (see Figure 49). In this particular simulation the differential lensing requires finding a new

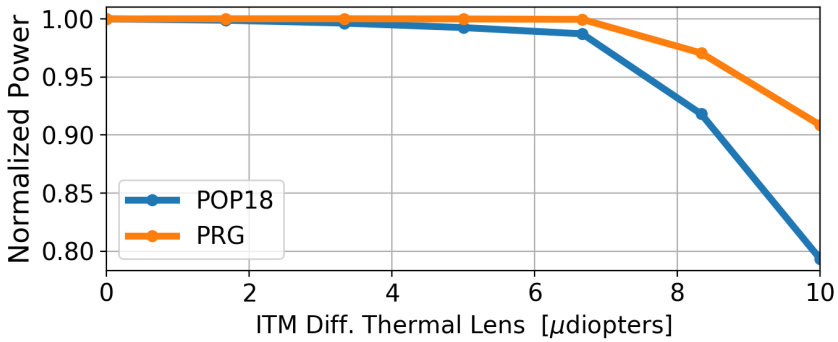

Figure 49 : **Model of POP-18 as a function of differential thermal lensing using FINESSE.** The horizontal axis is differential lensing between the ITMX/ITMY substrates and the vertical axis represents the normalized power when locked with nominal mode matching. Even with modest differential lensing (10 microdiopters), the buildup drops by 20 percent and eventually the simulation has trouble maintaining resonance, similar to the actual interferometer.

operating point to continually lock the longitudinal degrees of freedom. Additionally, the simulated sensors which are used to maintain resonance and measure the RF power need to be re-phased; this agrees with the analytical calculation mentioned in Section 6.1.1 where the carrier power recycling gain is not as adversely affected by the substrate thermal lens compared to the sideband fields.

In the ideal mode matching scenario, the carrier and sidebands resonate differently in the power recycling cavity; where the 9 MHz modulation sidebands has approximately a factor of 10 larger finesse than the carrier [57]. However, this assumes a lossless interferometer and needs to be revisited in the presence of substrate thermal lensing. As with all Pound-Drever-Hall locking, an error signal relies on the static and varying field accumulating different phases to lock the cavity. As lensing causes more losses for the sideband compared to the carrier, the difference in accumulated phase between the two fields is reduced hence the optical gain starts to diminish. For the current Advanced LIGO configuration, all vertex degrees of freedom (PRCL, SRCL, MICH) utilize the POP port for their error signals shown in Figure 50. The degradation can be estimated by injecting a dither line into each degree of freedom and digitally demodulating the respective sensors at the excitation frequency, see Figure 51. This provides insight on how much the optical gain/phase shifts as a function of heating. When powering up to 30 Watts, the loss of optical gain in PRCL is almost 80% with a 10 degrees phase shift, which enough to drive the system towards

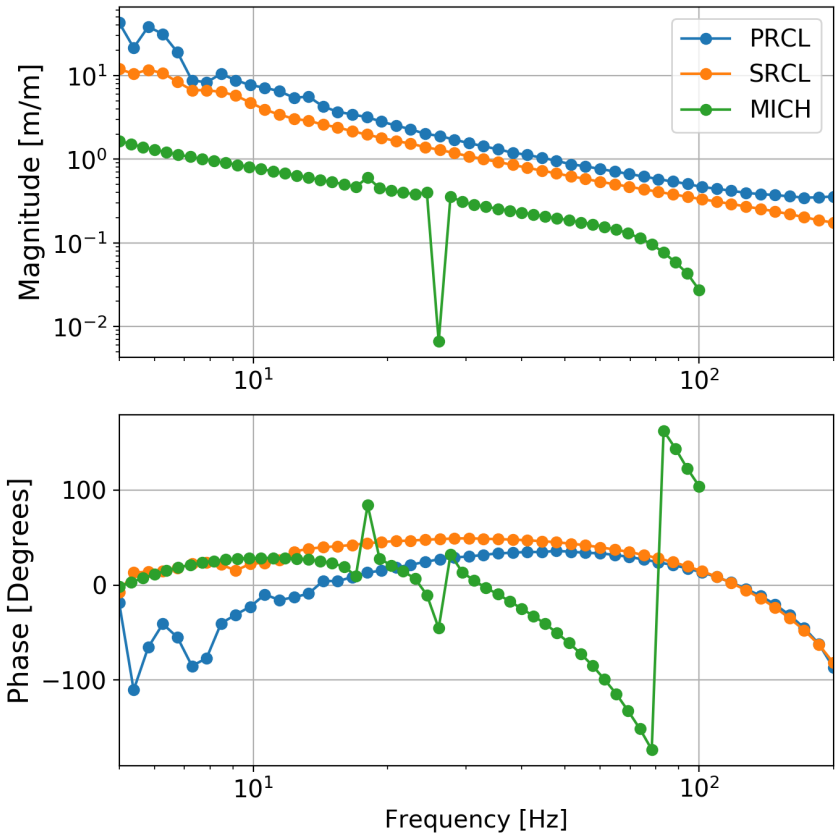

Figure 50 : **Vertex open loop transfer functions while in Nominal Low Noise.** The nominal UGF for PRCL is around 45 Hz.

an unstable loop. This can be compensated by adjusting the digital gain but that fix is only temporary because the problem stems from an optical loss so eventually, the error signal will have no linearity about the zero-point. Alternatively, searching for optimal thermal compensations settings to undo these losses can be very time consuming because of the long thermal time constants and in the case of point absorbers, the current thermal compensation system is not designed to correct the high spatial frequencies. As previously mentioned, one of the main limiters to higher power operation will be reducing the optical loss from mode mismatch.

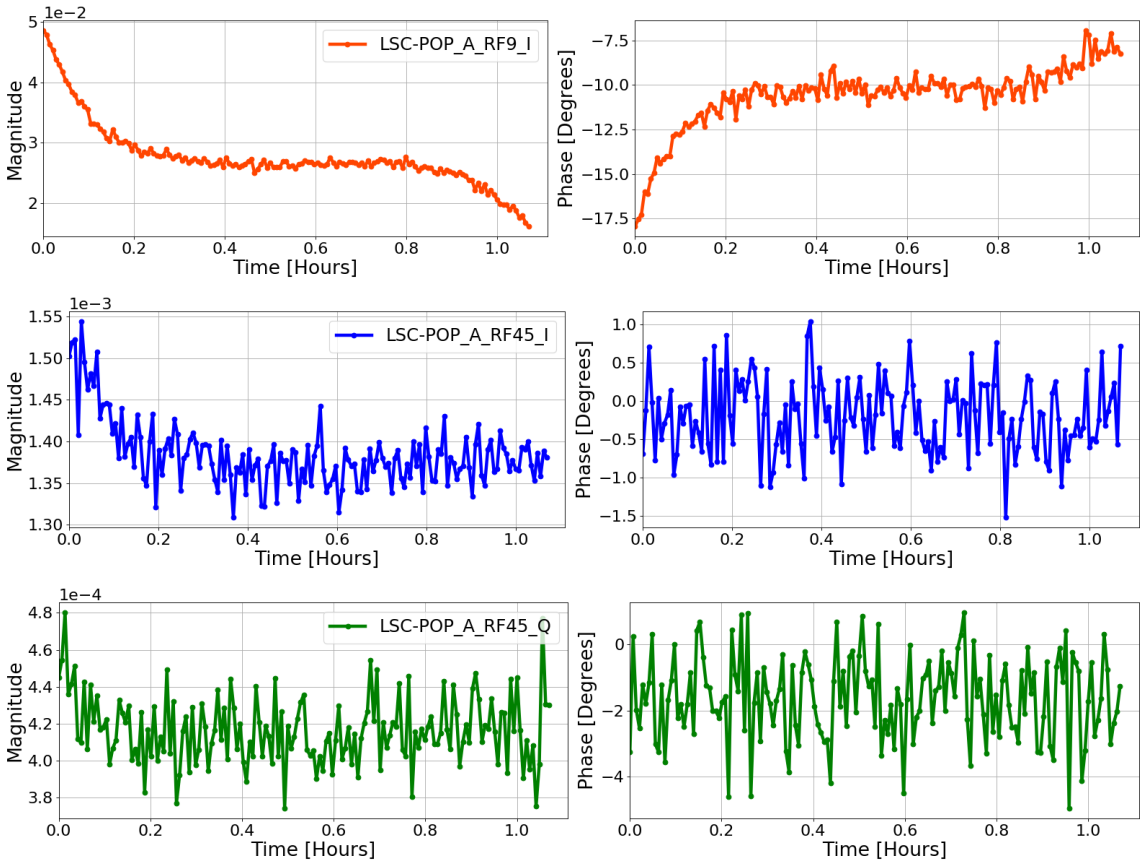

Figure 51 : **Measuring vertex optical gains as a function of heating.** At time t=0, the power begins increasing from 2 watts of input power to 20 watts. In PRCL, there is a reduction to 80% of the starting magnitude and 7.5 degrees of phase rotation with the first power increase. At 0.9 hours, the input power goes from 20 to 30 watts and the magnitude drops to about 30% of the original gain which results in a lock loss. As for the SRCL and MICH degrees of freedom, there are slight changes first power increase but not nearly as bad as PRCL.

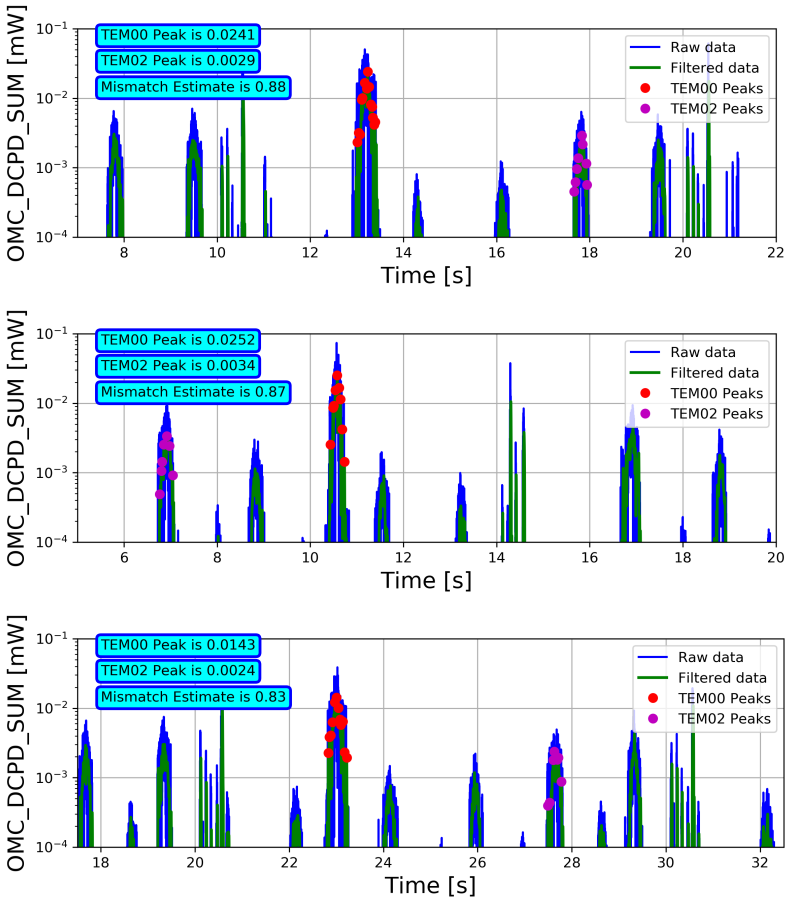

Figure 52 : **OPO to OMC cavity scanning for various Lens2 positions.** The top figure has the lens closest to the OPO along the propagation axis, the middle figure represents Lens2 at half the actuation range and the bottom figure shows the lens furthest from the OPO. During this time, the OMC ASC control loops were closed on the reflected QPDs to minimize the odd order mode coupling.

6.7 Mode Matching from the OPO to the OMC

As mentioned in Chapter 2, one of the main limitations to effective squeezing is mode mismatch which needs to be characterized carefully. Generally, the mode exiting the OPO and OMC cavities are accurately determined from design values but the path lengths and mode profile was measured and the results are presented in this section.

Using the OMC as an optical spectrum analyzer is one simplest methods for understanding the mode matching coming out of the interferometer. In a single bounce configuration, measuring the ratio between the second order mode and the fundamental gives a first look at the limit of matching. Similar techniques can be

used with the squeezed beam as well and during commissioning of the squeezer, a mode mismatch between 12-17% was observed which led to a re-design of the OPO to OMC optical path. Figure 52 shows the results for scanning the OMC length using PZT2 with the ASC control loops closed on the reflected QPDs to minimize odd-order mode coupling. The measurements were taken in-air which made the results rather noisy so before the peak-finding algorithm tries to fit the 00 or 02 modes, the data is low-passed with a corner frequency of 1kHz.

Using a well-calibrated mode profiler that measures beam sizes along the propagation axis is the most direct way of determining OPO to OMC mode matching. This method can also predict the actuator Gouy phase of the second lens after the OPO, which is on a translation stage with approximately 4 centimeters of range. Generally, the length measurement between optics is the largest systematic error especially in the near-field where beam sizes do not change very much as a function of $\hat{z}$. In addition, places to put a beam profiler become very limited as HAM6 becomes crowded with optical components. In preparation for squeezing in Advanced LIGO, the mode matching from the OPO to OMC was measured and found to be approximately 88% at best. When implementing a telescope with fast lenses, the distances between optics must be stringently characterized but the OPO platform is very crowded along the output path so it was very difficult to accurately measure the path lengths with a ruler. Between the second lens and ZM1, the table is much clearer and by removing Lens2, the Gouy phase is approximately in the far-field which means the distance measurements can be more easily measured as a function of beam size. Figure 53 shows the results of characterizing the OPO output mode as it enters HAM5 by removing Lens2, a fit constrains the Lens1 positioning and the OPO mode is assumed from its design document [70].

With the poor mode matching shown in Figure 54, the fast telescope lenses needed to be replaced, or otherwise, risk being the limit to effective squeezing for O3. The available range in the translation stage did not allow for increased matching and the crowded OPO platform did not permit coarse moves of Lens1. In addition, moving the translation stages for Lens2 closer to the OPO cavity does not gain any extra mode overlap. The next option was replacing the lenses with a solution which did not incorporate large actuation range but was more suited for mode matching. There were a few clean lenses available that provided the right solution but greatly reduced

the translation stage efficacy, on the other hand, this made the telescope placement much more robust to path length errors which is the original problem to begin with. The new model is shown in Figure 55 where the lenses are now $f^{\text{new}}_{\text{Lens1}} = 250$ mm and $f^{\text{new}}_{\text{Lens2}} = 350$ mm where Lens1 is closer to the OPO output. The calculated overlap integral between the expected OMC mode and the squeezer is on the order of 99% with very little sensitivity in the Lens2 positioning as expected. Follow up measurements with OMC scans in-vacuum indicate approximately 95% mode matching between the OPO to SRM and back to the OMC, this is due to the astigmatism mentioned previously that is still prevalent after changing the lenses. However, the mode matching from the OPO to ITMs and back to the OMC shows 99% mode matching with the new lens configuration [19] which is effectively the path of squeezed light. It is important to note that measurements taken in-vacuum had pre-loaded TCS settings in anticipation for 50 W.

For future implementations of high sensitivity telescopes, length measurements between optics will need to be more stringently constrained with specialized tools such as laser range finders or mechanical jigs while simultaneously re-confirmed with profile scans to understand the laser beam entering the interferometer. Distances between optics were the largest source of uncertainties in these measurements so understanding the optical path length will help curb the systematic errors.

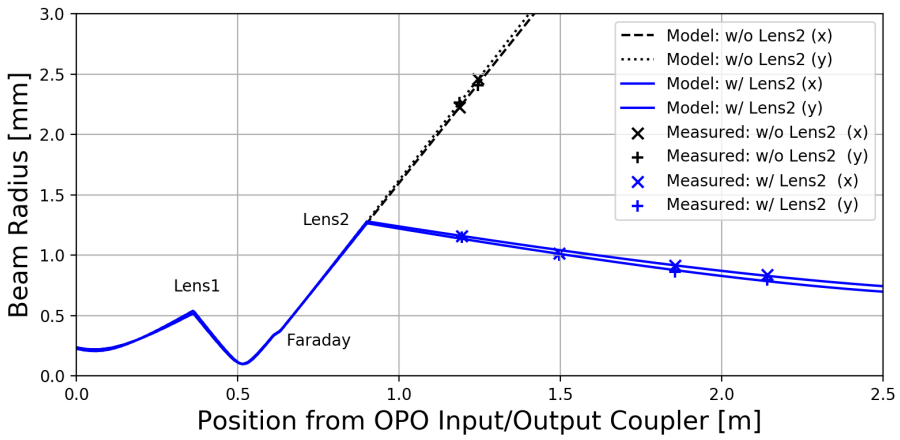

Figure 53 : **Mode measurement from the OPO.** The results without Lens2 are shown in black for two transverse directions (x/y) and constrain the distance of Lens1 relative to the OPO output. Then, Lens2 is replaced back in its original position on a translation stage at half the range and measurements were taken in order to constrain the distance between Lens1 and Lens2. The beam sizes were fit to find the Gaussian q-parameter entering HAM5. There is some slight deviation in the transverse directions after Lens2, possibly from misalignment of the lens. This method seems to provide a good model of what beam is being injected from the squeezer side.

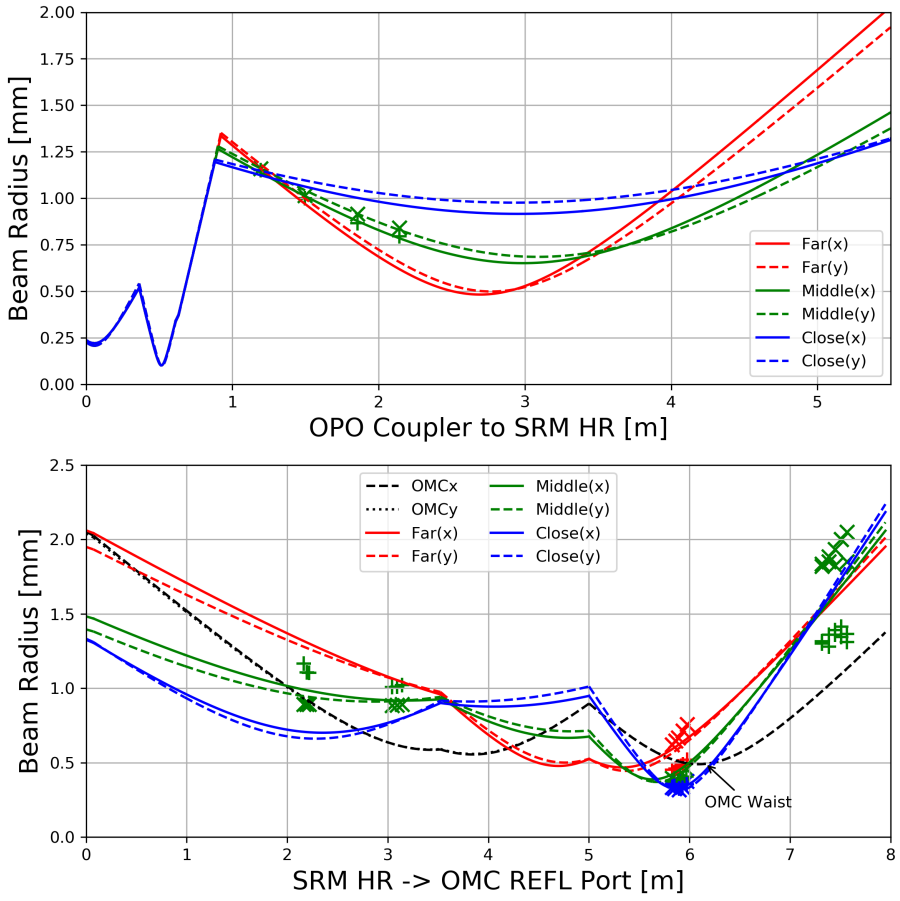

Figure 54 : **Projecting the modes from the squeezer to the OMC.** Determining the actuation range with the translation stage using the as-installed focal lengths, $f_{\mathrm{Lens1}} = 111$ mm and $f_{\mathrm{Lens2}} = 334$ mm, showed that the mode matching into the OMC was at most 80% with various translation stage positions with "Close" referring to the position of Lens2 relative to the OPO cavity. Here, crosses represent the transverse-x direction and pluses denote the transverse-y orientation. One very interesting feature is that the astigmatism as measured seems to be worse after re-entering HAM6 from HAM5 and is not explainable by the slight deviations shown in Figure 53, so it is possible that some sort of clipping occurs while propagating through the main output Faraday isolator. Near the OMC waist, the predicted mode shapes for different translation stage positions agree with the measured beam sizes and power overlaps were confirmed to be accurate with OMC scans to within a percent.

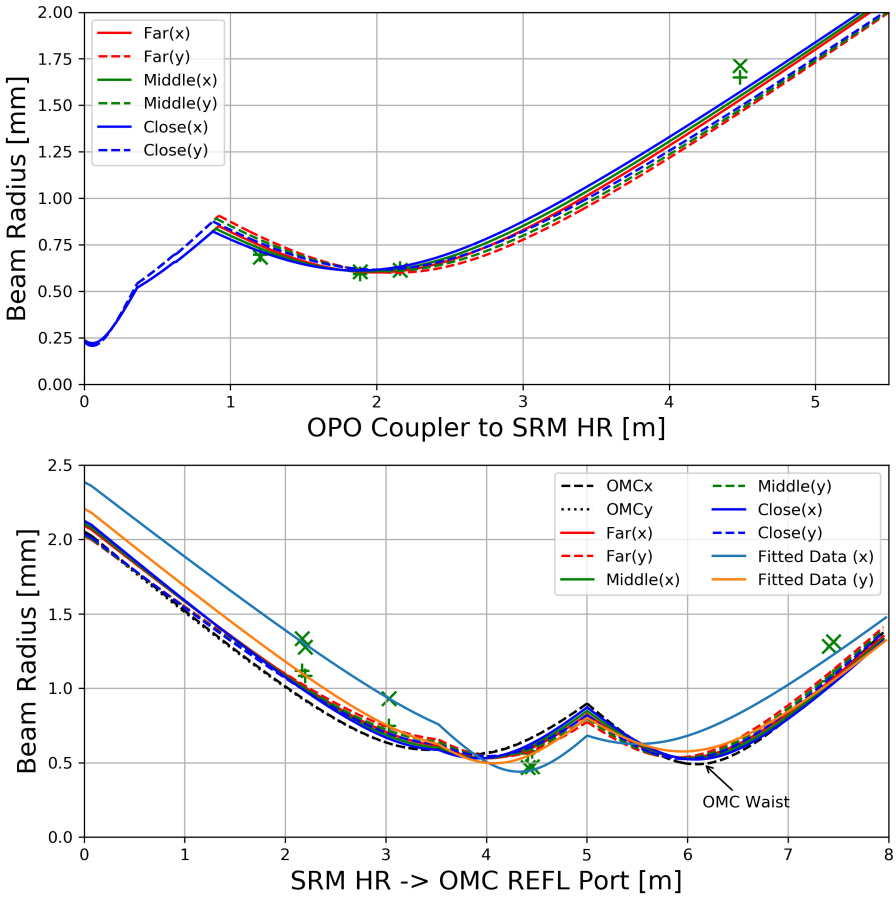

Figure 55 : **Repeated measurements with new lenses.** The model tries a few different lens solutions and settles on $f^{\text{new}}_{\text{Lens1}} = 250$ mm and $f_{\text{Lens2}} = 350$ mm, which severely limits the actuation range. However, it shows approximately 97% mode matching for the fitted transverse-y data and 92% for the transverse-x data. Astigmatism which was already shown in Figure 54 is still prevalent here and brings the average mode matching to 95% from the OPO to OMC in the single bounce configuration.

Chapter 7

Conclusions

The LIGO detectors are currently entering the engineering run to start observing astrophysical events at the best network sensitivities ever achieved for binary neutron star inspirals and both machines include upgrades to inject squeezed vacuum. The mode matching work presented in this thesis helped reduce the optical losses at Hanford and a parallel team implemented similar work at Livingston. In addition, it has been shown that active wavefront control will need to be carefully considered for future design phases for the next generation of laser interferometric gravitational wave detectors where its difficulties are rooted in both the noise performance and operational stability. It has also been shown that substrate thermal lensing from excess absorption will be the critical limiter for increasing input power. The continuation of engineering and science tasks are itemized below:

- Point Absorbers
  - Early detection of point absorbers is crucial, so resonating each arm with power recycling and maximal input power ahead of full lock acquisition is a possible strategy for mapping out the optimal spot position on each test mass.
  - Corrections for the high spatial frequencies from point absorbers will require significant re-work of the current thermal compensation hardware which is underway with custom masks for the CO2 lasers. This will help with sideband build ups but does not solve the arm scatter losses which limit the sensitivity improvement with increased higher power. However,

it does provide the possibility of reducing the 9 Mhz higher order mode RIN coupling which co-resonates in the OMC.

  - For Advanced LIGO, POP sensors provide the most sensitive error signals for the longitudinal vertex degrees of freedom [57][58][59]. However, in the face of irreparable lensing from point absorbers, re-visiting the sensing matrix for the available ports when the interferometer has reached thermal equilibrium may yield a better sensor for locking PRCL.

- Global Mode Matching

  - Even if the point absorbers are not present, to truly implement a system that solves the mode matching challenges presented in LIGO, an active control scheme that implements both sensors and actuators will be required to span the degrees of freedom that are present in the interferometer. Similar to the angular wavefront sensors already being used in LIGO at the time of this writing, the active wavefront control system should be expanded to a global sensing and actuation scheme, however, this adds to an already heavy commissioning load in preparing for runs.
  - The addition of mode converters and phase cameras will provide a glimpse into the interferometer modal content which is crucial in determining the upper limits of operating power. The effect of point absorbers on the interferometer noise is an on-going area of research but it is clear that increased differential substrate lensing beyond the Advanced LIGO specifications will increase the technical complications of high power operation.

- Hartmann Sensor Tunings

  - Reducing the amount of in-chamber clipping on the Hartmann Sensors will provide more accurate and reliable results to estimate the total absorption, this can be done by replacing the in-vacuum steering mirrors with picomotors in preparation for the fourth observing run.
  - Implementation of the current Thermal Compensation System still faces challenges with reliable lock acquisition when pre-loading the ring heaters in anticipation for 50 Watts of power but with the combination of careful

Hartmann Sensor tuning and sufficient fine-tuning it is possible to obtain the desired settings.

- Squeezer to Interferometer Mode Matching
  - Integrating reliable path length measurements with beam profile scans will make existing models more accurate which is important when using high sensitivity telescopes.

Appendices

Appendix A

Resonator Formulas

Equation 2.40 describes the stability condition for a two mirror Fabry-Perot cavity, but is worthwhile to derive the criterion for geometric stability from the ray matrix tools commonly used in optics. The alignment of two plane waves traveling in space can differ by two quantities: the axial and angular separations, y and θ, respectively. These two quantities can be transformed via these optical matrices:

Lens:

$$\hat{F}_i = \begin{pmatrix} 1 & 0 \\ -\frac{1}{f_i} & 1 \end{pmatrix} \tag{A.184}$$

Curved Mirror:

$$\hat{M}_i = \begin{pmatrix} 1 & 0 \\ \frac{2}{R_i} & 1 \end{pmatrix} \tag{A.185}$$

Space:

$$\hat{D}_i = \begin{pmatrix} 1 & d_i \\ 0 & 1 \end{pmatrix} \tag{A.186}$$

Using these matrices, the periodic Fabry-Perot with two mirrors can be represented by the matrix,

$$\begin{pmatrix} y_{m+1} \\ \theta m + 1 \end{pmatrix} = \hat{M}_{FP} \begin{pmatrix} y_m \\ \theta m \end{pmatrix} \tag{A.187}$$

where

$$\hat{M}_{FP} = \hat{M}_i \hat{D}_i \hat{M}_i \hat{D}_i \tag{A.188}$$

is the optical transfer matrix. The goal is to find a geometric condition that is

dependent on the optical transfer matrix which keeps the axial displacement from diverging.

$$\begin{pmatrix} y_{m+1} \\ \theta m+1 \end{pmatrix} = \begin{pmatrix} A & B \\ C & D \end{pmatrix} \begin{pmatrix} y_m \\ \theta m \end{pmatrix} \tag{A.189}$$

which means

$$\theta_m = \frac{y_{m+1} - A\, y_m}{B} \tag{A.190a}$$

$$\theta_{m+1} = \frac{y_{m+2} - A\, y_{m+1}}{B} \tag{A.190b}$$

Solving for y_{m+2}

$$y_{m+2} = (A+D)\, y_{m+1} - \det(\hat{M}_{FP}) y_m \tag{A.191}$$

Assuming a geometrical solution where $y_m = y_o h^m$ and plugging into the equation above,

$$h^2 = (A+D)\, h - \det(\hat{M}_{FP}) \tag{A.192}$$

which is a quadratic equation that has two solutions and can be further simplified if the index of refraction for the entire system remains constant such that $\det(\hat{M}_{FP}) = 1$. Plugging back into y_m and doing some algebra

$$y_m \propto \sin(m\phi) \tag{A.193}$$

where $\phi = \cos^{-1}(\frac{A+D}{2})$, which is also referred to as the round trip Gouy phase of the cavity. In order for y_m to be harmonic instead of hyperbolic and hence confined, this condition must be met

$$\frac{|A+D|}{2} \leq 1 \tag{A.194}$$

By actually calculating the terms of $\hat{M}_{FP}$ and doing even more algebra, it is clear that

$$0 \leq \left(1 - \frac{L}{R_1}\right)\left(1 - \frac{L}{R_2}\right) \leq 1 \tag{A.195}$$

which is what was stated in equation 2.40. There is a simpler and less algebraic way to reach the same conclusion by looking at the Rayleigh range of a finite Gaussian beam for a simple cavity. In Table II of Kogelnik and Li [61], there is an expression for the Rayleigh range

$$\begin{aligned} z_R^2 &= \frac{L(R_1 - L)(R_2 - L)(R_1 + R_2 - L)}{(R_1 + R_2 - 2L)^2} \\ &= \frac{g_1 g_2 (1 - g_1 g_2}{(g_1 - g_2 - 2g_1 g_2)^2} \end{aligned} \tag{A.196}$$

If the Rayleigh range is a real number, then once again, equation 2.40 must be true.

Appendix B

Hermite Gauss Normalization

According to equation 3.112, the higher order modes in the Hermite Gauss basis has the intensity profile,

$$I_{mn}(x,y,z) = |A_{mn}|^2 \left[\frac{W_0}{W(z)}\right]^2 \mathbb{G}_n^2\left(\frac{\sqrt{2}x}{W(z)}\right)\mathbb{G}_n^2\left(\frac{\sqrt{2}y}{W(z)}\right) \tag{B.197}$$

It is useful to normalize the first few lowest order modes with respect to the total optical power since the Gaussian beam will couple to them the most due either misalignment or mode mismatch as seen in section []. In one dimension, the total optical power for the first 3 modes are

$$\begin{aligned}
P_0(x,y,z) &= \int_{-\infty}^{\infty} |A_0|^2 \left[\frac{W_0}{W(z)}\right] e^{-2x^2/w^2(z)} dx \\
P_1(x,y,z) &= \int_{-\infty}^{\infty} |A_1|^2 \left[\frac{W_0}{W(z)}\right] \frac{8x^2}{w^2(z)} e^{-2x^2/w^2(z)} dx \\
P_2(x,y,z) &= \int_{-\infty}^{\infty} |A_2|^2 \left[\frac{W_0}{W(z)}\right] \left(\frac{8x^2}{w^2(z)} - 2\right)^2 e^{-2x^2/w^2(z)} dx
\end{aligned} \tag{B.198}$$

In two dimensions, the total optical power for the first 3 modes are

$$
\begin{aligned}
P_{00}(x,y,z) &= \int_{-\infty}^{\infty}\int_{-\infty}^{\infty} |A_{00}|^2 \left[\frac{W_0}{W(z)}\right]^2 e^{-2x^2/w^2(z)} e^{-2y^2/w^2(z)} dxdy \\
P_{10}(x,y,z) &= \int_{-\infty}^{\infty}\int_{-\infty}^{\infty} |A_{10}|^2 \left[\frac{W_0}{W(z)}\right]^2 \frac{8x}{w^2(z)} e^{-2x^2/w^2(z)} e^{-2y^2/w^2(z)} dxdy \\
P_{20}(x,y,z) &= \int_{-\infty}^{\infty}\int_{-\infty}^{\infty} |A_{20}|^2 \left[\frac{W_0}{W(z)}\right]^2 \left(\frac{8x^2}{w^2(z)} - 2\right)^2 e^{-2x^2/w^2(z)} e^{-2y^2/w^2(z)} dxdy
\end{aligned}
\tag{B.199}
$$

By setting the equations above to unity, the normalization factors become

$$
\begin{aligned}
A_0 &= \left(\frac{2}{\pi w_0^2}\right)^{1/4} \\
A_1 &= \left(\frac{2}{\pi w_0^2}\right)^{1/4} \frac{1}{\sqrt{2}} \\
A_2 &= \left(\frac{2}{\pi w_0^2}\right)^{1/4} \frac{1}{\sqrt{8}}
\end{aligned}
\tag{B.200}
$$

$$
\begin{aligned}
A_{00} &= \sqrt{\frac{2}{\pi w_0^2}} \\
A_{10} &= \sqrt{\frac{1}{\pi w_0^2}} \\
A_{20} &= \sqrt{\frac{1}{4\pi w_0^2}}
\end{aligned}
\tag{B.201}
$$

Appendix C

Bullseye and Quadrant Photodiode Characterization

Both RF and DC segmented photodiodes are widely used in LIGO's sensing schemes, however, the quadrant photodiodes (QPDs) are more readily implemented. Recently, a bullseye photodiode has been installed upstream of the pre-mode cleaner to sense the size and angular jitter noise contribution from the high powered oscillator. It is useful to have angular sensors both upstream and downstream of optical cavities to narrow down where jitter could be coupling into the optical path. That being said, to calibrate the two types of sensors in common units, it is easiest to scale by beam diameters.

C.1 Quadrant Photodiodes (QPD)

Calculating the QPD response to angular jitter is relatively straight forward. Beginning with a Gaussian beam in rectangular coordinates that is displaced along the horizontal axis by a small value Δx and expanding to first order:

$$\begin{aligned} I(x,y) &= \left(\frac{2}{\pi w^2}\right) e^{-2\frac{(x+\Delta x)^2+y^2}{w^2}} \\ &\approx \left(\frac{2}{\pi w^2}\right) e^{-2\frac{x^2+y^2}{\omega^2}} \left(1 - \frac{4x\Delta x}{w^2}\right) \end{aligned} \tag{C.202}$$

	Seg 1	Seg 2	Seg 3	Seg 4
Pit	1	1	-2	0
Yaw	-1	1	0	0
Wid	1	1	1	-1
Sum	1	1	1	1

Table 6 : Bullseye photodiode sensing matrix.

Converting to polar coordinates where $x = r\cos\theta$ and $y = r\sin\theta$ then integrating over the individual segments to get the power,

$$\begin{aligned} P &= \left(\frac{2}{\pi w^2}\right)\int_0^{\infty}\int_{\theta_1}^{\theta_2} e^{-2\frac{r^2}{\omega^2}}\left(1-\frac{4r\cos\theta}{w^2}\Delta x\right) r\mathrm{d}r\mathrm{d}\theta \\ &= \frac{1}{2} - [\cos\theta_2 - \cos\theta_1]\frac{8\Delta x}{\pi\omega^4}\int_0^{\infty} e^{-2\frac{r^2}{\omega^2}} r^2\mathrm{d}r \\ &= \frac{1}{2} - [\cos\theta_2 - \cos\theta_1]\frac{\Delta x}{2\pi\omega^2}\left(\sqrt{2\pi}\omega\ \mathrm{erf}(\frac{\sqrt{2}r)}{\omega}) - 4re^{-2\frac{r^2}{\omega^2}}\right)\Bigg|_0^{\infty} \\ &= \frac{1}{2} - [\cos\theta_2 - \cos\theta_1]\frac{\Delta x}{w}\sqrt{\frac{1}{2\pi}} \end{aligned} \tag{C.203}$$

where θ_1 and θ_2 are the limits from $\pm\pi/2$ for the right half and $\mp\pi/2$ for the left half. Denoting the right and left segment as P_2 and P_1, respectively, it is possible to subtract the halves and obtain a calibrated DC signal in units of beam diameter.

$$S = P_2 - P_1 = 2\sqrt{\frac{2}{\pi}}\frac{\Delta x}{\omega} \tag{C.204}$$

It is trivial to repeat the calculation for vertical displacements so it is left for the reader to complete.

C.2 Bullseye Photodiodes

Similar to the QPD calibration above, it is possible to express pitch and yaw displacements that are normalized to beam diameters. Additionally, the bullseye's geometry will give insight on the beam size jitter. A sensing matrix for these degrees of freedom is realized in Table 6.

C.2.1 Width

The bullseye's calibration is determined in a similar manner to the QPD however, the sensitivity will inherently depend on the beam size. To calculate what beam size is optimal, first consider a power integral for a cylindrically symmetric Gaussian beam,

$$\begin{aligned} \text{Power} &= \int_A^B |A_{00}|^2 e^{\frac{-2r^2}{\omega^2}} 2\pi r dr \\ &= -|A_{00}|^2 \frac{\pi\omega^2}{2} e^{\frac{-2r^2}{\omega^2}} \Big|_A^B \end{aligned} \tag{C.205}$$

Plugging in limits for the equation where R is the boundary between the inner and outer segments,

$$\text{P}_{\text{in}} = \text{Power}\Big|_0^R = |A_{00}|^2 \frac{\pi\omega^2}{2}[1 - e^{\frac{-2R^2}{\omega^2}}] \tag{C.206}$$

$$\text{P}_{\text{out}} = \text{Power}\Big|_R^\infty = |A_{00}|^2 \frac{\pi\omega^2}{2}[e^{\frac{-2R^2}{\omega^2}}] \tag{C.207}$$

The error signal comes from subtracting the inner segment from the outer,

$$\text{S}_{\text{WID}} = \text{P}_{\text{in}} - \text{P}_{\text{out}} \tag{C.208}$$

Minimizing the derivative with respect to the beam size will determine the optimal width which gives the best sensitivity to beam size change,

$$\begin{aligned} \frac{\partial \text{S}_{\text{WID}}}{\partial\omega} &\approx \frac{8R^2}{\omega^2}\left(1 - \frac{2R^2}{\omega^2}\right) = 0 \\ \Rightarrow \omega &= \sqrt{2}R \end{aligned} \tag{C.209}$$

When determining the beam size, it is possible to measure the beam size directly by fitting the power ratio. For example, if the constraint that $\omega = \sqrt{2}R$ then the power ratio is,

$$\text{DC Power Ratio} = \frac{P_{\text{out}}}{P_{\text{in}}} = \frac{e^{-2R^2/\omega_0^2}}{1 - e^{-2R^2/\omega_0^2}} \approx 0.582 \tag{C.210}$$

C.2.2 Pitch

To calibrate the pitch signal on a bullseye, first consider a Gaussian that is displaced in the vertical direction,

$$\begin{aligned} I^{\text{Pit}}(x,y) &= \left(\frac{2}{\pi w^2}\right) e^{-2\frac{x^2+(y+\Delta y)^2}{w^2}} \\ &\approx \left(\frac{2}{\pi w^2}\right) e^{-2\frac{x^2+y^2}{\omega^2}} \left(1 - \frac{4x\Delta y}{w^2}\right) \end{aligned} \tag{C.211}$$

The integrated power for a given segment is,

$$\begin{aligned} P^{\text{Pit}}_{\theta_1\to\theta_2} &= \left(\frac{2}{\pi w^2}\right) \int_R^\infty \int_{\theta_1}^{\theta_2} e^{-2\frac{r^2}{\omega^2}} \left(1 - \frac{4r\sin\theta}{w^2}\Delta y\right) r\mathrm{d}r\mathrm{d}\theta \\ &= \left(\frac{\theta_2-\theta_1}{2\pi}\right) e^{-2\frac{R^2}{\omega^2}} + (\cos\theta_2 - \cos\theta_1)\frac{1}{\sqrt{2\pi}}\frac{\Delta y}{\omega}\left[\operatorname{erfc}\left(\frac{\sqrt{2}R}{\omega}\right)\sqrt{\frac{8}{\pi}}\frac{R}{\omega}e^{-2\frac{R^2}{\omega^2}}\right] \end{aligned} \tag{C.212}$$

The error signal from a pitch displacement following Table 6 is,

$$S^{\text{Pit}} = P^{\text{Pit}}_{\text{seg1}} + P^{\text{Pit}}_{\text{seg2}} - 2P^{\text{Pit}}_{\text{seg3}} = 3\sqrt{\frac{3}{2\pi}}\frac{\Delta y}{\omega}\left[\operatorname{erfc}\left(\frac{\sqrt{2}R}{\omega}\right) + \sqrt{\frac{8}{\pi}}\frac{R}{\omega}e^{-2\frac{R^2}{\omega^2}}\right] \tag{C.213}$$

C.2.3 Yaw

Using C.202 and repeating the mathematics above, the power for an individual segment is

$$\begin{aligned} P^{\text{Yaw}}_{\theta_1\to\theta_2} &= \left(\frac{2}{\pi w^2}\right) \int_R^\infty \int_{\theta_1}^{\theta_2} e^{-2\frac{r^2}{\omega^2}} \left(1 - \frac{4r\cos\theta}{w^2}\Delta x\right) r\mathrm{d}r\mathrm{d}\theta \\ &= \left(\frac{\theta_2-\theta_1}{2\pi}\right) e^{-2\frac{R^2}{\omega^2}} + (\cos\theta_2 - \cos\theta_1)\frac{1}{\sqrt{2\pi}}\frac{\Delta x}{\omega}\left[\operatorname{erfc}\left(\frac{\sqrt{2}R}{\omega}\right)\sqrt{\frac{8}{\pi}}\frac{R}{\omega}e^{-2\frac{R^2}{\omega^2}}\right] \end{aligned} \tag{C.214}$$

Plugging in the angles to get the signal response in terms of beam radius,

$$S^{\text{Yaw}} = P^{\text{Yaw}}_{\text{seg1}} - P^{\text{Yaw}}_{\text{seg2}} = \frac{3}{\sqrt{2\pi}}\frac{\Delta x}{\omega}\left[\operatorname{erfc}\left(\frac{\sqrt{2}R}{\omega}\right) + \sqrt{\frac{8}{\pi}}\frac{R}{\omega}e^{-2\frac{R^2}{\omega^2}}\right] \tag{C.215}$$

Appendix D

Overlap of Gaussian Beams

When a cavity is mode mismatched to an incoming laser field, the amount of power loss from scattering to higher order modes is quantified by the spatial overlap integral between the TEM00 cavity eigenmode and TEM00 of the input beam. An arbitrary Gaussian integral is defined as,

$$\begin{aligned} |A(r)\rangle &= \frac{A_0}{q(z)} e^{\frac{-ikr^2}{2q(z)}} \\ &= \frac{A_0}{q(z)} e^{\frac{-ikr^2(z-iz_0)}{2|q(z)|^2}} \end{aligned} \tag{D.216}$$

where A_0 is a real amplitude, $q(z) = z + iz_0$ is the complex beam parameter, k is the wave number, and r is the radial variable in the transverse direction. Then normalizing to unity,

$$\langle A(r)|A(r)\rangle = \frac{|A_0|^2}{z^2 + z_0^2} \int_0^\infty e^{\frac{-kr^2 z_0}{|q(z)|^2}} 2\pi r dr = 1 \tag{D.217}$$

$$A_0 = \sqrt{\frac{kz_0}{\pi}} \tag{D.218}$$

For a Gaussian beam with arbitrary q-parameters,

$$|A_i\rangle = \frac{A_{0,i}}{q_i} e^{\frac{-ikr^2(z-iz_0)}{2|q_i|^2}} \tag{D.219}$$

where $z_{0,i}$ is the waist size of one particular beam, the overlap integral for the amplitude becomes

$$\langle A_1|A_2\rangle = 2i\frac{z_{0,1}z_{0,2}}{q_1 - q_2^*} \tag{D.220}$$

So the power overlap is:

$$\text{Power Overlap} = |\langle A_1|A_2\rangle|^2 = 4\frac{z_{0,1}z_{0,2}}{|q_1 - q_2^*|^2} \tag{D.221}$$

Essentially, mode matching an optical system only requires the designer to match the incoming beam's q-parameter to the cavity's, so it makes sense that the final power overlap depends only on the waist size and location.

Bibliography

[1] J. Abadie et al. Sensitivity Achieved by the LIGO and Virgo Gravitational Wave Detectors during LIGO's Sixth and Virgo's Second and Third Science Runs. *arXiv*, 2012. 6

[2] B. P. e. a. Abbott. Observation of gravitational waves from a binary black hole merger. *Phys. Rev. Lett.*, 116:061102, Feb 2016. doi: 10.1103/PhysRevLett.116.061102. URL `https://link.aps.org/doi/10.1103/PhysRevLett.116.061102`. i

[3] B. P. e. a. Abbott. Gw170817: Observation of gravitational waves from a binary neutron star inspiral. *Phys. Rev. Lett.*, 119:161101, Oct 2017. doi: 10.1103/PhysRevLett.119.161101. URL `https://link.aps.org/doi/10.1103/PhysRevLett.119.161101`. i

[4] R. Abbott, R. Adhikari, G. Allen, S. Cowley, E. Daw, D. DeBra, J. Giaime, G. Hammond, M. Hammond, C. Hardham, J. How, W. Hua, W. Johnson, B. Lantz, K. Mason, R. Mittleman, J. Nichol, S. Richman, J. Rollins, D. Shoemaker, G. Stapfer, and R. Stebbins. Seismic isolation for advanced ligo. *Classical and Quantum Gravity*, 19(7):1591, 2002. URL `http://stacks.iop.org/0264-9381/19/i=7/a=349`. 33

[5] D. Z. Anderson. Alignment of resonant optical cavities. *Appl. Opt.*, 23(17): 2944–2949, Sep 1984. doi: 10.1364/AO.23.002944. URL `http://ao.osa.org/abstract.cfm?URI=ao-23-17-2944`. 47

[6] K. Arai. H1 omc hom/sb resonant structure (and possible mitigation of 9th-order 9mhz sb resonance), 2019. URL `https://alog.ligo-wa.caltech.edu/aLOG/index.php?callRep=46667`. 106

[7] M. Beijersbergen, L. Allen, H. van der Veen, and J. Woerdman. Astigmatic laser mode converters and transfer of orbital angular momentum. *Optics Communications*, 96(1):123 – 132, 1993. ISSN 0030-4018. doi: https://doi.org/10.1016/0030-4018(93)90535-D. URL http://www.sciencedirect.com/science/article/pii/003040189390535D. 47, 74

[8] P. G. Bergmann. Summary of the chapel hill conference. *Rev. Mod. Phys.*, 29: 352–354, Jul 1957. doi: 10.1103/RevModPhys.29.352. URL https://link.aps.org/doi/10.1103/RevModPhys.29.352. 3

[9] E. D. Black. An introduction to pound–drever–hall laser frequency stabilization. *American Journal of Physics*, 69(1):79–87, 2001. doi: 10.1119/1.1286663. URL https://doi.org/10.1119/1.1286663. 12, 15, 18

[10] D. G. Blair. *The detection of gravitational waves*. Cambridge University Press, 2005. 33

[11] C. Bond, D. Brown, A. Freise, and K. A. Strain. Interferometer techniques for gravitational-wave detection. *Living Reviews in Relativity*, 19(1):3, Feb 2017. ISSN 1433-8351. doi: 10.1007/s41114-016-0002-8. URL https://doi.org/10.1007/s41114-016-0002-8. 58

[12] C. e. a. Bond. Finesse input files for the h1 interferometer, 2013. URL https://dcc.ligo.org/LIGO-T1300904. 25, 59

[13] A. Brooks, P. Veitch, J. Munch, and T.-L. Kelly. An off-axis hartmann sensor for the measurement of absorption-induced wavefront distortion in advanced gravitational wave interferometers. *General Relativity and Gravitation*, 37(9): 1575–1580, Sep 2005. ISSN 1572-9532. doi: 10.1007/s10714-005-0137-5. URL https://doi.org/10.1007/s10714-005-0137-5. 91

[14] A. F. Brooks. *Hartmann Wavefront Sensors for Advanced Gravitational Wave*. PhD thesis, The University of Adelaide, 7 2007. 91

[15] A. F. Brooks, T.-L. Kelly, P. J. Veitch, and J. Munch. Ultra-sensitive wavefront measurement using a hartmann sensor. *Opt. Express*, 15(16):10370–10375,

Aug 2007. doi: 10.1364/OE.15.010370. URL http://www.opticsexpress.org/abstract.cfm?URI=oe-15-16-10370. 91

[16] A. F. Brooks, D. Hosken, J. Munch, P. J. Veitch, Z. Yan, C. Zhao, Y. Fan, L. Ju, D. Blair, P. Willems, B. Slagmolen, and J. Degallaix. Direct measurement of absorption-induced wavefront distortion in high optical power systems. *Appl. Opt.*, 48(2):355–364, Jan 2009. doi: 10.1364/AO.48.000355. URL http://ao.osa.org/abstract.cfm?URI=ao-48-2-355. 91

[17] A. F. Brooks, B. Abbott, M. A. Arain, G. Ciani, A. Cole, G. Grabeel, E. Gustafson, C. Guido, M. Heintze, A. Heptonstall, M. Jacobson, W. Kim, E. King, A. Lynch, S. O'Connor, D. Ottaway, K. Mailand, G. Mueller, J. Munch, V. Sannibale, Z. Shao, M. Smith, P. Veitch, T. Vo, C. Vorvick, and P. Willems. Overview of advanced ligo adaptive optics. *Appl. Opt.*, 55(29):8256–8265, Oct 2016. doi: 10.1364/AO.55.008256. URL http://ao.osa.org/abstract.cfm?URI=ao-55-29-8256. 90, 91, 92, 93

[18] D. Brown. Personal Communication, 2018. 96

[19] D. Brown. 992018. URL https://alog.ligo-wa.caltech.edu/aLOG/index.php?callRep=45511. 117

[20] A. Buonanno and Y. Chen. Quantum noise in second generation, signal-recycled laser interferometric gravitational-wave detectors. *Phys. Rev. D*, 64:042006, Jul 2001. doi: 10.1103/PhysRevD.64.042006. URL https://link.aps.org/doi/10.1103/PhysRevD.64.042006. 28

[21] S. M. Carroll. *Spacetime and geometry: an introduction to general relativity.* Pearson, 2003. 1

[22] C. M. Caves. Quantum-mechanical noise in an interferometer. *Phys. Rev. D*, 23:1693–1708, Apr 1981. doi: 10.1103/PhysRevD.23.1693. URL https://link.aps.org/doi/10.1103/PhysRevD.23.1693. 28

[23] C. M. Caves and B. L. Schumaker. New formalism for two-photon quantum optics. i. quadrature phases and squeezed states. *Phys. Rev. A*, 31:3068–3092,

May 1985. doi: 10.1103/PhysRevA.31.3068. URL https://link.aps.org/doi/10.1103/PhysRevA.31.3068. 28, 38

[24] C. M. Caves, K. S. Thorne, R. W. P. Drever, V. D. Sandberg, and M. Zimmermann. On the measurement of a weak classical force coupled to a quantum-mechanical oscillator. i. issues of principle. *Rev. Mod. Phys.*, 52:341–392, Apr 1980. doi: 10.1103/RevModPhys.52.341. URL https://link.aps.org/doi/10.1103/RevModPhys.52.341. 28

[25] J. L. Cervantes-Cota, S. Galindo-Uribarri, and G. F. Smoot. A brief history of gravitational waves. *Universe*, 2(3), 2016. ISSN 2218-1997. doi: 10.3390/universe2030022. URL http://www.mdpi.com/2218-1997/2/3/22. 3

[26] Y. Chen, S. L. Danilishin, F. Y. Khalili, and H. Müller-Ebhardt. Qnd measurements for future gravitational-wave detectors. *General Relativity and Gravitation*, 43(2):671–694, Feb 2011. ISSN 1572-9532. doi: 10.1007/s10714-010-1060-y. URL https://doi.org/10.1007/s10714-010-1060-y. 28

[27] S. S. Y. Chua. *Quantum Enhancement of a 4km Laser Interferometer Gravitational-Wave Detector*. PhD thesis, The Australian National University, 4 2013. 40

[28] L. Collaboration. Ligo optics, 2019. URL https://galaxy.ligo.caltech.edu/optics/. 15, 22, 67

[29] T. L. S. Collaboration. A gravitational wave observatory operating beyond the quantum shot-noise limit. *Nature Physics*, 7:962, Nov 2009. doi: 10.1038/nphys2083. URL http://dx.doi.org/10.1038/nphys2083. 38

[30] T. L. S. Collaboration. Enhanced sensitivity of the ligo gravitational wave detector by using squeezed states of light. *Nature Physics*, 7:613, Jul 2013. doi: 10.1038/nphoton.2013.177. URL http://dx.doi.org/10.1038/nphoton.2013.177. 38

[31] T. L. S. Collaboration. Advanced ligo. *Classical and Quantum Gravity*, 32(7):074001, 2015. URL http://stacks.iop.org/0264-9381/32/i=7/a=074001. 19

[32] R. DeRosa, J. C. Driggers, D. Atkinson, H. Miao, V. Frolov, M. Landry, J. A. Giaime, and R. X. Adhikari. Global feed-forward vibration isolation in a km scale interferometer. *Classical and Quantum Gravity*, 29(21):215008, 2012. URL http://stacks.iop.org/0264-9381/29/i=21/a=215008. 33

[33] J. C. Driggers, J. Harms, and R. X. Adhikari. Subtraction of newtonian noise using optimized sensor arrays. *Physics Review D*, 86(10):102001, Nov. 2012. doi: 10.1103/PhysRevD.86.102001. 37

[34] S. Dwyer, L. Barsotti, S. S. Y. Chua, M. Evans, M. Factourovich, D. Gustafson, T. Isogai, K. Kawabe, A. Khalaidovski, P. K. Lam, M. Landry, N. Mavalvala, D. E. McClelland, G. D. Meadors, C. M. Mow-Lowry, R. Schnabel, R. M. S. Schofield, N. Smith-Lefebvre, M. Stefszky, C. Vorvick, and D. Sigg. Squeezed quadrature fluctuations in a gravitational wave detector using squeezed light. *Opt. Express*, 21(16):19047–19060, Aug 2013. doi: 10.1364/OE.21.019047. URL http://www.opticsexpress.org/abstract.cfm?URI=oe-21-16-19047. 40

[35] E. A. Dyson F. and D. C. Ix. a determination of the deflection of light by the sun's gravitational field, from observations made at the total eclipse of may 29, 1919. *Philosophical Transactions of the Royal Society of London A: Mathematical, Physical and Engineering Sciences*, 220(571-581):291–333, 1920. ISSN 0264-3952. doi: 10.1098/rsta.1920.0009. URL http://rsta.royalsocietypublishing.org/content/220/571-581/291. 1

[36] A. Einstein. Die grundlage der allgemeinen relativitätstheorie. *Annalen der Physik*, 354(7):769–822, 1905. doi: 10.1002/andp.19163540702. URL https://onlinelibrary.wiley.com/doi/abs/10.1002/andp.19163540702. 1

[37] A. Einstein. Investigations on the theory of the brownian movement. *Ann. der Physik*, 1905. URL http://www.physik.fu-berlin.de/~{}kleinert/files/eins_brownian.pdf. 34

[38] A. Einstein. Zur Elektrodynamik bewegter Körper. (German) [On the electrodynamics of moving bodies]. *Annalen der Physik*, 322(10):891–921, 1905. doi: http://dx.doi.org/10.1002/andp.19053221004. 1

[39] R. W. et al. Ligo document m890001-v3, 1989. URL https://dcc.ligo.org/LIGO-M890001/public. 3, 6

[40] M. Evans, S. Ballmer, M. Fejer, P. Fritschel, G. Harry, and G. Ogin. Thermo-optic noise in coated mirrors for high-precision optical measurements. *Phys. Rev. D*, 78:102003, Nov 2008. doi: 10.1103/PhysRevD.78.102003. URL https://link.aps.org/doi/10.1103/PhysRevD.78.102003. 37

[41] M. Evans, L. Barsotti, P. Kwee, J. Harms, and H. Miao. Realistic filter cavities for advanced gravitational wave detectors. *Phys. Rev. D*, 88:022002, Jul 2013. doi: 10.1103/PhysRevD.88.022002. URL https://link.aps.org/doi/10.1103/PhysRevD.88.022002. 39

[42] L. S. Finn. Binary inspiral, gravitational radiation, and cosmology. *Phys. Rev.*, D53:2878–2894, 1996. doi: 10.1103/PhysRevD.53.2878. 5, 6

[43] L. S. Finn and D. F. Chernoff. Observing binary inspiral in gravitational radiation: One interferometer. *Phys. Rev. D*, 47:2198–2219, Mar 1993. doi: 10.1103/PhysRevD.47.2198. URL https://link.aps.org/doi/10.1103/PhysRevD.47.2198. 7

[44] D. Foreman-Mackey, D. W. Hogg, D. Lang, and J. Goodman. emcee : The mcmc hammer. *Publications of the Astronomical Society of the Pacific*, 125(925):306, 2013. URL http://stacks.iop.org/1538-3873/125/i=925/a=306. 101

[45] P. Fritschel, D. Shoemaker, and R. Weiss. Demonstration of light recycling in a michelson interferometer with fabry–perot cavities. *Appl. Opt.*, 31(10): 1412–1418, Apr 1992. doi: 10.1364/AO.31.001412. URL http://ao.osa.org/abstract.cfm?URI=ao-31-10-1412. 22

[46] P. Fritschel, N. Mavalvala, D. Shoemaker, D. Sigg, M. Zucker, and G. González. Alignment of an interferometric gravitational wave detector. *Appl. Opt.*, 37(28): 6734–6747, Oct 1998. doi: 10.1364/AO.37.006734. URL http://ao.osa.org/abstract.cfm?URI=ao-37-28-6734. 33, 42

[47] P. Fritschel, R. Bork, G. González, N. Mavalvala, D. Ouimette, H. Rong,

D. Sigg, and M. Zucker. Readout and control of a power-recycled interferometric gravitational-wave antenna. *Appl. Opt.*, 40(28):4988–4998, Oct 2001. doi: 10.1364/AO.40.004988. URL http://ao.osa.org/abstract.cfm?URI=ao-40-28-4988. 12, 19

[48] P. Fritschel, R. Bork, G. González, N. Mavalvala, D. Ouimette, H. Rong, D. Sigg, and M. Zucker. Readout and control of a power-recycled interferometric gravitational-wave antenna. *Appl. Opt.*, 40(28):4988–4998, Oct 2001. doi: 10.1364/AO.40.004988. URL http://ao.osa.org/abstract.cfm?URI=ao-40-28-4988. 22

[49] C. C. Gerry and P. Knight. *Introductory quantum optics*. Cambridge University Press, 2005. 29, 30, 63

[50] G. I. González and P. R. Saulson. Brownian motion of a mass suspended by an anelastic wire. *The Journal of the Acoustical Society of America*, 96(1):207–212, 1994. doi: 10.1121/1.410467. URL https://doi.org/10.1121/1.410467. 37

[51] D. J. Griffiths. *Introduction to quantum mechanics*. Pearson Prentice Hall, 2005. 28

[52] G. M. Harry, A. M. Gretarsson, P. R. Saulson, S. E. Kittelberger, S. D. Penn, W. J. Startin, S. Rowan, M. M. Fejer, D. R. M. Crooks, G. Cagnoli, J. Hough, and N. Nakagawa. Thermal noise in interferometric gravitational wave detectors due to dielectric optical coatings. *Classical and Quantum Gravity*, 19(5):897, 2002. URL http://stacks.iop.org/0264-9381/19/i=5/a=305. 37

[53] Y. Hefetz, N. Mavalvala, and D. Sigg. Principles of calculating alignment signals in complex resonant optical interferometers. *J. Opt. Soc. Am. B*, 14(7):1597–1606, Jul 1997. doi: 10.1364/JOSAB.14.001597. URL http://josab.osa.org/abstract.cfm?URI=josab-14-7-1597. 51

[54] P. Hello and J.-Y. Vinet. Analytical models of thermal aberrations in massive mirrors heated by high power laser beams. *Journal de Physique*, 51(12):1267–1282, 1990. doi: 10.1051/jphys:0199000510120126700. 82

[55] S. Hild, H. Grote, J. Degallaix, S. Chelkowski, K. Danzmann, A. Freise, M. Hewitson, J. Hough, H. Lück, M. Prijatelj, K. A. Strain, J. R. Smith, and B. Willke. Dc-readout of a signal-recycled gravitational wave detector. *Classical and Quantum Gravity*, 26(5):055012, 2009. URL http://stacks.iop.org/0264-9381/26/i=5/a=055012. 12

[56] S. A. Hughes and K. S. Thorne. Seismic gravity-gradient noise in interferometric gravitational-wave detectors. *Phys. Rev. D*, 58:122002, Nov 1998. doi: 10.1103/PhysRevD.58.122002. URL https://link.aps.org/doi/10.1103/PhysRevD.58.122002. 37

[57] I. K. and S. D. Frequency response of the aligo interferometer: part1. Technical report, California Institute of Technology, 2015. URL https://dcc.ligo.org/LIGO-T1500325. 26, 112, 122

[58] I. K., S. D., and K. K. Frequency response of the aligo interferometer: part2. Technical report, California Institute of Technology, 2015. URL https://dcc.ligo.org/LIGO-T1500461. 26, 122

[59] I. K., S. D., and K. K. Frequency response of the aligo interferometer: part3. Technical report, California Institute of Technology, 2015. URL https://dcc.ligo.org/LIGO-T1500559. 26, 122

[60] H. J. Kimble, Y. Levin, A. B. Matsko, K. S. Thorne, and S. P. Vyatchanin. Conversion of conventional gravitational-wave interferometers into quantum nondemolition interferometers by modifying their input and/or output optics. *Phys. Rev. D*, 65:022002, Dec 2001. doi: 10.1103/PhysRevD.65.022002. URL https://link.aps.org/doi/10.1103/PhysRevD.65.022002. 28, 38, 39, 40

[61] H. Kogelnik and T. Li. Laser beams and resonators. *Appl. Opt.*, 5(10):1550–1567, Oct 1966. doi: 10.1364/AO.5.001550. URL http://ao.osa.org/abstract.cfm?URI=ao-5-10-1550. 126

[62] R. Lawrence, M. Zucker, P. Fritschel, P. Marfuta, and D. Shoemaker. Adaptive thermal compensation of test masses in advanced ligo. *Classical and Quantum Gravity*, 19(7):1803, 2002. URL http://stacks.iop.org/0264-9381/19/i=7/a=377. 78, 81, 90

[63] O. D. M Rakhmanov, F Bondu and R. L. S. Jr. Characterization of the ligo 4 km fabry–perot cavities via their high-frequency dynamic responses to length and laser frequency variations. *Classical and Quantum Gravity*, Feb 2004. URL http://iopscience.iop.org/article/10.1088/0264-9381/21/5/015/meta. 14

[64] F. Magana-Sandoval. Adaptive mode matching upgrade for advanced ligo, 2019. URL https://dcc.ligo.org/LIGO-P1800143. 68

[65] F. Matichard, B. Lantz, K. Mason, R. Mittleman, B. Abbott, S. Abbott, E. Allwine, S. Barnum, J. Birch, S. Biscans, D. Clark, D. Coyne, D. DeBra, R. DeRosa, S. Foley, P. Fritschel, J. Giaime, C. Gray, G. Grabeel, J. Hanson, M. Hillard, J. Kissel, C. Kucharczyk, A. L. Roux, V. Lhuillier, M. Macinnis, B. O'Reilly, D. Ottaway, H. Paris, M. Puma, H. Radkins, C. Ramet, M. Robinson, L. Ruet, P. Sareen, D. Shoemaker, A. Stein, J. Thomas, M. Vargas, and J. Warner. Advanced ligo two-stage twelve-axis vibration isolation and positioning platform. part 1: Design and production overview. *Precision Engineering*, 40:273 – 286, 2015. ISSN 0141-6359. doi: https://doi.org/10.1016/j.precisioneng.2014.09.010. URL http://www.sciencedirect.com/science/article/pii/S0141635914001561. 33

[66] F. Matichard, B. Lantz, K. Mason, R. Mittleman, B. Abbott, S. Abbott, E. Allwine, S. Barnum, J. Birch, S. Biscans, D. Clark, D. Coyne, D. DeBra, R. DeRosa, S. Foley, P. Fritschel, J. Giaime, C. Gray, G. Grabeel, J. Hanson, M. Hillard, J. Kissel, C. Kucharczyk, A. L. Roux, V. Lhuillier, M. Macinnis, B. O'Reilly, D. Ottaway, H. Paris, M. Puma, H. Radkins, C. Ramet, M. Robinson, L. Ruet, P. Sareen, D. Shoemaker, A. Stein, J. Thomas, M. Vargas, and J. Warner. Advanced ligo two-stage twelve-axis vibration isolation and positioning platform. part 2: Experimental investigation and tests results. *Precision Engineering*, 40: 287 – 297, 2015. ISSN 0141-6359. doi: https://doi.org/10.1016/j.precisioneng.2014.11.010. URL http://www.sciencedirect.com/science/article/pii/S0141635914002098. 33

[67] F. Matichard, B. Lantz, R. Mittleman, K. Mason, J. Kissel, B. Abbott, S. Biscans, J. McIver, R. Abbott, S. Abbott, E. Allwine, S. Barnum, J. Birch,

C. Celerier, D. Clark, D. Coyne, D. DeBra, R. DeRosa, M. Evans, S. Foley, P. Fritschel, J. A. Giaime, C. Gray, G. Grabeel, J. Hanson, C. Hardham, M. Hillard, W. Hua, C. Kucharczyk, M. Landry, A. L. Roux, V. Lhuillier, D. Macleod, M. Macinnis, R. Mitchell, B. O'Reilly, D. Ottaway, H. Paris, A. Pele, M. Puma, H. Radkins, C. Ramet, M. Robinson, L. Ruet, P. Sarin, D. Shoemaker, A. Stein, J. Thomas, M. Vargas, K. Venkateswara, J. Warner, and S. Wen. Seismic isolation of advanced ligo: Review of strategy, instrumentation and performance. *Classical and Quantum Gravity*, 32(18):185003, 2015. URL `http://stacks.iop.org/0264-9381/32/i=18/a=185003`. 33

[68] E. Morrison, B. J. Meers, D. I. Robertson, and H. Ward. Automatic alignment of optical interferometers. *Appl. Opt.*, 33(22):5041–5049, Aug 1994. doi: 10.1364/AO.33.005041. URL `http://ao.osa.org/abstract.cfm?URI=ao-33-22-5041`. 47

[69] G. Mueller, Q. ze Shu, R. Adhikari, D. B. Tanner, D. Reitze, D. Sigg, N. Mavalvala, and J. Camp. Determination and optimization of mode matching into optical cavities by heterodyne detection. *Opt. Lett.*, 25(4):266–268, Feb 2000. doi: 10.1364/OL.25.000266. URL `http://ol.osa.org/abstract.cfm?URI=ol-25-4-266`. 70, 74

[70] E. Oelker, T. Isogai, J. Miller, M. Tse, L. Barsotti, N. Mavalvala, and M. Evans. Audio-band frequency-dependent squeezing for gravitational-wave detectors. *Phys. Rev. Lett.*, 116:041102, Jan 2016. doi: 10.1103/PhysRevLett.116.041102. URL `https://link.aps.org/doi/10.1103/PhysRevLett.116.041102`. 39, 116

[71] U. of Birmingham. *Finesse Manual*, 2014. URL `http://www.gwoptics.org/finesse/`. 25, 58

[72] A. T. O'Neil and J. Courtial. Mode transformations in terms of the constituent hermite–gaussian or laguerre–gaussian modes and the variable-phase mode converter. *Optics Communications*, 181(1):35 – 45, 2000. ISSN 0030-4018. doi: https://doi.org/10.1016/S0030-4018(00)00736-7. URL `http://www.sciencedirect.com/science/article/pii/S0030401800007367`. 47, 73, 74, 75

[73] A. Perreca, J. Lough, D. Kelley, and S. W. Ballmer. Multidimensional optical trapping of a mirror. *Phys. Rev. D*, 89:122002, Jun 2014. doi: 10.1103/PhysRevD.89.122002. URL https://link.aps.org/doi/10.1103/PhysRevD.89.122002. 68

[74] F. A. E. Pirani. Republication of: On the physical significance of the riemann tensor. *General Relativity and Gravitation*, 41(5):1215–1232, May 2009. ISSN 1572-9532. doi: 10.1007/s10714-009-0787-9. URL https://doi.org/10.1007/s10714-009-0787-9. 3

[75] J. Ramette, M. Kasprzack, A. Brooks, C. Blair, H. Wang, and M. Heintze. Analytical model for ring heater thermal compensation in the advanced laser interferometer gravitational-wave observatory. *Appl. Opt.*, 55(10):2619–2625, Apr 2016. doi: 10.1364/AO.55.002619. URL http://ao.osa.org/abstract.cfm?URI=ao-55-10-2619. 97

[76] B. E. A. Saleh and M. C. Teich. *Fundamentals of Photonics*. Wiley-Interscience, 2009. 43, 55, 80

[77] P. Saulson. *Fundamentals of Gravitational Wave Detectors*. World Scientific, 2016. 1, 4, 5, 14, 35, 37

[78] P. R. Saulson. Terrestrial gravitational noise on a gravitational wave antenna. *Phys. Rev. D*, 30:732–736, Aug 1984. doi: 10.1103/PhysRevD.30.732. URL https://link.aps.org/doi/10.1103/PhysRevD.30.732. 37

[79] P. R. Saulson. Thermal noise in mechanical experiments. *Phys. Rev. D*, 42:2437–2445, Oct 1990. doi: 10.1103/PhysRevD.42.2437. URL https://link.aps.org/doi/10.1103/PhysRevD.42.2437. 37

[80] B. Schutz. *A First Course in General Relativity*. Cambridge University Press, 2009. 1, 2

[81] B. F. Schutz. *A first course in general relativity*. Cambridge University Press, 2009. 1

[82] R. Shankar. *Principles of Quantum Mechanics*. Springer Verlag, 2014. 27, 28

[83] J. A. Sidles and D. Sigg. Optical torques in suspended fabry–perot interferometers. *Physics Letters A*, 354(3):167 – 172, 2006. ISSN 0375-9601. doi: https://doi.org/10.1016/j.physleta.2006.01.051. URL http://www.sciencedirect.com/science/article/pii/S0375960106001381. 42

[84] K. Strain, K. Danzmann, J. Mizuno, P. Nelson, A. Rüdiger, R. Schilling, and W. Winkler. Thermal lensing in recycling interferometric gravitational wave detectors. *Physics Letters A*, 194(1):124 – 132, 1994. ISSN 0375-9601. doi: https://doi.org/10.1016/0375-9601(94)00717-4. URL http://www.sciencedirect.com/science/article/pii/0375960194007174. 90

[85] P. Veitch, A. Brooks, W. Kim, C. Blair, H. Cao, G. Grabeel, T. Hardwick, M. Heintze, A. Heponstall, C. Ingram, J. Munch, D. Ottaway, and T. Vo. Hartmann wavefront sensors for advanced ligo. In *Conference on Lasers and Electro-Optics*, page SW3M.5. Optical Society of America, 2018. doi: 10.1364/CLEO_SI.2018.SW3M.5. URL http://www.osapublishing.org/abstract.cfm?URI=CLEO_SI-2018-SW3M.5. 91

[86] R. F. C. Vessot, M. W. Levine, E. M. Mattison, E. L. Blomberg, T. E. Hoffman, G. U. Nystrom, B. F. Farrel, R. Decher, P. B. Eby, C. R. Baugher, J. W. Watts, D. L. Teuber, and F. D. Wills. Test of relativistic gravitation with a space-borne hydrogen maser. *Phys. Rev. Lett.*, 45:2081–2084, Dec 1980. doi: 10.1103/PhysRevLett.45.2081. URL https://link.aps.org/doi/10.1103/PhysRevLett.45.2081. 1

[87] J.-Y. Vinet. On special optical modes and thermal issues in advanced gravitational wave interferometric detectors. *Living Reviews in Relativity*, 12(1):5, Jul 2009. ISSN 1433-8351. doi: 10.12942/lrr-2009-5. URL https://doi.org/10.12942/lrr-2009-5. 82, 87, 105

[88] H. Wang, C. Blair, M. D. Álvarez, A. Brooks, M. F. Kasprzack, J. Ramette, P. M. Meyers, S. Kaufer, B. O'Reilly, C. M. Mow-Lowry, and A. Freise. Thermal modelling of advanced ligo test masses. *Classical and Quantum Gravity*, 34(11):115001, 2017. URL http://stacks.iop.org/0264-9381/34/i=11/a=115001. 97

[89] J. Weber. Evidence for discovery of gravitational radiation. *Phys. Rev. Lett.*, 22: 1320–1324, Jun 1969. doi: 10.1103/PhysRevLett.22.1320. URL `https://link.aps.org/doi/10.1103/PhysRevLett.22.1320`. 3

[90] J. M. Weisberg, J. H. Taylor, and L. A. Fowler. Gravitational waves from an orbiting pulsar. *Scientific American*, 245(4):74–83, 1981. ISSN 00368733, 19467087. URL `http://www.jstor.org/stable/24964580`. 1

[91] W. Winkler, K. Danzmann, A. Rüdiger, and R. Schilling. Heating by optical absorption and the performance of interferometric gravitational-wave detectors. *Phys. Rev. A*, 44:7022–7036, Dec 1991. doi: 10.1103/PhysRevA.44.7022. URL `https://link.aps.org/doi/10.1103/PhysRevA.44.7022`. 78, 90

[92] H. Yu, D. Martynov, S. Vitale, M. Evans, D. Shoemaker, B. Barr, G. Hammond, S. Hild, J. Hough, S. Huttner, S. Rowan, B. Sorazu, L. Carbone, A. Freise, C. Mow-Lowry, K. L. Dooley, P. Fulda, H. Grote, and D. Sigg. Prospects for detecting gravitational waves at 5 hz with ground-based detectors. *Phys. Rev. Lett.*, 120:141102, Apr 2018. doi: 10.1103/PhysRevLett.120.141102. URL `https://link.aps.org/doi/10.1103/PhysRevLett.120.141102`. 33

Curriculum Vitae

Title of Dissertation

Adaptive Mode Matching in Advanced LIGO and Beyond

Full Name

Thomas V. Vo

Place and Date of Birth

Seattle, WA July 26, 1988

Colleges and Universities,	Years attended and degrees
University of Washington	2006–2010, B.S.
Syracuse University	2014–2019, M.S.,Ph.D.

Patents

2018 Mode Converter and Quadrant Photodiode for Sensing Optical Cavity Mode Mismatch

Major Department

Physics

Publications

- A. F. Brooks, B. Abbott, M. A. Arain, G. Ciani, A. Cole, G. Grabeel, E. Gustafson, C. Guido, M. Heintze, A. Heptonstall, M. Jacobson, W. Kim, E. King, A. Lynch, S. O'Connor, D. Ottaway, K. Mailand, G. Mueller, J. Munch, V. Sannibale, Z. Shao, M. Smith, P. Veitch, T. Vo, C. Vorvick, and P. Willems. Overview of advanced ligo adaptive optics. Appl. Opt., 55(29):82568265, Oct 2016. doi: 10.1364/AO.55.008256

- P. Veitch, A. Brooks, W. Kim, C. Blair, H. Cao, G. Grabeel, T. Hardwick, M. Heintze, A. Heponstall, C. Ingram, J. Munch, D. Ottaway, and T. Vo. Hartmann wavefront sensors for advanced ligo. In Conference on Lasers and Electro-Optics, page SW3M.5. Optical Society of America, 2018. doi: 10.1364/CLEO SI.2018.SW3M.5.

- Fabian Magana-Sandoval, Thomas Vo, y Daniel Vander-Hyde, J. R. Sanders, and Stefan W. Ballmer Sensing Optical Cavity Mismatch with a Mode-Converter and Quadrant Photodiode (in progress)

Awards and Fellowships

2017-2019 LIGO Hanford Fellow

Major Department

Physics